QUANTITATIVE MICROWAVE IMAGING FOR BREAST CANCER DETECTION

ADVANCES IN REAL-TIME QUANTITATIVE NEAR-FIELD MICROWAVE IMAGING FOR BREAST CANCER DETECTION

BY

DANIEL TAJIK, B.Eng., M.A.Sc.

A THESIS
SUBMITTED TO THE DEPARTMENT OF ELECTRICAL & COMPUTER ENGINEERING
AND THE SCHOOL OF GRADUATE STUDIES
OF MCMASTER UNIVERSITY
IN PARTIAL FULFILMENT OF THE REQUIREMENTS
FOR THE DEGREE OF
DOCTOR OF PHILOSOPHY

Doctor of Philosophy (2022)
(Electrical & Computer Engineering)

McMaster University
Hamilton, Ontario, Canada

TITLE:	Advances in Real-time Quantitative Near-field Microwave Imaging for Breast Cancer Detection
AUTHOR:	Daniel Tajik B.Eng, M.A.Sc. McMaster University, Hamilton, Canada
SUPERVISORS:	Dr. Natalia K. Nikolova Ph.D (University of Electro-Communications) P. Eng. (Ontario) Dr. John W. Bandler D. Sc. (Eng.) (University of London) P. Eng. (Ontario)
NUMBER OF PAGES:	xxii, 183

To my parents and sisters

ABSTRACT

Microwave imaging finds numerous applications involving optically obscured targets. One particular area is breast cancer detection, since microwave technology promises fast low-cost image reconstruction without the use of harmful radiation typical of X-ray mammography. However, the success of microwave imaging is hindered by a critical issue, the complex nature of near-field electromagnetic scattering in tissue. To overcome this, specialized image reconstruction algorithms alongside sensitive measurement hardware are required. In this work, real-time near-field microwave imaging algorithms known as quantitative microwave holography and scattered power mapping are explored. They are experimentally demonstrated to identify potential tumor regions in tissue phantoms. Alongside this development, quality control techniques for evaluating microwave hardware are also described. Two new methods for improving the image reconstruction quality are also presented. First, a novel technique, which combines two commonly used mathematical approximations of scattering (the Born and Rytov approximations), is demonstrated yielding improved image reconstructions due to the complimentary nature of the approximations. Second, a range migration algorithm is introduced which enables near-field refocusing of a point-spread function (PSF), which is critical for algorithms that rely on measured PSFs to perform image reconstruction.

ACKNOWLEDGEMENTS

First, I must begin by thanking my supervisor, Natalia K. Nikolova. She is an incredible professor and I have learned an enormous amount over the course of the last seven years as part of her team. She spent countless hours with me in exploring and deriving new concepts, implementing and testing our ideas, and perfecting numerous manuscripts. Without her, I doubt I would have published as much as I have, and I hope that I can become an engineer and researcher that she is proud of. I must also express gratitude to my co-supervisor John W. Bandler. Over the course of my PhD work, we have collaborated much on the development of 3MT, both at McMaster and abroad, and his lessons on communications skills have impacted me greatly. Thanks to him I will be comfortable communicating both at technical and nontechnical levels for the rest of my life. I also learned to appreciate explorations outside of engineering, which can be beneficial to both the mind and the soul. I must thank my supervisory committee members, Michael D. Noseworthy and James P. Reilly. Both are exemplary professors, and they inspire me with their passion for research and teaching. Their support throughout my PhD studies helped drive my success and I appreciate all their contributions to my research.

To my colleagues I also express my sincerest gratitude. Chaarl Bard, Eric Eveleigh, Farzad Foroutan, Romina Kazemivala, and Yang Meng played a large role in the success of my degree, and their support both past and present means everything to me. Also, thank you to Denys Shumakov, Aaron Pitcher, Jimmy Nguyen, and Mihail Georgiev, without whom I would have been very lonely at the Phoenix. You were always there to help me get up after my failures, and celebrate my successes, and I will never forget that.

I would also like to thank everyone who I had the opportunity to work with on the NEUDOSE satellite project. The support of Andrei R. Hanu, Soo Hyun Byun, Eric Johnston, Devan Wagner, and countless other members of the team has led us close to achieving the seemingly impossible; communicating with a small box 1000 kilometers away on only a shoestring budget (fingers crossed)!

To my former colleagues at Apple, Carlo Di Nallo, Aaron Cooper, Amin Tayebi, Ana Papio Toda, Ali Kiaee, and Eric Barkhouse, I thank you for the time you gave to me to help me improve as an engineer. My experience in California was an exciting whirlwind, and I appreciate you all providing me with unending support. I will never forget my time there, and hope that our paths can cross again in the future.

Thank you to my girlfriend Kristina Klobucar, who has somehow put up with me for 7 years now, with the last two being trapped together in a small 500 square foot apartment thanks to COVID-19. Without her support, this PhD would have been impossible, but her kindness, love, and inspiration have helped me push through the most challenging parts. She is an inspiration herself, and will be completing her PhD degree this year as well, so I look forward to us both being able to relax on a nice beach somewhere once we finally receive our pretty pieces of paper.

I must thank my friends: Derek Klatt, who has always been by my side no matter the struggles I faced; Jeremy Dilks, whom I've been friends with since the age of 5 and has always supported me; Apoorv Vaidya, with whom I still argue politics and discuss finances even after living thousands of kilometers apart for years; Michael Behr and Jake Maclennan, who have somehow dealt with my antics for years, and are always available to provide an opportunity to relax; and to the countless others who have stood beside me and made my life meaningful and truly happy.

Last, but certainly not least, to my parents Inge and Farhad Tajik, my sisters Amanda and Tania, and all my relatives in Canada, Denmark, and Iran, I thank you for your endless patience and unconditional love. There is no doubt in my mind I would not have completed this thesis without you standing behind me. Thank you!

NOTATION AND ABBREVIATIONS

2D	Two Dimensional
3D	Three Dimensional
BA	Born's Approximation
BI-RADS	Breast Imaging Reporting and Data System
CNR	Contrast to Noise Ratio
CO	Calibration Object
CT	Computed Tomography
DFT	Discrete Fourier Transform
EFIE	Electric Field Integral Equation
EM	Electromagnetic
FFT	Fast Fourier Transform
FT	Fourier Transform
Im	Imaginary
MRI	Magnetic Resonance Imaging
OUT	Object Under Test
PBJ	Peanut Butter and Jam
PET	Positron Emission Tomography
PSF	Point Spread Function
QC	Quality Control
QMH	Quantitative Microwave Holography

RA	Rytov's Approximation
Re	Real
RO	Reference Object
ROI	Region of Interest
Rx	Receiving
SAR	Specific Absorption Rate **OR**
	Synthetic Aperture Radar
SNR	Signal to Noise Ratio
SP	Scattering Probe
SPA	Stationary Phase Approximation
SPM	Scattered Power Mapping
TEM	Transverse Electromagnetic
Tx	Transmitting
VNA	Vector Network Analyzer

CONTENTS

LIST OF FIGURES

CHAPTER 1

INTRODUCTION

1.1 History of Medical Microwave Imaging

The first explorations of microwave imaging date back to the late 1960s [1–3]. The utilization of microwave radiation for imaging was an exciting prospect, as microwave radiation can detect optically obscured targets. With a wavelength ranging from 0.1 mm to 10 cm and corresponding image resolution, embedded targets of interest could be investigated without destructive evaluation of the encapsulating material. Indeed, the scientific community immediately began to explore applications that could benefit from this feature, and developments in ground penetrating radar, remote sensing, and biomedical imaging began in earnest [4–11]. Many methods utilized the work of Dennis Gabor's holographic principle derived several decades previously [12]. The concept of holography, utilizing the magnitude and phase information of a field captured on a 2-dimensional (2D) plane to reconstruct 3-dimensional (3D) images, is very straightforward to apply in microwave measurements due to the signal acquisition process. By measuring scattering parameters (S-parameters) using a vector network analyzer (VNA), one acquires a complex signal from which 3D images can be reconstructed. Microwave imaging has since seen widespread use, and is heavily relied upon in airports for concealed weapon detection, satellite weather monitoring, and ground penetrating radar [13–18].

However, microwave imaging for medical diagnostics purposes continues to see only limited clinical use [19–24]. The challenge lies in the extremely complex nature of electromagnetic scattering in human tissue. It is primarily due to diverse tissue heterogeneity, with vastly varying permittivities distributed in widely varying sizes and depths. This is true for the majority of organs in the body, as they are typically comprised of several different tissue types with varying fat and water content. Though dielectric permittivity correlates directly with tissue types (e.g. epidermis, fibroglandular, grey matter, etc.) [25, 26], large ex vivo measurement studies have had their accuracy questioned due to varying experimental procedures such as varying measurement probe penetration depth [27]. On top of this, specific tissue targets for microwave imaging, such as cancerous tissue, have shown permittivity values that can range within the permittivity of healthy tissue, further challenging the accuracy of microwave imaging as a diagnostic tool [28, 29].

Still, promising research is being performed across the globe, and prototypes and clinical trials are underway, with primary focus on the applications of breast cancer screening [30–33]. While breast cancer mortality rates have been steadily declining since 1988, breast cancer remains the second highest cause of cancer-related deaths in women in Canada in 2021 [34]. It is also one of the most prevalent cancers in the 30 to 49 year age group, contributing to 23% of all cancer cases in Canada from 2013-2017. Yet even considering these statistics, healthcare professionals are hesitant to use X-ray mammography for these age groups, citing insignificant decreases in the mortality rate while creating undo-stress in a significant proportion of the screened group due to false-positives [35]. New technology must look to resolve these issues with mammography in order to see wide acceptance and improve mortality rates of breast cancer.

Microwave-based breast cancer screening has multiple benefits over the conventional X-ray mammography systems in that it can avoid painful breast compression, utilizes nonionizing radiation (and thus avoid carcinogenic effects), and can be operated without the use of a trained radiologist due to its detection/quantitative capabilities. One recently developed technology known as the Wavelia currently undergoing clinical trials [36–38]. It has been demonstrated supporting the diagnosis of breast tumors by independent radiologists, and in certain cases has provided improved estimates of tumor size relative to those provided by ultrasound and mammography. In one of the clinical trials, the device successfully identified 12 out of 13 lesions, and was recommended by 92% of the participants in place of more painful X-ray mammography.

Another recent technology undergoing clinical trials is the portable breast-scanning system developed by Kikkawa *et al.* [33]. This system utilizes a hand-held microwave imaging device that has been demonstrated successfully detecting breast cancer tumors of significant size (4-10 cm). However, both mentioned systems still have difficulty in accurately detecting breast cancer tumors in dense breast tissue, and further exploration into algorithmic improvements to the image reconstruction is warranted.

1.2 Models of Electromagnetic Scattering

Key to successful microwave imaging is the underlying forward model of scattering, which enables imaging algorithms to reconstruct the reflective properties of the target based on assumed signal path through the target. Image reconstruction inverts a forward model[1] that maps the microwave data to the dielectric properties of the object under test (OUT). This electromagnetic (EM) scattering model is inherently nonlinear. Nonlinear reconstruction methods aim at inverting the model without the use of linearizing approximations, which demands a solution not only for the dielectric profile of the OUT but also for the field inside it. This necessitates the use of EM simulations, leading to significant computational time. The advantage is that the images are quantitative, i.e., the real and imaginary parts of the object's permittivity can be recovered, subject to the fidelity of the simulations. Examples of such methods include the Born iterative and distorted Born iterative methods [39,40] and the model-based optimization methods [24, 41], which are utilized heavily in biomedical microwave imaging.

In contrast, the linear (or direct) methods employ linearizing approximations of the forward model to dramatically accelerate the reconstruction. However, the validity of these approximations is limited to weak scattering. If the object violates these limits, its image may contain significant artifacts. In the past, linear methods have been able to produce only qualitative images (e.g. normalized reflectivity). Fortunately, recent developments have shown that these methods are in fact capable of generating quantitative (e.g. permittivity and conductivity) images. There are two critical developments that enable this capability. First, quantitatively accurate data equations have become available [42,43]. These map the measured S-parameters (or, alternatively, the port voltages and currents) to the dielectric properties of the OUT.

---

[1] A forward model is mathematical function which computes an output parameter given prescribed inputs. In this thesis, the input values relate to the permittivity of the object and the fields within it, with the output relating to the measured responses external to the object. Inverting a forward model means that the outputs are known and used to identify a particular input parameter, such as the permittivity of an object.

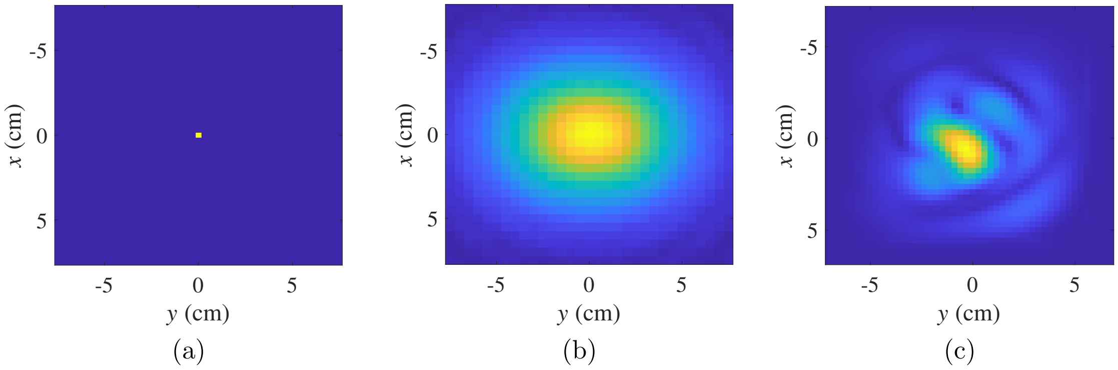

Figure 1.1: Images of (a) an impulse function, (b) a PSF (magnitude) generated using an EM simulation of an electrically small scattering object, and (c) a PSF (magnitude) generated through a measurement of an electrically small scattering object. Note that the measured response differs dramatically, caused by a lower signal-to-noise ratio, measurement tolerances, and other contributing factors.

Second, a calibration method has been developed [44–46], which enables the extraction of the resolvent kernel (i.e., the transfer function of the linearized scattering model) from the measured system point spread function (PSF).

1.2.1 Point Spread Functions

A point spread function is the response of a system to an impulse function. A visual example of a PSF is shown in Fig. 1.1, and demonstrates the difference between a simulated PSF in a noise-free environment, and a measured PSF. This measured PSF is a critical component of quantitative linear inversion algorithms, as it more accurately models a measurement setup than conventional resolvent kernels which rely on idealized analytical approximations and electric field values.

To better understand this, consider the electric field integral equation (EFIE), which is widely known and used as the fundamental equation for electromagnetic scattering of a contrast source [42, 47]:

$$\mathbf{E}(\mathbf{r}) - \mathbf{E}^{\text{inc}}(\mathbf{r}) = \mathbf{E}^{\text{sc}} = \omega^2 \iiint_V \bar{\mathbf{G}}_b(\mathbf{r}, \mathbf{r}') \cdot [\mu_0 \Delta\epsilon(\mathbf{r}')\mathbf{E}(\mathbf{r}')] \, d\mathbf{r}' \tag{1.1}$$

where $\mathbf{E}(\mathbf{r})$ is the total electric field measured at location $\mathbf{r} = (x, y, z)$, $\mathbf{E}^{\text{inc}}(\mathbf{r})$ is the incident electric field, $\mathbf{E}^{\text{sc}}(\mathbf{r})$ is the scattered electric field, ω is the angular frequency, $\bar{\mathbf{G}}_b(\mathbf{r}, \mathbf{r}')$ is Green's dyadic function of the background medium[2], $\mathbf{r}' = (x', y', z')$ is the location internal to the imaged volume V, μ_0 is the permeability of free space, and $\Delta\epsilon = \epsilon_{\text{sc}} - \epsilon_b$ is the relative permittivity contrast between the scattering target and the background. The integral portion of (1.1) is referred to as the scattered field due to an induced source of scattering (e.g. an object embedded within an imaged volume). This equation is nonlinear, as the solution requires a total internal electric field $\mathbf{E}(\mathbf{r}')$ that itself can be described with (1.1). To simplify this model, a common approach known as the Born's approximation can be applied (discussed further in Chapter 2 and Chapter 4) [39, 40, 42]:

$$\mathbf{E}^{\text{sc}}(\mathbf{r}) \approx \omega^2 \iiint_V \bar{\mathbf{G}}_b(\mathbf{r}, \mathbf{r}') \cdot \left[\mu_0 \Delta\epsilon(\mathbf{r}')\mathbf{E}^{\text{inc}}(\mathbf{r}')\right] d\mathbf{r}'. \tag{1.2}$$

Note that the total internal field $\mathbf{E}(\mathbf{r}')$ has now been replaced by the internal incident field $\mathbf{E}^{\text{inc}}(\mathbf{r}')$, which linearizes the forward model, but is only valid in the case where weak scattering effects are present. With an estimate for the Green's function, and measurements of the total and incident electric fields, one can invert this model to

---

[2] The Green's function of a system captures the system's response to an impulse function, e.g. an excitation at a single point. For example, the Green's function of a guitar string would describe the string's vibration as a result of a single quick pluck of the string. It is a very powerful tool in solving linear partial differential equations, and was developed in the 1830s by English mathematician George Green [42, 48].

extract the desired permittivity of the objects under test.

While solving (1.2) is achievable in scenarios relying on full-wave electromagnetic simulation, real-world measurements do not have the luxury of (3D) vectorial electric field extraction, or in the case of near-field imaging, well-known Green's functions. Instead, measurements are performed using scalar quantities and rely heavily on approximations that can introduce modelling errors, which can be as detrimental to the image reconstruction as measurement uncertainty [42, 49].

It is critical that the model correlates as closely as possible to the experimental setup. This can be achieved by either designing the experimental setup to match the model, or by updating the model to match a practical imaging setup. One example of experimental design driven by the forward model is the Dartmouth College monopole antenna system, benefiting from the accurate modelling of each antenna as a line source, and using water as a lossy embedding medium to suppress undesirable characteristics of the antennas (e.g. narrow bandwidth, generation of surface waves) [30, 50]. Model improvement driven by experimental hardware has also been explored in the manipulation of the conventional forward model of (1.2) to incorporate S-parameters widely used in microwave technology [43, 51]:

$$S_{ik}^{\text{sc}}(\mathbf{r}) \approx \frac{j\omega}{2\alpha_i\alpha_k} \iiint_V \Delta\epsilon(\mathbf{r}')\mathbf{E}_i^{\text{inc}}(\mathbf{r}',\mathbf{r}) \cdot \mathbf{E}_k^{\text{inc}}(\mathbf{r}',\mathbf{r}) d\mathbf{r}' \tag{1.3}$$

where S_{ik}^{sc} is the measured S-parameter of the scattered response given a receiving antenna i and a transmitting antenna k, $j = \sqrt{-1}$, $a_{i,k}$ is the outgoing root power wave of the respective antenna, and $\mathbf{E}_i^{\text{inc}}$ is the incident field that would be generated by the receiving antenna if it were operating in a transmitting mode. While this scalar forward model does not account for the true behaviour of complex electromagnetic scattering in heterogeneous structures, it more closely aligns with VNA measurements and avoids discrepancies between the measured data and the underlying algorithmic model. The use of this S-parameter formulation and its implementation has been published in previous work [43, 46, 52] to reasonable success. However, work still remains to improve these underlying forward models, and the experiments that they pair with, in order to enable commercially viable microwave imaging technology for biomedical applications.

1.3 Research Objective

The objective of this research is to further enhance microwave imaging algorithms to enable fast high-fidelity reconstructions to support the need for breast cancer screening technology. To perform these enhancements, two specific imaging algorithms are evaluated, namely quantitative microwave holography (QMH) and scattered power mapping (SPM) [46, 52]. These imaging methods utilize linear approximations of scattering, enabling real-time image reconstruction, while also having the ability to estimate the quantitative permittivity of the target being imaged. In doing so, they present a promising algorithmic methodology for planar imaging technologies. To enhance these techniques, they have been applied to both simulated and experimental setups, and from those have led to several improvements which have been published and comprise the body of this thesis.

1.4 Contributions

The author has contributed to the development of microwave imaging in the following ways:

1. Performed an experimental validation of QMH via a custom-designed breast phantom [53]. Important to the image quality of the reconstruction are real-domain and Fourier-domain filtering techniques which suppress image artifacts. A focusing filter is also applied to demonstrate the ability to evaluate narrow regions of interest (ROI) and reduce image clutter.

2. Developed quality control techniques for evaluating a microwave imaging setup to guarantee sufficient signal quality [54]. These techniques are applied to the planar scanning acquisition setup used in all experiments throughout this thesis, and are incredibly important as they provide a means to ensure sufficient signal quality during measurement.

3. Implemented a novel combined Born/Rytov reconstruction technique that utilizes both linear approximations in tandem to enhance image quality [55, 56]. Both of these approximations have unique limitations, and when used together can dampen approximation-specific artifacts. This work avoids the challenge of Rytov phase unwrapping by excluding the OUT phase information when performing reconstructions, a necessary requirement when performing breast imaging. It also demonstrates the Marks' approach in QMH, which is a modified Born/Rytov method that relies on an ad hoc scaling factor to select an "in-between" approximation for the external field [57].

4. Created a novel technique for reducing the number of PSF measurements required in QMH and SPM via a range migration approach. This technique is derived from the stationary phase approximation [58], and improves on previous implementations by including a magnitude scaling factor in the Fourier-domain migration.

1.5 Outline of the Thesis

This thesis presents the above advances with particular focus on their implementation in QMH, though they are generally applicable to Fourier-domain microwave imaging algorithms. Chapter 2 begins with an evaluation of a custom breast phantom containing a cancerous tissue simulants, and applies the QMH and scattered-power mapping (SPM) algorithms to perform the reconstruction [52, 53]. In this chapter, QMH and SPM are derived, and the construction of the compressed breast phantom is documented. This chapter is duplicated directly from [53] with formatting modifications to improve legibility.

Chapter 3 explores a quality control technique which enables the quality evaluation a microwave imaging system. By studying the contrast-to-noise ratio of a measured PSF, a quality metric can be evaluated and used to improve the acquisition setup. This method is used in all experimental evaluations following this contribution [56, 59, 60]. This chapter is also duplicated directly from a first-authored manuscript [54].

Chapter 4 derives the combined Born/Rytov implementation of QMH, highlighting the benefits of using both approximations in tandem. It presents both simulated and experimental results which demonstrate its ability. This chapter is duplicated from a paper [56], which itself is based on a conference paper [55].

Chapter 5 demonstrates a novel range migration technique that reduces the number of PSF measurements required for both QMH and SPM. It also improves on the conventional angular spectrum representation approach for PSF translation, especially in circumstances where the PSF is located at a range distance proportional to the desired shift along range. This chapter is a manuscript in preparation to be submitted.

Chapter 6 concludes the discussion on improvements to microwave imaging, and provides further developments necessary for QMH and SPM to become practical algorithms for use in biomedical imaging for breast cancer detection.

REFERENCES

[1] R. A. Litten, "An experimental microwave imaging system using preformed beams," Ph.D. dissertation, Sep. 1967. [Online]. Available: http://hdl.handle.net/10945/12175

[2] S. Kazel, "High-sensitivity real-time microwave holography and imaging," *Proc. IEEE*, vol. 57, no. 6, pp. 1222–1222, Jun. 1969.

[3] B. Feingold and B. Levin, "Millimeter wave imaging," in *G-MTT 1970 Intern. Microw. Sym.*, 1970, pp. 126–130.

[4] O.-C. Yue, E. Rope, and G. Tricoles, "Two reconstruction methods for microwave imaging of buried dielectric anomalies," *IEEE Trans. Comput.*, vol. 100, no. 4, pp. 381–390, Apr. 1975.

[5] A. Anderson and P. Richards, "Microwave imaging of subsurface cylindrical scatters from crosspolar backscatter," *Electron. Lett.*, vol. 13, no. 20, pp. 617–619, Sep. 1977.

[6] R. Larson, R. Rawson, D. Ausherman, L. Bryan, and L. Porcello, "Multispectral microwave imaging radar for remote sensing applications," in *Specialist Meeting on Microwave Scattering and Emission from the Earth*, Jan. 1974, pp. 305–315.

[7] N. Farhat, "High resolution microwave holography and the imaging of remote moving objects," *Opt. Eng.*, vol. 14, no. 5, pp. 499–505, Oct. 1975.

[8] J. H. Jacobi and L. E. Larsen, “Microwave interrogation of dielectric targets. part II: By microwave time delay spectroscopy,” *Med. Phys.*, vol. 5, no. 6, pp. 509–513, Nov. 1978.

[9] A. Bahr, “Microwave techniques for NDE of ceramics,” in *SRI Intern.*, 1978.

[10] O. Yue, G. Tricoles, and E. Rope, “Monostatic microwave imaging of buried objects. volume I.” General Dynamics Corp, San Diego, CA. Electronics Division, Tech. Rep., Oct. 1974.

[11] M. Adams and A. Anderson, “Three-dimensional image-construction technique and its application to coherent microwave diagnostics,” in *IEEE Proc. H-Microw. Opt. Antenna*, vol. 127, no. 3. IET, Jun. 1980, pp. 138–142.

[12] D. Gabor, “A new microscopic principle,” *Nature*, no. 666, pp. 777–778, May 1948.

[13] D. M. Sheen, D. L. McMakin, and T. E. Hall, “Three-dimensional millimeter-wave imaging for concealed weapon detection,” *IEEE Trans. Microw. Theory Techn.*, vol. 49, no. 9, pp. 1581–1592, Sep. 2001.

[14] D. Sheen, D. McMakin, and T. Hall, “Near-field three-dimensional radar imaging techniques and applications,” *Appl. Opt.*, vol. 49, no. 19, pp. E83–E93, Jun. 2010.

[15] S. S. Ahmed, “Microwave imaging in security—Two decades of innovation,” *IEEE J. Microw.*, vol. 1, no. 1, pp. 191–201, Jan. 2021.

[16] C. Özdemir, Şevket Demirci, E. Yiğit, and B. Yilmaz1, “A review on migration methods in B-scan ground penetrating radar imaging,” *Math. Probl. Eng.*, vol. 2014, pp. 772–788, Jun. 2014.

[17] I. Catapano, G. Gennarelli, G. Ludeno, and F. Soldovieri, "Applying ground-penetrating radar and microwave tomography data processing in cultural heritage: State of the art and future trends," *IEEE Signal Process. Mag.*, vol. 36, no. 4, pp. 53–61, Jun. 2019.

[18] C. Gilmore, I. Jeffrey, and J. LoVetri, "Derivation and comparison of SAR and frequency-wavenumber migration within a common inverse scalar wave problem formulation," *IEEE Trans. Geosci. Remote Sens.*, vol. 44, no. 6, pp. 1454–1461, Jun. 2006.

[19] M. A. Aldhaeebi, K. Alzoubi, T. S. Almoneef, S. M. Bamatraf, H. Attia, and O. M. Ramahi, "Review of microwaves techniques for breast cancer detection," *Sensors*, vol. 20, no. 8, Apr. 2020. [Online]. Available: https://www.mdpi.com/1424-8220/20/8/2390

[20] S. Semenov, "Microwave tomography: review of the progress towards clinical applications," *Philos. Trans. Royal Soc. A*, vol. 367, no. 1900, pp. 3021–3042, Aug. 2009.

[21] R. C. Conceição, J. J. Mohr, M. O'Halloran *et al.*, *An Introduction to Microwave Imaging for Breast Cancer Detection.* Springer, 2016.

[22] S. Kwon and S. Lee, "Recent advances in microwave imaging for breast cancer detection," *Int. J. Biomed.*, vol. 2016, Dec. 2016.

[23] D. O'Loughlin, M. O'Halloran, B. M. Moloney, M. Glavin, E. Jones, and M. A. Elahi, "Microwave breast imaging: Clinical advances and remaining challenges," *IEEE Trans. Biomed. Eng.*, vol. 65, no. 11, pp. 2580–2590, Nov. 2018.

[24] M. Pastorino, *Microwave Imaging.* John Wiley & Sons, Ltd, 2010.

[25] S. Gabriel, R. Lau, and C. Gabriel, "The dielectric properties of biological tissues: II. measurements in the frequency range 10 Hz to 20 GHz," *Phys. Med. Biol.*, vol. 41, no. 11, p. 2251, Apr. 1996.

[26] M. Lazebnik, M. C. Converse, J. H. Booske, and S. C. Hagness, "Ultrawideband temperature-dependent dielectric properties of animal liver tissue in the microwave frequency range," *Phys. Med. Biol.*, vol. 51, no. 7, p. 1941, Mar. 2006.

[27] E. Porter and M. O'Halloran, "Investigation of histology region in dielectric measurements of heterogeneous tissues," *IEEE Trans. Antennas Propag.*, vol. 65, no. 10, pp. 5541–5552, Aug. 2017.

[28] M. Lazebnik, L. McCartney, D. Popovic, C. B. Watkins, M. J. Lindstrom, J. Harter, S. Sewall, A. Magliocco, J. H. Booske, M. Okoniewski, and S. C. Hagness, "A large-scale study of the ultrawideband microwave dielectric properties of normal breast tissue obtained from reduction surgeries," *Phys. Med. Biol.*, vol. 52, no. 10, p. 2637, Apr. 2007. [Online]. Available: http://stacks.iop.org/0031-9155/52/i=10/a=001

[29] M. Lazebnik, D. Popovic, L. McCartney, C. B. Watkins, M. J. Lindstrom, J. Harter, S. Sewall, T. Ogilvie, A. Magliocco, T. M. Breslin, W. Temple, D. Mew, J. H. Booske, M. Okoniewski, and S. C. Hagness, "A large-scale study of the ultrawideband microwave dielectric properties of normal, benign and malignant breast tissues obtained from cancer surgeries," *Phys.*

Med. Biol., vol. 52, no. 20, p. 6093, Oct 2007. [Online]. Available: http://stacks.iop.org/0031-9155/52/i=20/a=002

[30] P. M. Meaney, M. W. Fanning, T. Raynolds, C. J. Fox, Q. Fang, C. A. Kogel, S. P. Poplack, and K. D. Paulsen, “Initial clinical experience with microwave breast imaging in women with normal mammography,” *Acad. Radiol.*, vol. 14, no. 2, pp. 207–218, Feb. 2007.

[31] J. Garrett and E. Fear, “Stable and flexible materials to mimic the dielectric properties of human soft tissues,” *IEEE Antennas Wireless Propag. Let.*, vol. 13, pp. 599–602, Mar. 2014.

[32] J. A. Tobon Vasquez, R. Scapaticci, G. Turvani, G. Bellizzi, D. O. Rodriguez-Duarte, N. Joachimowicz, B. Duchêne, E. Tedeschi, M. R. Casu, L. Crocco *et al.*, “A prototype microwave system for 3D brain stroke imaging,” *Sensors*, vol. 20, no. 9, p. 2607, May 2020.

[33] M. Adachi, T. Nakagawa, T. Fujioka, M. Mori, K. Kubota, G. Oda, and T. Kikkawa, “Feasibility of portable microwave imaging device for breast cancer detection,” *Diagnostics*, vol. 12, no. 1, Dec. 2022. [Online]. Available: https://www.mdpi.com/2075-4418/12/1/27

[34] Canadian Cancer Society’s Advisory Committee on Cancer Statistics, “Canadian cancer statistics,” 2021. [Online]. Available: https://cancer.ca/en/research/cancer-statistics/canadian-cancer-statistics

[35] S. Klarenbach, N. Sims-Jones, G. Lewin, H. Singh, G. Thériault, M. Tonelli, M. Doull, S. Courage, A. J. Garcia, and B. D. Thombs, “Recommendations on

screening for breast cancer in women aged 40–74 years who are not at increased risk for breast cancer," *CMAJ*, vol. 190, no. 49, pp. E1441–E1451, Dec. 2018. [Online]. Available: https://www.cmaj.ca/content/190/49/E1441

[36] "Wavelia: Microwave breast imaging scanner," accessed on 2022-02-23. [Online]. Available: https://www.wavelia.com/

[37] B. M. Moloney, P. F. McAnena, S. M. Abd Elwahab, A. Fasoula, L. Duchesne, J. D. Gil Cano, C. Glynn, A. O'Connell, R. Ennis, A. J. Lowery, and M. J. Kerin, "Microwave imaging in breast cancer – results from the first-in-human clinical investigation of the Wavelia system," *Acad. Radiol.*, vol. 29, pp. S211–S222, Jan. 2022, Special Issue: Breast Imaging. [Online]. Available: https://www.sciencedirect.com/science/article/pii/S1076633221002993

[38] B. M. Moloney, P. F. McAnena, S. M. Elwahab, A. Fasoula, L. Duchesne, J. D. Gil Cano, C. Glynn, A. O'Connell, R. Ennis, A. J. Lowery *et al.*, "The Wavelia microwave breast imaging system–tumour discriminating features and their clinical usefulness," *Br. J. Radiol.*, vol. 94, no. 1128, p. 20210907, Oct. 2021.

[39] Y. M. Wang and W. C. Chew, "An iterative solution of the two-dimensional electromagnetic inverse scattering problem," *Int. J. Imag. Sys. Tech.*, vol. 1, no. 1, pp. 100–108, 1989.

[40] W. C. Chew and Y. M. Wang, "Reconstruction of two-dimensional permittivity distribution using the distorted Born iterative method," *IEEE Trans. Med. Imag.*, vol. 9, no. 2, pp. 218–225, Jun. 1990.

[41] K. D. Paulsen, P. M. Meaney, L. C. Gilman, and eds., *Alternative Breast Imaging: Four Model-based Approaches.* Boston, MA: Cambridge University Press, 2017.

[42] N. K. Nikolova, *Introduction to Microwave Imaging.* Cambridge, United Kingdom: Springer Science & Business Media, 2017.

[43] A. S. Beaverstone, D. S. Shumakov, and N. K. Nikolova, "Integral equations of scattering for scalar frequency-domain responses," *IEEE Trans. Microw. Theory Techn.*, vol. 64, no. 4, pp. 1120–1132, Apr. 2015.

[44] S. Tu, J. J. McCombe, D. S. Shumakov, and N. K. Nikolova, "Fast quantitative microwave imaging with resolvent kernel extracted from measurements," *Inverse Probl.*, vol. 31, no. 4, p. 045007, Apr. 2015.

[45] R. K. Amineh, J. J. McCombe, A. Khalatpour, and N. K. Nikolova, "Microwave holography using measured point-spread functions," *IEEE Trans. Instrum. Meas.*, vol. 64, no. 2, pp. 403–417, Feb. 2015.

[46] D. Tajik, A. D. Pitcher, and N. K. Nikolova, "Comparative study of the Rytov and Born approximations in quantitative microwave holography," *Prog. Electromagn. Res. B*, vol. 79, pp. 1–19, Jan. 2017.

[47] W. C. Chew, *Waves and Fields in Inhomogeneous Media.* IEEE Press, 1990.

[48] *Green's Functions (Intuitive Ideas).* John Wiley & Sons, Ltd, 2011, ch. 1, pp. 51–90. [Online]. Available: https://onlinelibrary.wiley.com/doi/abs/10.1002/9780470906538.ch1

[49] M. Ostadrahimi, P. Mojabi, C. Gilmore, A. Zakaria, S. Noghanian, S. Pistorius, and J. LoVetri, "Analysis of incident field modeling and incident/scattered

field calibration techniques in microwave tomography," *IEEE Antennas Wireless Propag. Lett.*, vol. 10, pp. 900–903, Sep. 2011.

[50] P. Meaney, M. Fanning, D. Li, S. Poplack, and K. Paulsen, "A clinical prototype for active microwave imaging of the breast," *IEEE Trans. Microw. Theory Techn.*, vol. 48, no. 11, pp. 1841–1853, Nov. 2000.

[51] D. Tajik, D. S. Shumakov, A. S. Beaverstone, and N. K. Nikolova, "Quasi-real time reconstruction of the complex permittivity of tissue through microwave holography," *11th Eur. Conf. Antennas Propag. EuCAP*, pp. 3485–3488, Mar. 2017.

[52] D. S. Shumakov and N. K. Nikolova, "Fast quantitative microwave imaging with scattered-power maps," *IEEE Trans. Microw. Theo. Techn.*, vol. 66, no. 1, pp. 439–449, Jan. 2018.

[53] D. Tajik, F. Foroutan, D. S. Shumakov, A. D. Pitcher, and N. K. Nikolova, "Real-time microwave imaging of a compressed breast phantom with planar scanning," *IEEE J. Electrom. RF Microw. Med. Bio.*, vol. 2, no. 3, pp. 154–162, Sep. 2018.

[54] D. Tajik, J. Trac, and N. K. Nikolova, "Quality control of microwave equipment for tissue imaging," *IEEE J. Electromagn., RF, Microw. Med. Biol.*, vol. 4, no. 1, pp. 52–60, Mar. 2019.

[55] D. Tajik, N. K. Nikolova, and M. D. Noseworthy, "Improving quantitative microwave holography through simultaneous use of the Born and Rytov approximations," in *16th Euro. Radar Conf. EuRAD*, Nov. 2019.

[56] D. Tajik, R. Kazemivala, and N. K. Nikolova, “Real-time imaging with simultaneous use of Born and Rytov approximations in quantitative microwave holography,” *IEEE Trans. Microw. Theory Techn.*, pp. 1–14, Dec. 2021.

[57] D. L. Marks, “A family of approximations spanning the Born and Rytov scattering series,” *Opt. Express*, vol. 14, no. 19, pp. 8837–8848, Sep. 2006. [Online]. Available: http://www.opticsexpress.org/abstract.cfm?URI=oe-14-19-8837

[58] S. J. Orfanidis, *Electromagnetic Waves and Antennas.* Rutgers University, 2015, vol. 1.

[59] D. Tajik, J. Trac, and N. K. Nikolova, “Spatial resolution evaluation of a microwave system for breast cancer screening,” in *13th Euro. Conf. Antennas Propag. EuCAP.* IEEE, Jun. 2019, pp. 1–5.

[60] D. Tajik, R. Kazemivala, and N. K. Nikolova, “Point-spread functions in inverse scattering and image reconstruction with microwaves and millimeter waves,” in *Electromagnetic Waves and Antennas for Biomedical Applications*, L. Wang, Ed. London, England: Institute of Engineering and Technology, 2022, ch. 1, pp. 1 – 46.

CHAPTER 2

REAL-TIME MICROWAVE IMAGING OF A COMPRESSED BREAST PHANTOM WITH PLANAR SCANNING

Preface

This chapter is a reproduction of the following published article:

D. Tajik, F. Foroutan, D. S. Shumakov, A. D. Pitcher, and N. K. Nikolova, "Real-time microwave imaging of a compressed breast phantom with planar scanning," in *IEEE J. Electromagn. RF Microw. Med. Bio.*, vol. 2, no. 3, pp. 154–162, Sep. 2018, doi: 10.1109/JERM.2018.2841380.

I designed the phantom, implemented the quantitative microwave holography (QMH) algorithm in code, designed the experiment, performed the image reconstructions with QMH, and wrote/edited the manuscript. Farzad Foroutan assisted in the experimental setup and measurement acquisition. Denys Shumakov provided the scattered power mapping (SPM) results and assisted in writing the theoretical SPM section. Aaron Pitcher assisted in the experimental setup and measurement acquisition. Natalia K. Nikolova developed the experimental concept and edited the manuscript.

2.1 Introduction

Microwave imaging has been successful in a variety of applications dealing with optically obscured targets such as concealed-weapon detection, through-the-wall imaging, nondestructive testing, meteorology, and ground-penetrating radar [1–7], where numerous commercial systems are in use. It also shows potential in medical diagnostics due to the nonionizing radiation, the relatively low cost and the compact light-weight electronics [8–10]. Despite its advantages, microwave systems have not yet become clinical imaging tools. There are a few challenges [11] that need to be overcome to make the technology competitive with the existing imaging modalities. In the case of breast-cancer screening, the common modality is mammography. While the above advantages hold in comparison with mammography, microwave technology is yet to demonstrate comparable or better sensitivity and specificity.

The main challenge stems from the complexities of the microwave scattering in tissue, which involves high attenuation, multiple reflections as well as diffraction and refraction within a heterogeneous medium that contains both electrically large and small anatomical details along with widely varying permittivity and conductivity values; see, e.g., [12]. As a result, microwave propagation in tissue is complicated and it is intrinsically nonlinear with respect to the permittivity of the object under test (OUT). The microwave-imaging community has developed various reconstruction algorithms to handle these complexities [8–11, 13, 14].

Here, we focus on two recently proposed direct-inversion methods, quantitative microwave holography (QMH) [15] and scattered-power mapping (SPM) [16]. They have been shown to reconstruct the complex permittivity of tissue objects of relatively small thickness (1 to 2 cm). As other direct-inversion methods, both QMH and SPM rely on a linearizing approximation in the forward model of scattering using either Born's approximation (BA) or Rytov's approximation (RA) [5,13,17–20]. The advantage of the direct-inversion methods is that they enable real-time imaging.

Until recently, it was believed that direct inversion can produce only qualitative images [6]. However, the work in [15, 16] along with earlier work reported in [21–24] demonstrates that quantitative permittivity estimates of tissue objects can be obtained with methods such as QMH and SPM.

The key to quantitative reconstruction with direct-inversion methods is a calibration measurement of the system point-spread function (PSF) [5]. The measured PSF brings two important advantages. Firstly, it provides a properly scaled forward model, which enables the quantitative reconstruction. Also, this forward model is inherently system-specific thus obviating the need to approximate Green's function and the incident field with analytical or simulated field distributions. Such approximations are inadequate in the near-field measurements of tissue and they lead to model inaccuracy and image artifacts. Secondly, the measured PSF allows for inversion through deconvolution, which is numerically fast.

The disadvantage of direct-inversion methods, QMH and SPM included, stems from the linearization of the forward model. This leads to an inability to account for the mutual influence of closely spaced scatterers, which are common in tissue. Multiple scattering is also ignored; however, it is less significant due to the high attenuation. Thus, direct-inversion methods may produce lower-resolution images than nonlinear iterative methods such as microwave tomography [25], which do not employ linearizing approximations.

Still, the quantitative direct-inversion methods can provide a much better starting point for the nonlinear reconstruction than the commonly employed assumption of a uniform medium. Moreover, they can serve as linear-inversion modules in nonlinear reconstructions based on the Born iterative and distorted Born iterative methods [17, 26]. Therefore, quantitative direct inversion in tissue imaging is worthy of investigation in both scenarios: as stand-alone reconstruction algorithms and as linear modules within iterative reconstruction.

The aim of this work is to study the performance of QMH and SPM as stand-alone algorithms in experiments with a compressed breast-tissue phantom of realistic thickness. Compression in breast imaging reduces the signal loss through the tissue and thus improves the signal-to-noise ratio (SNR). Beside the ionizing radiation, one of the drawbacks of X-ray mammography is the level of compression which may cause pain. The mean thickness in routine mammography in a craniocaudal view is about 4.4 cm; see, for example [27]. The respective mean thickness in the mediolateral oblique view is about 4.8 cm [27]. Compression levels aiming at smaller than the above mean thicknesses are often required, leading to significant patient discomfort. It is expected that microwave-based mammography would not require uncomfortable compression since thicknesses equal to or exceeding the mean thicknesses used in X-ray mammography allow for good signal quality [11]. Here, we demonstrate imaging of breast phantoms of thickness 4.8 cm.

There is another reason that makes the investigation of the microwave imaging of the compressed breast worthwhile. It is well known that compression can exploit the significant difference in stiffness among glandular, fatty and cancerous tissues [28, 29].

Multiple measurements of the same tissue object at different compression levels displace healthy tissue more significantly than tumorous tissue. In view of the non-ionizing nature of the microwave radiation, multiple measurements within a single examination session are indeed admissible, enabling better identification of cancerous regions. Before these studies can occur, QMH and SPM must be demonstrated functioning in a typical mammography breast compression scenario.

The purpose of this work is to evaluate both QMH and SPM at compression thicknesses comparable to the mean thicknesses in routine X-ray mammography. These reconstruction methods have been previously shown [15, 16] to be successful in imaging tissue phantoms, the thickness of which is about 1 cm. However, at thicknesses of approximately 5 cm, the signal-to-noise ratio (SNR) is significantly reduced due to the substantial attenuation in breast tissue. Thus, validation at mean mammography compression is required along with strategies to deal with low data SNR.

To this end, comparisons between the Rytov and Born approximations with QMH and SPM at these thicknesses have not been done. As shown in previous work, the two approximations provide images, which may differ substantially depending on the heterogeneity of the sample and the data SNR [15]. One critical difference is that BA is sensitive to the size of high-contrast scattering objects whereas RA is not. On the other hand, the RA-based reconstruction exhibits sensitivity to sharp discontinuities in the spatial dependence of the phase of the data across the acquisition plane. Since the volume has been increased five-fold from previous tissue experiments, re-evaluation of the two approximations is necessary. To verify the approximations, a simplistic compressed-breast tissue phantom is constructed. Finally, since both QMH and SPM can execute within seconds, filtering strategies can be easily implemented and explored. In particular, here we show that focusing filters can improve the diagnostic quality of the final images.

2.2 Forward Model of Scattering

Both QMH and SPM operate on frequency-domain responses such as S-parameters. Wide-bandwidth frequency sweeps are used as they improve the spatial resolution [5]. The forward model of scattering in terms of S-parameter data is given by [5, 30]:

$$S_{ik}^{\mathrm{sc,OUT}}(\mathbf{r}; f) = \frac{\mathrm{i}\omega\epsilon_0}{2a_i a_k} \cdot \iiint_V \Delta\epsilon_{\mathrm{r}}(\mathbf{r}')\mathbf{E}_i^{\mathrm{inc}}(\mathbf{r}', \mathbf{r}; f) \cdot \mathbf{E}_k^{\mathrm{tot}}(\mathbf{r}', \mathbf{r}_{\mathrm{Tx}}; f)dv', \tag{2.1}$$

where $S_{ik}^{\mathrm{sc,OUT}}$ is the scattering portion of the S-parameter measured with the OUT, i.e., the portion due to the presence of the OUT in the background (or host) medium. Note that the S-parameters are not zero in the absence of an OUT because reflection and transmission still occur at the terminals of the transmitting (Tx) and receiving (Rx) antennas. The S-parameter is acquired at the location $\mathbf{r}$ and at frequency f. The position inside the imaged volume V is denoted by $\mathbf{r}' = (x', y', z')$. In the case of planar scans, $\mathbf{r} \equiv (x, y, \bar{z})$, where the acquisition plane is fixed at $\bar{z}$ and the Rx antenna scans laterally along x and y. Also, $\mathrm{i} = \sqrt{-1}$ and a_ζ ($\zeta = i, k$) is the incoming root-power wave at the ζ antenna, when it operates in a Tx mode. Assuming all quantities are root-mean-square (RMS) phasors, a_ζ is the square root of the incoming power at the ζ-th port. Further, ϵ_0 is the permittivity of free space and

$$\Delta\epsilon_{\mathrm{r}}(\mathbf{r}') = \epsilon_{\mathrm{r,OUT}}(\mathbf{r}') - \epsilon_{\mathrm{r,b}}(\mathbf{r}') \tag{2.2}$$

is the permittivity contrast in the volume of interest V. Here, $\epsilon_{\mathrm{r,OUT}}$ and $\epsilon_{\mathrm{r,b}}$ are the complex relative permittivities of the OUT and the background, respectively. Note that the latter is known at least approximately. $\mathbf{E}_i^{\mathrm{inc}}(\mathbf{r}', \mathbf{r}; f)$ is the incident-field distribution as a function of $\mathbf{r}' \in V$ produced by the Rx (i-th) antenna if it were to operate in a Tx mode at the location $\mathbf{r}$. $\mathbf{E}_k^{\mathrm{tot}}(\mathbf{r}', \mathbf{r}_{\mathrm{Tx}}; f)$ is the total-field distribution as a function of $\mathbf{r}'$ due the Tx (k-th) antenna k at $\mathbf{r}_{\mathrm{Tx}}$.

In our setup, the Rx and Tx antennas are aligned along each other's boresight and move together along x and y on two parallel planes on both sides of the OUT, i.e., $\mathbf{r}_{\mathrm{Tx}} = (x, y, \bar{z} + D)$, where D is the distance between the two planes. Thus, $\mathbf{r}$ defines uniquely the position of both the Rx and the Tx antennas and the explicit use of $\mathbf{r}_{\mathrm{Tx}}$ is unnecessary.

Applying Born's approximation [17] to the total internal field,

$$\mathbf{E}_k^{\mathrm{tot}}(\mathbf{r}', \mathbf{r}; f) \approx \mathbf{E}_k^{\mathrm{inc}}(\mathbf{r}', \mathbf{r}; f), \tag{2.3}$$

and substituting (2.3) into (2.1) leads to the linearized forward model of scattering:

$$S_{ik}^{\mathrm{sc,OUT}}(\mathbf{r}; f) \approx \frac{\mathrm{i}\omega\epsilon_0}{2a_i a_k} \iiint_V \Delta\epsilon_{\mathrm{r}}(\mathbf{r}') \left[\mathbf{E}_i^{\mathrm{inc}} \cdot \mathbf{E}_k^{\mathrm{inc}}\right](\mathbf{r}', \mathbf{r}; f) dv' . \tag{2.4}$$

The incident-field dot product $\left[\mathbf{E}_i^{\mathrm{inc}} \cdot \mathbf{E}_k^{\mathrm{inc}}\right](\mathbf{r}', \mathbf{r}; f)$, also referred to as the resolvent kernel [21], can be acquired using the measured point-spread function (PSF). Consider the measurement of an electrically small scattering probe of known size Ω_{sp} and known relative permittivity $\epsilon_{\mathrm{r,sp}}$ embedded in a uniform background medium at position $\mathbf{r}'_{\mathrm{sp}} = (x'_{\mathrm{sp}}, y'_{\mathrm{sp}}, z'_{\mathrm{sp}})$. The contrast function of the scattering probe can be represented as $\Delta\epsilon_{\mathrm{r}}(\mathbf{r}') = \Delta\epsilon_{\mathrm{r,sp}}\delta(\mathbf{r}' - \mathbf{r}'_{\mathrm{sp}})$, where $\delta(\mathbf{r}')$ is the 3D Dirac delta function.

Here, $\Delta\epsilon_{\mathrm{r,sp}} = \epsilon_{\mathrm{r,sp}} - \epsilon_{\mathrm{r,b}}$. Based on (2.4), the response of the scattering probe can now be written as

$$S_{ik}^{\mathrm{sc,PSF}}(\mathbf{r},\mathbf{r}'_{\mathrm{sp}};f) \approx \frac{\mathrm{i}\omega\epsilon_0\Delta\epsilon_{\mathrm{r,sp}}(\mathbf{r}')\Omega_{\mathrm{sp}}}{2a_i a_k}\left[\mathbf{E}_i^{\mathrm{inc}}\cdot\mathbf{E}_k^{\mathrm{inc}}\right](\mathbf{r}'_{\mathrm{sp}},\mathbf{r};f)\,. \tag{2.5}$$

This is the system PSF for a point scatterer at $\mathbf{r}'_{\mathrm{sp}}$. It follows that the respective resolvent kernel is derived from the PSF as

$$\left[\mathbf{E}_i^{\mathrm{inc}}\cdot\mathbf{E}_k^{\mathrm{inc}}\right](\mathbf{r}'_{\mathrm{sp}},\mathbf{r};f) \approx \frac{S_{ik}^{\mathrm{sc,PSF}}(\mathbf{r},\mathbf{r}'_{\mathrm{sp}};f)2a_i a_k}{\mathrm{i}\omega\epsilon_0\Delta\epsilon_{\mathrm{r,sp}}(\mathbf{r}')\Omega_{\mathrm{sp}}}\,. \tag{2.6}$$

Assuming the background is uniform, the PSF is translationally invariant in the lateral directions x and y. In other words, if the PSF is measured with the scattering probe at the center of the plane $z'_{\mathrm{sp}} = const.$, $\mathbf{r}'_0 = (0,0,z'_{\mathrm{sp}})$, then the PSF can be derived for any other scattering-probe position $\mathbf{r}'_{\mathrm{sp}} = (x'_{\mathrm{sp}}, y'_{\mathrm{sp}}, z'_{\mathrm{sp}})$ as

$$S_{ik}^{\mathrm{sc,PSF}}(x,y,\bar{z};x'_{\mathrm{sp}},y'_{\mathrm{sp}},z'_{\mathrm{sp}};f) = S_{ik}^{\mathrm{sc,PSF}}(x-x'_{\mathrm{sp}},y-y'_{\mathrm{sp}},\bar{z};0,0,z'_{\mathrm{sp}};f)\,. \tag{2.7}$$

Note that for each imaged z'-plane, a separate PSF measurement with the scattering probe at $z'_{\mathrm{sp}} = z'$ is required. Analytical approximations of the z dependence of the PSF are also possible [5] but have not been employed here.

Using (2.6) and the PSF in (2.7), the forward model in (2.4) is expressed as

$$S_{ik}^{\mathrm{sc,OUT}}(\mathbf{r}) \approx \iiint_V \rho(\mathbf{r}')S_{ik}^{\mathrm{sc,PSF}}(\mathbf{r}-\mathbf{r}'_{xy},\mathbf{r}'_0)dv,' \tag{2.8}$$

where $\mathbf{r}'_{xy} = (x', y', 0)$ and

$$\rho(\mathbf{r}') = \Delta\epsilon_{\mathrm{r}}(\mathbf{r}') \cdot (\Delta\epsilon_{\mathrm{r,sp}}\Omega_{\mathrm{sp}})^{-1} \tag{2.9}$$

is the reflectivity function to be recovered. The above integral is a 2D convolution (in x, y) of $\rho(\mathbf{r}')$ and the PSF. Thus, both the QMH and the SPM methods essentially perform inversion through 2D deconvolution at each z' plane to obtain the respective slice of the OUT image. The difference between the two methods lies in the way this inversion is done.

2.3 Approximations of the Scattering Data

The scattered responses $S_{ik}^{\mathrm{sc,OBJ}}$ of the imaged objects (OBJ), OBJ denoting either the OUT or the PSF, cannot be measured directly.

They are derived from two measurements. The first is a calibration measurement, which is independent of the OUT. It is carried out in the background without any embedded scatterers and it provides the incident-field portion of the response S_{ik}^{inc}. The measurement with a scattering probe is also part of the system calibration and it provides the total-field PSF $S_{ik}^{\mathrm{tot,PSF}}$. Finally, the measurement of the OUT provides the total-field OUT response $S_{ik}^{\mathrm{tot,OUT}}$.

2.3.1 Born's Approximation

Born's approximation (BA) relies on the assumption that the total-field response is a superposition of the incident and scattered field responses [5, 19]:

$$S_{ik}^{\text{tot,OBJ}}(\mathbf{r}; f) \approx S_{ik}^{\text{inc}}(\mathbf{r}; f) + S_{ik}^{\text{sc,OBJ}}(\mathbf{r}; f), \tag{2.10}$$

where $S_{ik}^{\text{sc,OBJ}}(\mathbf{r})$ is the scattered field response. With this assumption, the scattered portions of the PSF and the OUT responses are derived as

$$S_{ik}^{\text{sc,OBJ}}(\mathbf{r}; f) \approx S_{ik}^{\text{tot,OBJ}}(\mathbf{r}; f) - S_{ik}^{\text{inc}}(\mathbf{r}; f)\,. \tag{2.11}$$

The applicability of BA is constrained by both the size and the contrast of the OUT [5, 17]. Large, high-contrast scatterers may lead to image artifacts and degradation of the quantitative accuracy. This is important bearing in mind the relatively large thickness required to image a realistic breast phantom.

2.3.2 Rytov's Approximation

Rytov's approximation (RA) views the total-field response as a phase correction of the incident field with the complex phase being a scaled version of the scattered-field response [5, 17, 19]:

$$S_{ik}^{\text{tot,OBJ}}(\mathbf{r}; f) \approx S_{ik}^{\text{inc}}(\mathbf{r}; f) \cdot \exp\left(\frac{S_{ik}^{\text{sc,OBJ}}(\mathbf{r}; f)}{S_{ik}^{\text{inc}}(\mathbf{r}; f)}\right). \tag{2.12}$$

To extract the scattered component, (2.12) is rearranged:

$$S_{ik}^{\mathrm{sc,OBJ}}(\mathbf{r};f) \approx S_{ik}^{\mathrm{inc}}(\mathbf{r};f) \cdot \ln\left(\frac{S_{ik}^{\mathrm{tot,OBJ}}(\mathbf{r};f)}{S_{ik}^{\mathrm{inc}}(\mathbf{r};f)}\right). \tag{2.13}$$

Unlike BA, RA is limited only by the permittivity contrast and it is not sensitive to the size of the scattering object [5, 17]. This is an important advantage in breast imaging where the electrical size of the OUT is large but the contrast between malignant and healthy tissue is low.

One should be aware that RA is sensitive to phase wrapping, which is not a factor in BA. Consider (2.13) written in terms of magnitude and phase:

$$S_{ik}^{\mathrm{sc,OBJ}}(\mathbf{r};f) = S_{ik}^{\mathrm{inc}}(\mathbf{r};f) \cdot \\ \left\{ \ln\frac{|S_{ik}^{\mathrm{tot,OBJ}}(\mathbf{r};f)|}{|S_{ik}^{\mathrm{inc}}(\mathbf{r};f)|} + \mathrm{i}\left[\angle S_{ik}^{\mathrm{tot,OBJ}}(\mathbf{r};f) - \angle S_{ik}^{\mathrm{inc}}(\mathbf{r};f)\right]\right\}. \tag{2.14}$$

The imaginary part of (2.14) is different depending on whether the signal is phase wrapped or unwrapped. Thus, in order to generate a valid reconstruction, it is recommended that all responses are phase unwrapped before applying RA.

2.4 Quantitative Microwave Holography

QMH solves (2.8) in the Fourier domain where the 2D convolution is replaced by a multiplication. The integration along z' is replaced by a discrete sum, leading to

$$\widetilde{S}_{ik}^{\mathrm{sc,OUT}}(\boldsymbol{\kappa},\bar{z};f) \approx \sum_{z} \widetilde{\rho}(\boldsymbol{\kappa},z')\widetilde{S}_{ik}^{\mathrm{sc,PSF}}(\boldsymbol{\kappa},z';f)\Omega_v\,. \tag{2.15}$$

Here, $\widetilde{S}_{ik}^{\text{sc,OUT}}$, $\widetilde{\rho}$, and $\widetilde{S}_{ik}^{\text{sc,PSF}}$ are the respective Fourier-transformed quantities in (2.8), $\boldsymbol{\kappa} = (\kappa_x, \kappa_y)$ is the spectral position in the Fourier domain, and Ω_v is the volume of a voxel. It is important to note that the data acquired in tissue imaging must be normalized with respect to the signal strength in order to compensate for its strong frequency dependence, i.e., its decline with increasing frequency. This normalization procedure can be found in [15].

The reflectivity function $\widetilde{\rho}(\boldsymbol{\kappa})$ is found one spectral position $\boldsymbol{\kappa}$ at a time by solving the system of equations:

$$\mathbf{A}(\boldsymbol{\kappa})\widetilde{\boldsymbol{\rho}}(\boldsymbol{\kappa}) = \mathbf{b}(\boldsymbol{\kappa}), \tag{2.16}$$

where

$$\mathbf{A}(\boldsymbol{\kappa}) = \begin{bmatrix} \widetilde{S}_{ik}^{\text{sc,PSF}}(\boldsymbol{\kappa}, z_1, f_1) & \cdots & \widetilde{S}_{ik}^{\text{sc,PSF}}(\boldsymbol{\kappa}, z_{N_z}, f_1) \\ \vdots & \ddots & \vdots \\ \widetilde{S}_{ik}^{\text{sc,PSF}}(\boldsymbol{\kappa}, z_1, f_{N_f}) & \cdots & \widetilde{S}_{ik}^{\text{sc,PSF}}(\boldsymbol{\kappa}, z_{N_z}, f_{N_f}) \end{bmatrix}, \tag{2.17}$$

$$\widetilde{\boldsymbol{\rho}}(\boldsymbol{\kappa}) = \Omega_v \left[\widetilde{\rho}(\boldsymbol{\kappa}, z_1) \cdots \widetilde{\rho}(\boldsymbol{\kappa}, z_{N_z}) \right]^T, \tag{2.18}$$

$$\mathbf{b}(\boldsymbol{\kappa}) = \left[\widetilde{S}_{ik}^{\text{sc,OUT}}(\boldsymbol{\kappa}, f_1) \cdots \widetilde{S}_{ik}^{\text{sc,OUT}}(\boldsymbol{\kappa}, f_{N_f}) \right]^T . \tag{2.19}$$

Here, z'_m, $m = 1, ..., N_z$, is the depth position and f_n, $n = 1, ..., N_f$, is the frequency sample. The system is typically solved using the pseudoinverse function due to the rectangular structure of $\mathbf{A}(\boldsymbol{\kappa})$ [15].

Once the reflectivity function at each depth position z' is found in the 2D Fourier domain, inverse 2D Fourier transform is applied to obtain its distribution in real space as a function of x' and y'. The relative permittivity distribution of the OUT is derived from the reflectivity function as:

$$\epsilon_{\mathrm{r,OUT}}(\mathbf{r}') \approx \Delta\epsilon_{\mathrm{r,sp}}\Omega_{\mathrm{sp}}\Omega_v^{-1} \cdot \rho(\mathbf{r}') + \epsilon_{\mathrm{r,b}}\,. \tag{2.20}$$

As shown in [21], the approximate forward model in (2.4) improves if either of the following requirements are fulfilled:

$$\epsilon_{\mathrm{r,OUT}}(\mathbf{r}') \approx \epsilon_{\mathrm{r,sp}}, \tag{2.21}$$

or,

$$|\epsilon_{\mathrm{r,OUT}}(\mathbf{r}')|, |\epsilon_{\mathrm{r,sp}}| \ll |\epsilon_{\mathrm{r,b}}|. \tag{2.22}$$

In tissue imaging, achieving (2.21) is not feasible since the permittivity in breast tissues can vary widely. However, the background permittivity can be selected to be higher in absolute value than that of both the scattering probe and the inspected tissue object, satisfying (2.22). Increasing $|\epsilon_{\mathrm{r,b}}|$ through increased loss of the background medium is beneficial in reducing reflections from enclosures and other components of the measurement setup. However, compromise must be made between increasing the losses in the background medium and the SNR of the data. Finally, selecting $\epsilon_{\mathrm{r,sp}}$ to be similar to the permittivity of a particular tissue target (e.g. cancer) improves the quantitative result for this target in the image.

2.5 Scattered Power Mapping

The SPM algorithm starts by constructing the scattered-power map of the OUT at each frequency. These are 3D complex-valued maps, which are in essence qualitative images of the OUT complex contrast [5, 16]. They are expressed as

$$M_{ik}^{\mathrm{OUT}}(\mathbf{r}'; f) = \iint\limits_{xy} S_{ik}^{\mathrm{sc,OUT}}(\mathbf{r}; f) \cdot [S_{ik}^{\mathrm{sc,PSF}}(\mathbf{r}; \mathbf{r}'; f)]^* dx dy, \tag{2.23}$$

where the asterisk denotes conjugation, $\mathbf{r} = (x, y, \bar{z})$, and $\mathbf{r}' = (x', y', z')$. Substituting (2.8) into (2.23) and exchanging the order of integration leads to

$$M_{ik}^{\mathrm{OUT}}(\mathbf{r}'; f) \approx \int\limits_{x''}\int\limits_{y''}\int\limits_{z''} \rho(\mathbf{r}'') \cdot M_{ik}^{\mathrm{PSF}}(\mathbf{r}'; \mathbf{r}''; f) dx'' dy'' dz'' \tag{2.24}$$

where $\mathbf{r}'' = (x'', y'', z'')$ and

$$M_{ik}^{\mathrm{PSF}}(\mathbf{r}'; \mathbf{r}''; f) = \iint\limits_{xy} S_{ik}^{\mathrm{sc,PSF}}(\mathbf{r}; \mathbf{r}''; f) \cdot [S_{ik}^{\mathrm{sc,PSF}}(\mathbf{r}; \mathbf{r}'; f)]^* dx dy \tag{2.25}$$

is the 3D scattered-power map as a function of $\mathbf{r}'$ (i.e., the qualitative image) of the scattering probe when it is positioned at $\mathbf{r}''$. In the case of uniform background, the PSF power maps are translationally invariant in x and y, which allows (2.24) to be written in terms of a 2D convolution similarly to (2.8):

$$M_{ik}^{\mathrm{OUT}}(\mathbf{r}'; f) \approx \int\limits_{x''}\int\limits_{y''}\int\limits_{z''} \rho(\mathbf{r}'') \cdot M_{ik}^{\mathrm{PSF}}(\mathbf{r}' - \mathbf{r}''_{xy}; \mathbf{r}''_0; f) dx'' dy'' dz'', \tag{2.26}$$

where $\mathbf{r}''_{xy} = (x'', y'', 0)$ and $\mathbf{r}''_0 = (0, 0, z'')$.

With multi-frequency data, $\mathbf{M}_{ik}^{\mathrm{OUT}}$ and $\mathbf{M}_{ik}^{\mathrm{PSF}}$ are combined into a single map [16, 21]:

$$M^{\mathrm{OBJ}}(\mathbf{r}') = \frac{1}{N_f} \sum_{m=1}^{N_f} \frac{M_{ik}^{\mathrm{OBJ}}(\mathbf{r}', f_m)}{\max\left(|M_{ik}^{\mathrm{PSF}}(\mathbf{r}'; \mathbf{r}''_0; f_m)|\right)}, \tag{2.27}$$

where OBJ≡OUT, PSF. The above linear combination of scattered-power maps can be extended to include the S-parameters for all Rx and Tx antennas, indexed by i and k, respectively. Since the linear combination of (2.27) is applied to both the left side of (2.26) and to its kernel, the forward model of the SPM can be finally stated as:

$$M^{\mathrm{OUT}}(\mathbf{r}') \approx \iiint\limits_{x''\,y''\,z''} \rho(\mathbf{r}'') \cdot M^{\mathrm{PSF}}(\mathbf{r}' - \mathbf{r}''_{xy}; \mathbf{r}''_0) dx'' dy'' dz''. \tag{2.28}$$

Similarly to QMH, we cast (2.28) into 2D Fourier domain as:

$$\widetilde{M}^{\mathrm{OUT}}(\boldsymbol{\kappa}, z') \approx \Omega_v \sum_{z''} \widetilde{\rho}(\boldsymbol{\kappa}, z'') \widetilde{M}^{\mathrm{PSF}}_{\mathbf{r}''_0}(\boldsymbol{\kappa}, z') \tag{2.29}$$

where $\widetilde{M}^{\mathrm{PSF}}_{\mathbf{r}''_0}(\boldsymbol{\kappa}, z')$ is the 2D Fourier transform of $M^{\mathrm{PSF}}(\mathbf{r}'; \mathbf{r}''_0)$ with respect to x' and y'. Thus, the reflectivity $\widetilde{\rho}(\boldsymbol{\kappa}, z'')$ is recovered by solving a linear system of equations at each spectral position $\boldsymbol{\kappa}$, similarly to (2.15). The difference is that here the system matrix is of size $N_z \times N_z$ whereas the QMH system matrix is of size $N_f \times N_z$. In either case, these linear systems of equations are very small and their solution is found practically instantaneously. In our experiments, N_f is typically on the order of 10 to 100, whereas N_z is on the order of 3 to 10.

2.6 Compressed Breast Phantom Experiment

2.6.1 Acquisition Setup

QMH and SPM have been previously used to image thin tissue phantoms approximately 1 cm thick [16, 24, 31]. To ensure these methods are clinically viable, they are

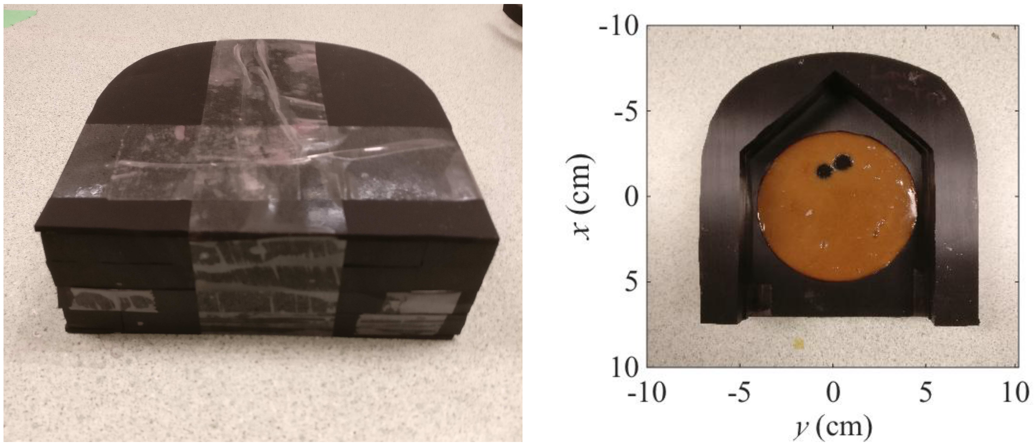

(a) (b)

Figure 2.1: Photos of the compressed breast phantom. a) Fully constructed phantom approximately 4.8 cm thick, and b) partially constructed phantom showing the location of the blueberries, 2 cm above the base of the phantom.

tested here with tissue thickness similar to that in mammography.

We have constructed a 4.8 cm thick modifiable compressed breast phantom; see Fig. 2.1. The permittivities of all phantom components were measured from 3 GHz to 8 GHz using a slim form probe [32]. Their averages are shown in Table 1.

The bulk of the phantom is comprised of four 1.1 cm thick stacked carbon-rubber sheets custom-ordered from Emerson & Cuming Ltd. (now Laird Tech). These sheets are carefully designed to have a permittivity and loss similar to that of averaged scattered fibroglandular (Class-2) breast tissue [33]. They were cut to form the shape of a compressed breast. A house-shaped section from each carbon-rubber sheet is separated to provide flexibility inserting different contrast structures into different layers of the phantom. The second layer from the bottom has a circular section removed and a Petri dish is inserted containing 2 blueberries. Since blueberries have similar permittivity to that of cancerous breast tissue [11,34], they are used to emulate a small cancerous structure within the breast. The blueberries are surrounded with a peanut butter and jam mixture (PBJ) which is designed to have similar permittivity to the carbon-rubber sheets. To construct the PBJ, a 9:1 jam to peanut butter volume ratio was mixed together in a food blender. The ratio of PBJ was determined by mixing different quantities and repeatedly measuring with an Agilent slim form probe [32] until the correct permittivity was acquired. Using PBJ as an embedding medium removes air gaps with high permittivity contrast that could violate the limitations of both BA and RA. High permittivity contrast with air gaps has been shown in previous work to severly hinder the quantitative reconstruction [16, 24]. On both the top and bottom of the phantom, a 2 mm thick carbon-rubber sheet of a higher relative permittivity (JCS-15, Laird Tech) than the thick sheets (see Table 1) was placed to represent skin. Finally, the phantom is wrapped in thin plastic wrap. Overall, this phantom represents a simplified compressed breast and is the first stage towards experimenting with thicker, more complex phantoms.

The OUT is the compressed breast phantom placed in a 30 cm by 30 cm *Plexiglas* tray, and surrounded with a background medium made of PBJ identical to the mixture surrounding the blueberries. An image of the blueberry layer is shown in Fig. 2.1b. The OUT is completed with a *Plexiglas* lid of the same thickness as the base of the tray. The PSF measurement is that of a small dielectric cylinder ($\epsilon_{\mathrm{r}} \approx 50 - 0\mathrm{i}$, radius $= 0.5$ cm, height $= 1.0$ cm) inserted in the PBJ medium at the center of the tray and aligned at the same range location as that of the Petri-dish layer of the phantom. The incident-field measurement is that of the tray containing the PBJ medium.

The acquisition setup comprises two transverse electromagnetic (TEM) horns impedance matched to the carbon-rubber sheets [35]. The horns are aligned along boresight and are positioned approximately 2 mm away from the top and bottom

Table 2.1: Averaged Dielectric Properties of Materials from 3 GHz to 8 GHz

Material (Structure)	ϵ'	ϵ''
Thick Carbon-rubber Sheet (Averaged Breast Tissue)	10.91	2.84
PBJ (Embedding Medium)	10.41	5.07
Thin Carbon-rubber Sheet (Averaged Skin Tissue)	15.69	10.28
Blueberry (Cancerous Tissue)	55.27	16.63
Scattering Probe (PSF)	50.00	0.05

Plexiglas plates, which are 4 mm thick. The overall distance between the apertures of the two antennas is 6 cm. The setup is shown in Fig. 2.2.

A raster scan is performed across a 20 cm by 20 cm acquisition area at 2 mm increments following the guidelines suggested in [15]. Transmission data S_{21} is acquired in a frequency bandwidth from 3 GHz to 8 GHz at 100 MHz intervals, generating over 600,000 individual data points. A 3-W continuous-wave power amplifier [36] is attached to the Tx antenna, and a 35 dB low-noise amplifier [37] is attached at the Rx antenna.

The mechanical scan is slow. In this case, it takes close to 6 hours. It is clear that while the current prototype offers flexibility in optimizing the acquisition setup and the sampling step, it cannot be used in the clinic. An electronically switched system is currently under development [38–40], which is estimated to complete a full scan in about 2 minutes.

2.6.2 Results

The reconstructed images using QMH and SPM are shown in Fig. 2.3 and Fig. 2.4. The computation takes 1.5 seconds using MATLAB on a 2013 Macbook Pro.

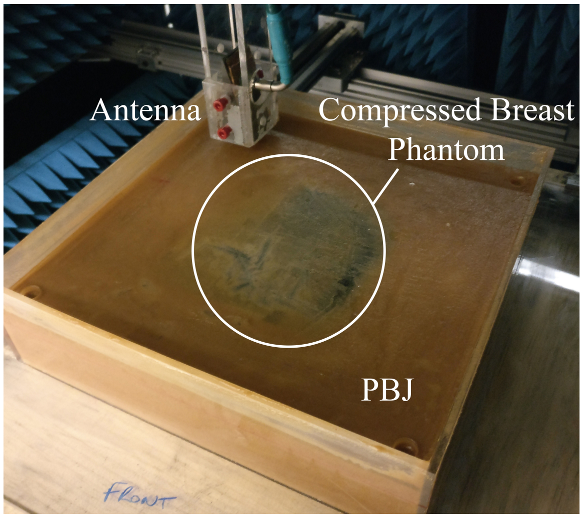

Figure 2.2: Photo of the acquistion setup during the OUT measurement. A lid is placed over the compressed breast phantom which is centered in the PBJ mixture. The antennas are positioned 2 mm above and below the *Plexiglas* plates.

Qualitatively, QMH and SPM produce similar results when using the same scattered-data approximation (BA or RA). In the BA reconstruction, the contours of the breast phantom appear strongly. This is due to air pockets which reside along the edges of the phantom. The air pockets present large high-contrast structures that impact the inversion negatively. This makes the blueberries, located approximately around (0,0), difficult to discern.

On the other hand, QMH and SPM under RA successfully locate the blueberries. This is due to to the insensitivity of RA to the size of the scattering objects. However, RA is unable to accurately depict the shape of the structures.

In quantitative terms, both QMH and SPM struggle with the reconstruction. Nonphysical permittivity values ($\mathrm{Re}\{\epsilon_\mathrm{r}\} < 1$, $\mathrm{Im}\{\epsilon_\mathrm{r}\} > 0$) remain a significant challenge, since they cannot be submitted to an iterative solver. A simple strategy for removing nonphysical values has already been proposed in [41].

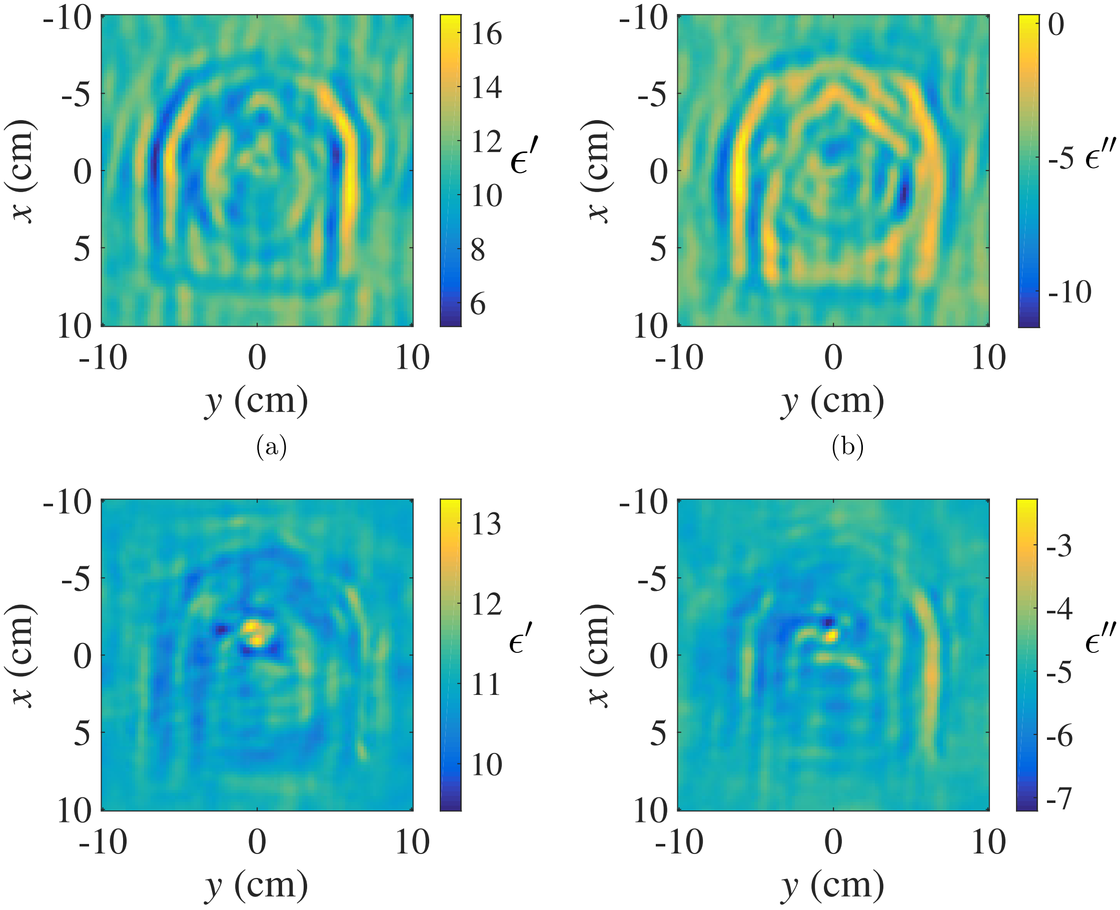

(a) (b)

(c) (d)

Figure 2.3: Reconstructed images of the compressed breast phantom using QMH (permittivity relative to vacuum): a) real permittivity with BA, b) imaginary permittivity with BA, c) real permittivity with RA, d) imaginary permittivity with RA.

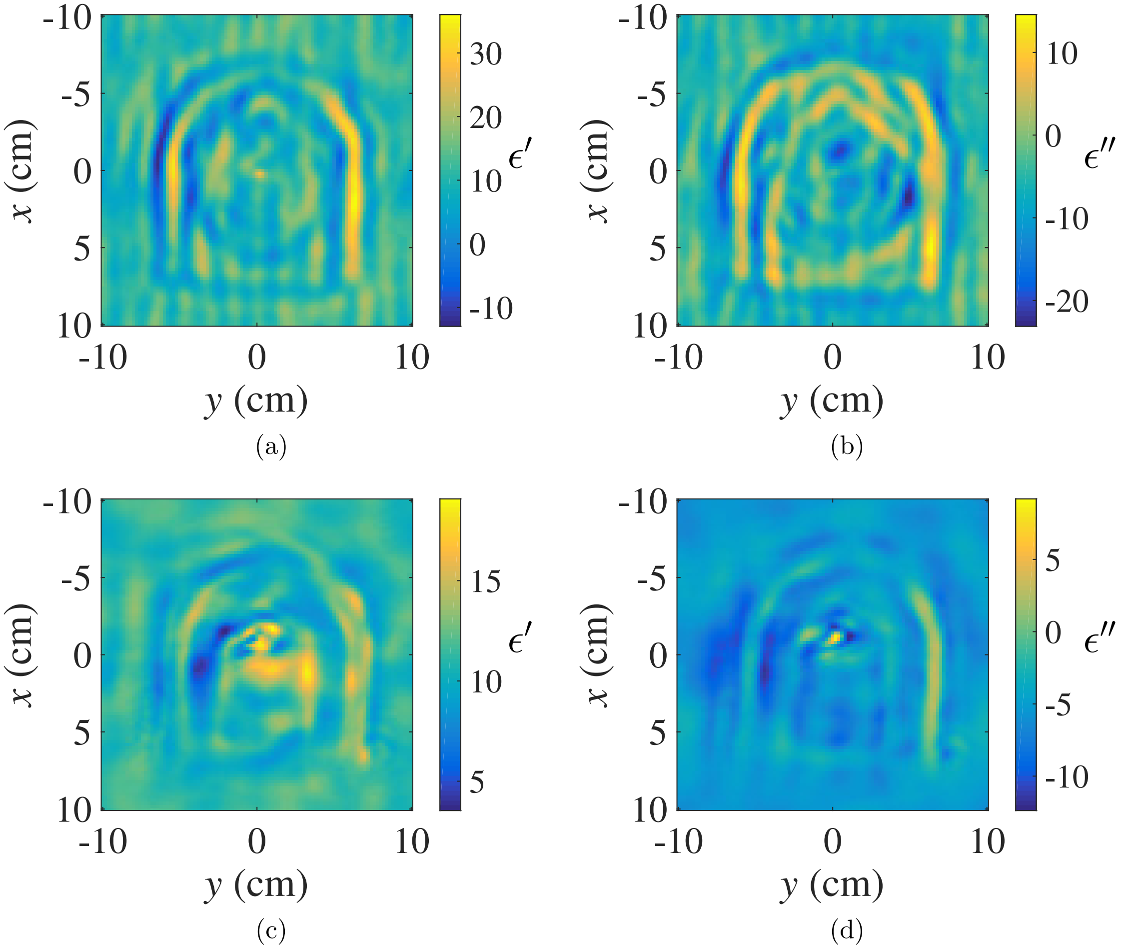

Figure 2.4: Reconstructed images of the compressed breast phantom using SPM (permittivity relative to vacuum): a) real permittivity with BA, b) imaginary permittivity with BA, c) real permittivity with RA, d) imaginary permittivity with RA.

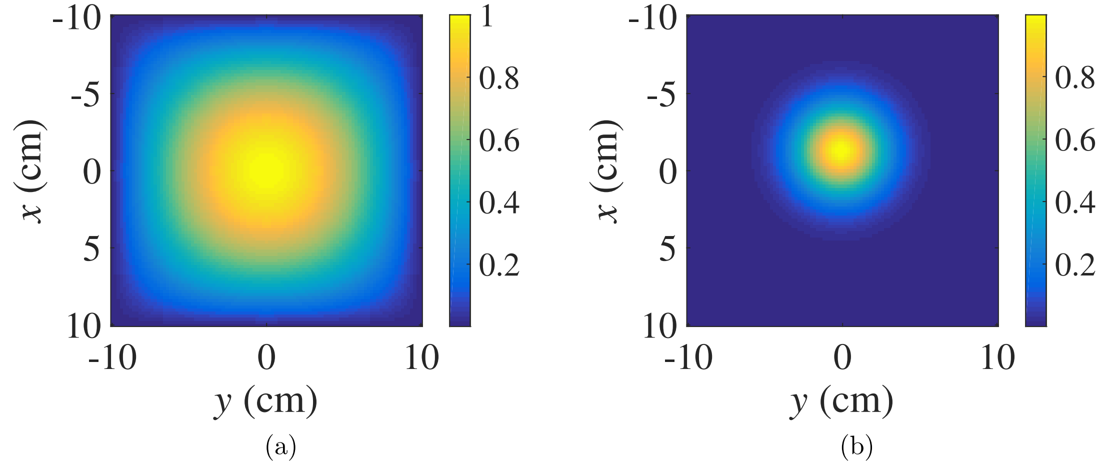

(a) (b)

Figure 2.5: Images of the apodization filters: a) Unfocused apodization filter using a 2D cosine function, b) focused apodization filter using a Gaussian function centered on the blueberry location predicted by the RA reconstruction.

2.7 Discussion

2.7.1 Permittivity of the Background Medium

It was shown in [21] that a background permittivity larger than the OUT permittivity improves the accuracy of the linearized forward model when using a PSF-based kernel. Also, since the PBJ is very lossy, reflections due to the acquisition setup are suppressed. These reflections have been shown to often corrupt the image reconstruction [15]. For clinical studies, a medium which provides a uniform high permittivity background should be used.

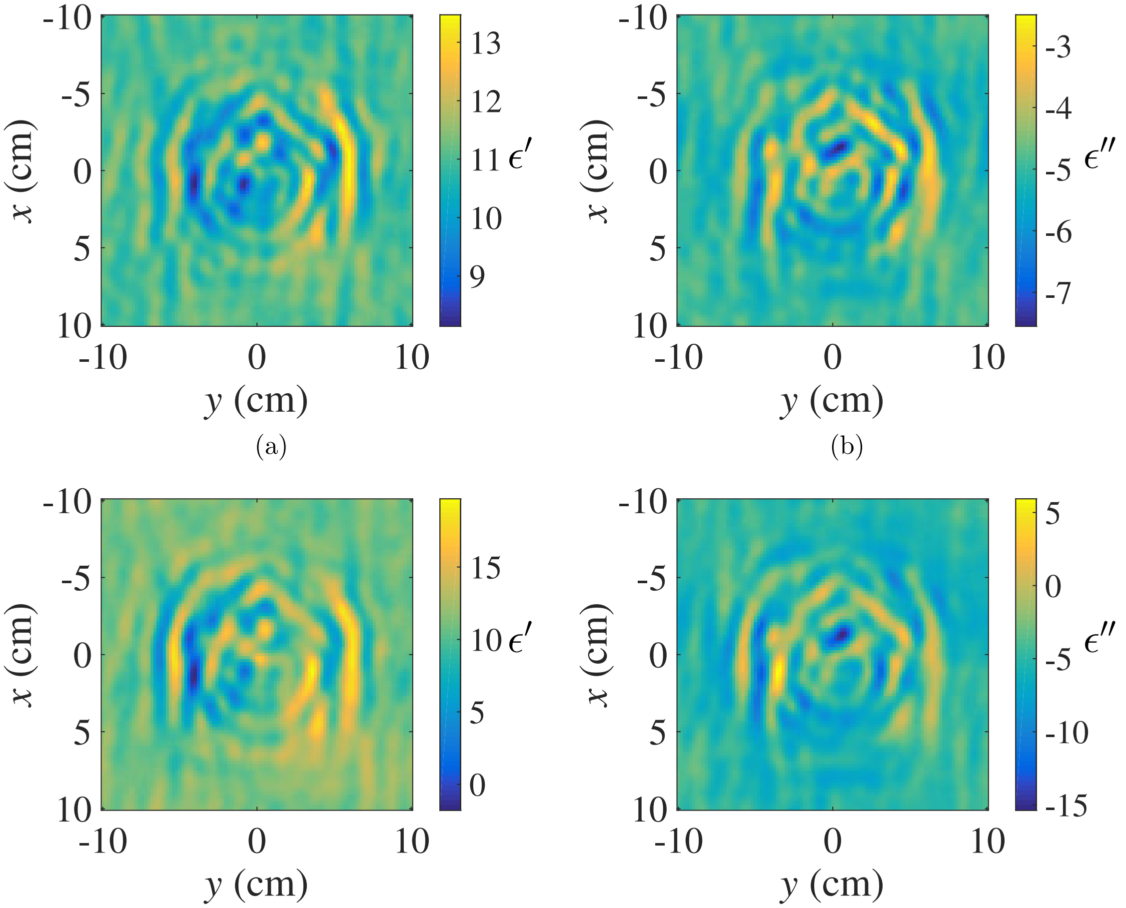

(a) (b)

(c) (d)

Figure 2.6: Reconstructed images of the compressed breast phantom under BA and using a focusing filter (permittivity relative to vacuum): a) real permittivity with QMH, b) imaginary permittivity with QMH, c) real permittivity with SPM, d) imaginary permittivity with SPM.

2.7.2 Apodization and Fourier-domain Filtering

Two filters, the apodization filter and the Fourier-domain low-pass filter, are used to improve the image quality in both QMH and SPM. These filters are necessary due to the methods' susceptibility to mathematical errors stemming from the use of the Fourier and inverse Fourier transform [15]. The apodization filter is a spatial window that is applied to the scattered signals of the PSF and the OUT. This filter tapers the edges of the image to zero, which avoids numerical artifacts due to discontinuous boundaries. A cosine window is selected due to its simple implementation, and is illustrated in Fig. 2.5a.

The post-inversion low-pass filter is used to filter out the high spatial-frequency components of the Fourier transform of the reflectivity function. It is well known that a Fourier domain low-pass filter has tradeoffs between high image resolution and suppression of noise. The method used to determine the filter parameters is shown in [15].

2.7.3 Born's Approximation and Rytov's Approximation

As shown in section 2.6.2, there are trade-offs in using either BA or RA to estimate the scattered data from the total-field and incident-field measurements. BA struggles with large tissue phantoms due to limitations related to size, which is not the case for RA. On the other hand, RA is prone to phase errors and it may fail to correctly identify the shape of the inclusions. There is therefore an advantage to using the RA-based reconstruction to first find regions of interest (ROI). Then, with a focused apodization filter, the BA reconstruction can succesfully reconstruct details within the ROI.

Fig. 2.6 depicts the QMH and SPM reconstruction under BA with the focused Gaussian filter shown in Fig. 2.5b. The blueberries' shape and location are reconstructed in both the real and imaginary part of the permittivity distribution obtained with both QMH and SPM.

Note that there is flexibility in the design of the focusing filter. Since both SPM and QMH execute quickly, tuning of the focusing filter can be accomplished in real time. This is a practical tool to enhance diagnostic quality.

2.8 Conclusion

For the first time, quantitative microwave holography (QMH) and scattered power mapping (SPM) are demonstrated as methods capable of imaging compressed dense breast tissue for cancer detection. They are shown detecting cancerous simulants in an experiment with a phantom of 4.8 cm thickness similar to the mean thickness of compressed breast in routine mammography. Two blueberries 1 cm in diameter are inserted into the breast phantom. They have permittivity similar to that of breast-cancer samples. The phantom is embedded in a high-permittivity/high-loss medium which improves the quality of the reconstruction while also suppressing unwanted reflections generated by the acquisition setup. The results demonstrate that while QMH and SPM reconstruct similar images, their implementation with either Born's approximation (BA) or Rytov's approximation (RA) has an impact on the overall reconstruction. Importantly, the RA-based reconstruction can be used to locate small scattering structures, which can then be resolved better by BA reconstruction that employs a controlled apodization filter. The QMH and SPM algorithms utilizing either BA or RA execute in MATLAB [42] within a couple of seconds on a 2013 Macbook Pro.

One critical concern with microwave imaging technology is its compliance with health and safety regulations. Due to the fact that microwave-imaging technology is still in a pre-clinical stage of development, no specific regulations exist at this time. This is in contrast with magnetic resonance imaging (MRI) technology, for which regulations exist; see, e.g., Health Canada Safety Code 26 [43]. In the meantime, the general regulations pertaining to electromagnetic radiation (typically that of communication devices), such as Health Canada Safety Code 6 [44], can be used as a reference.

Due to the very long exposure time, a mechanical scan using a 3-W transmission would not satisfy the Health Canada Safety Code 6 limitations for the specific absorption rate (SAR); see section 2.1.2 in [44]. As an example, at frequencies up to 6 GHz, the SAR basic restrictions are: 1.6 W/kg (uncontrolled environment) and 8 W/kg (controlled environment) averaged over any 6 minute reference period. [1]

However, an electronically switched acquisition within 2 minutes can easily satisfy the safety regulations for a *controlled environment* with a power-transmission level of 3 W. For a 20 cm by 20 cm acquisition aperture, a two-minute measurement at 3 W input power would generate an averaged incident power density of 25 W/m^2, where the averaging is done over the prescribed period of 6 minutes. It was shown in a microwave breast-imaging SAR study [45] that a power density of 10 W/m^2 produced a peak SAR of 1.7 W/kg in the breast. Since power density and SAR are linearly

---

[1] A controlled environment is the one which: 1) has adequately characterized the RF fields intensities in the area, 2) exposure is incurred by persons who are aware and cognizant of RF exposure and intensity, and 3) exposure is incurred by persons who are aware of risks and can apply mitigation strategies [44].

related, the estimated peak SAR for our system is 4.25 W/kg, which falls well within the safety limits for a controlled environment.

Future work aims towards reconstructing 3D images of tissue in real time. In principle, this requires PSFs for each imaged z-plane, which implies multiple PSF measurements and, therefore, increased system-calibration effort. The development of a range-translation algorithm that can synthetically shift an already measured PSF to other locations along range would eliminate the need for multiple PSF measurements.

Further study on readily available low-cost background mediums (e.g. ultrasound gel) is also necessary. To further validate the methods, more complex phantoms containing larger heterogeneities need to be imaged.

Finally, the two methods must be integrated in an iterative solver, which would improve the resolution and eliminate nonphysical values. This would pave the way towards clinically-viable microwave imaging tools for breast-cancer screening.

REFERENCES

[1] D. M. Sheen, D. L. McMakin, and T. E. Hall, “Three-dimensional millimeter-wave imaging for concealed weapon detection,” *IEEE Trans. Microw. Theory Techn.*, vol. 49, no. 9, pp. 1581–1592, Sep. 2001.

[2] M. G. Amin, *Through-the-wall Radar Imaging*, CRC Press, 2016.

[3] W.F. Hitschfeld, “The invention of radar meteorology,” *Bulletin Amer. Meteorological Soc.* , vol. 67, no. 1, pp. 33–37, Jan. 1986.

[4] D. J. Daniels, *Ground Penetrating Radar*, Wiley, 2005.

[5] N. K. Nikolova, *Introduction to Microwave Imaging*, Cambridge University Press, 2017.

[6] M. Pastorino, *Microwave Imaging*, Wiley, 2010.

[7] S. Kharkovsky and R. Zoughi, “Microwave and millimeter wave nondestructive testing and evaluation – overview and recent advances,” *IEEE Instrum. Meas. Mag.*, vol. 10, no. 2, pp. 26–38, Apr. 2007.

[8] N. K. Nikolova, “Microwave biomedical imaging,” *Wiley Encyclopedia of Electrical and Electronics Engineering*, pp. 1–22, Apr. 2014.

[9] R. C. Conceição, J. J. Mohr, M. O’Halloran (Eds.), *An Introduction to Microwave Imaging for Breast Cancer Detection*, Springer, 2016.

[10] S. Kwon and S. Lee, “Recent advances in microwave imaging for breast cancer detection,” *Int. J. Biomed. Imag.*, vol. 2016, Article ID 5054912, 25 pages, Dec. 2016.

[11] N. K. Nikolova, “Microwave imaging for breast cancer,” *IEEE Microw. Mag.*, vol. 12, no. 2, pp. 78–94, Dec. 2011.

[12] T. Sugitani, S. Kubota, S. Kuroki, K. Sogo, K. Arihiro, M. Okada, T. Kadoya, M. Hide, M. Oda, and T. Kikkawa, “Complex permittivities of breast tumor tissues obtained from cancer surgeries,” *Appl. Phys. Lett.*, vol. 104, Article ID 253702, Jun. 2014.

[13] A. C. Kak and M. Slaney, *Principles of Computerized Tomographic Imaging*, IEEE Press, 1988.

[14] K. D. Paulsen, P. M. Meaney, and L. C. Gilman, *Alternative Breast Imaging: Four Model-based Approaches*, Springer Science & Business Media, 2004.

[15] D. Tajik, A. D. Pitcher, N. K. Nikolova, “Comparative study of the Rytov and Born approximations in quantitative microwave holography,” *Prog. Electromagn. B* , vol. 79, pp 1–19 , Jan. 2017.

[16] D. S. Shumakov, N. K. Nikolova, “Fast quantitative microwave imaging with scattered power maps,” *IEEE Trans. Microw. Theory Techn.* , vol. 66, no. 1, pp. 439–449, May 2017.

[17] W. Chew, *Waves and Fields in Inhomogeneous Media*, IEEE Press, 1995.

[18] J. Li, X. Wang, and T. Wang, ”On the validity of Born approximation,” *Prog. Electromagn. Res.*, vol. 107, pp. 219–237, Jan. 2010.

[19] T. M. Habashy, R. W. Groom, and B. R. spies, "Beyond the Born and Rytov approximations: a nonlinear approach to electromagnetic scattering," *J. Geophys. Res.*, vol. 98, no. B2, pp. 1759–1775, Feb. 1993.

[20] M. Slaney, A. C. Kak, L. E. Larsen, "Limitations of imaging with first-order diffraction tomography", *IEEE Trans. Microw. Theory Techn.*, vol. 32, no. 8, pp. 860–874, Aug. 1984.

[21] S. Tu, J. J. McCombe, D. S. Shumakov, and N. K. Nikolova, "Fast quantitative microwave imaging with resolvent kernel extracted from measurements," *Inverse Probl.*, vol. 31, no. 4, pp. 045007 (33 pp.), Mar. 2015.

[22] D. S. Shumakov, S. Tu, and N. K. Nikolova, "Fast quantitative microwave imaging based on measured point spread functions and inversion in real space," *IEEE AP-S/URSI Int. Symp. Antennas Propag.*, Jul. 2015, Vancouver, Canada.

[23] D. Tajik, J. R. Thompson, A. S. Beaverstone, and N.K. Nikolova, "Real-time quantitative reconstruction based on microwave holography", *IEEE Int. Symp. Antennas Propag. (APS/URSI)*, Fajardo, PR, pp. 851–852, Jun. 2016.

[24] D. Tajik, D. S. Shumakov, and N. K. Nikolova, "An experimental comparison between the Born and Rytov approximations in microwave tissue imaging," *IEEE Int. Microw. Symp.*, Honolulu, Hawaii, Jun. 2017.

[25] T. M. Grzegorczyk, P. M. Meaney, P. A. Kaufman, R. M. diFlorio-Alexander, and K. D. Paulsen, "Fast 3-D tomographic microwave imaging for breast cancer detection," *IEEE Trans. Med. Imag.*, vol. 31, no. 8, pp. 1584–1592, Aug. 2012.

[26] W. C. Chew and Y. M. Wang, "Reconstruction of two-dimensional permittivity distribution using the distorted Born iterative method," *IEEE Trans. Med. Imag.*, vol. 9, no. 2, pp. 218–225, Jun. 1990.

[27] M. A. Helvie, H.-P. Chan, D. D. Adler, and P. G. Boyd, "Breast thickness in routine mammograms: effect on image quality and radiation dose," *Am. J. Roentgenol.*, vol. 163, no. 6, pp. 1371–1374, Dec. 1994.

[28] T. A. Krouskop, T. M. Wheeler, F. Kallel, B. S. Garra, T. Hall, "Elastic moduli of breast and prostate tissues under compression," *Ultrason. Imag.*, vol. 20, no. 4, pp. 260–274, Oct. 1998.

[29] P. Wellman, R. H. Howe, E. Dalton, K. A. Kern, "Breast tissue stiffness in compression is correlated to histological diagnosis," Harvard BioRobotics Lab., Division Eng. Appl. Sci., Harvard Univ., Tech. Rep. 1999.

[30] A. S. Beaverstone, D. S. Shumakov, N. K. Nikolova, "Frequency-domain integral equations of scattering for complex scalar responses," *IEEE Trans. Microw. Theory Techn.*, vol. 65, no. 4, pp. 1120–1132, Apr. 2016.

[31] D. S. Shumakov, D. Tajik, A. S. Beaverstone, and N. K. Nikolova, "Study of practical limitations of real-time microwave imaging of tissue," *IEEE Int. Symp. Antennas Propag. (APS/URSI)*, San Diego, CA, Jul. 2017.

[32] Keysight (Agilent) Technologies, "Dielectric Probe Kit 200 MHz to 50 GHz, (85070E)", USA, 2014.

[33] P. M. Meaney, M. W. Fanning, T. Raynolds, et al., "Initial clinical experience with microwave breast imaging in women with normal mammography," *Acad. Radiol.*, vol. 14, no. 2, pp. 207–218, Mar. 2007.

[34] M. Lazebnik, D. Popovic, L. McCartney, C. B. Watkins, M. J. Lindstrom, J. Harter, *et al.*, "A large-scale study of the ultrawideband microwave dielectric properties of normal, benign and malignant breast tissues obtained from cancer surgeries," *Phys. Med. Bio.*, vol. 50, no. 20, pp. 6093–6115, Oct. 2007.

[35] R. K. Amineh, A. Trehan, and N. K. Nikolova, "TEM horn antenna for ultra-wide band microwave breast imaging," *Prog. Electromagn. Res. B*, vol. 13, pp. 59–74, Feb. 2009.

[36] Mini-Circuits, "Coaxial High Power Amplifier (ZVE-3W-83+)", USA.

[37] Mini-Circuits, "Low Noise, Wideband, High IP3 Monolithic Amplifier (PMA3-83LN+)", USA.

[38] A. S. Beaverstone, "An electronically-switched sensor array for microwave imaging," M.A.Sc. thesis, McMaster University, Hamilton, ON, Canada, 2015.

[39] A.S. Beaverstone and N.K. Nikolova, "Modeling and design of a switched transceiver array for tissue imaging," in *Numerical Electromagnetic and Multiphysics Modeling and Optimization (NEMO 2015)*, Aug. 2015, Ottawa, Canada.

[40] F. Foroutan and N.K. Nikolova, "Dynamic range of an active radio sensor for bias-switched arrays for microwave tissue imaging," in *IEEE AP-S/URSI Int. Symp. Antennas Propag.*, Jul. 2018, Boston, MA.

[41] D. Tajik, A. D. Pitcher, D. S. Shumakov, N. K. Nikolova, and J. W. Bandler, "Enhancing quantitative microwave holography in tissue imaging," in *Euro. Conf. Antennas Propag. (EUCAP)*, London, England, Apr. 2018.

[42] The MathWorks, Inc., "MATLAB 2016a", USA, 2016.

[43] Health Canada, "Guidelines on Exposure to Electromagnetic Fields from Magnetic Resonance Clinical Systems - Safety Code 26," Health Canada, 1987.

[44] Health Canada, "Limits of Human Exposure to Radiofrequency Electromagnetic Energy in the Frequency Range from 3 kHz to 300 GHz: Safety Code 6 ," Health Canada, 2015.

[45] A. Santorelli, M. V. Schueren, and M. Popovic, "SAR levels in microwave breast imaging: 3-D safety assessment with plane-wave illumniation," in *Asia Paci. Micro. Conf. (APMC)*, Melbourne, Australia, 2011.

CHAPTER 3

QUALITY CONTROL OF MICROWAVE EQUIPMENT FOR TISSUE IMAGING

Preface

This chapter is a reproduction of the following published article:

D. Tajik, J. Trac, and N. K. Nikolova, “Quality control of microwave equipment for tissue imaging,” in *IEEE J. Electromagn. RF Microw. Med. Bio.*, vol. 4, no. 1, pp. 52-60, Mar. 2020, doi: 10.1109/JERM.2019.2925599.

This article is open access under the Creative Commons 4.0 licensing agreement.

I designed the experimental setup, implemented the quantitative microwave holography (QMH) algorithm in code, performed the image reconstruction, evaluated the quality control performance, and wrote/edited the manuscript. Jessica Trac wrote the code implementing the quality control evaluation with my guidance. Natalia K. Nikolova assisted in the development of the quality control technique and edited the manuscript.

3.1 Introduction

Biomedical microwave imaging technology shows promise in a variety of applications such as breast cancer imaging, stroke detection, skin cancer diagnosis, bone and joint imaging, and many more [1–10]. Microwave imaging technology is nonionizing, compact, and low-cost, demonstrating clear advantages over current diagnostic technology. These advantages motivate interest in developing microwave imaging as an alternative or complimentary diagnostic modality.

To date, however, microwave imaging technology has not been deployed in clinical practice. This is primarily due to the highly nonlinear scattering phenomenon in tissue [11]. A large number of algorithms have been developed to address these complexities, including direct (linear) and iterative (nonlinear) approaches, all of which employ approximations of the scattering behaviour [12–16]. While many of these approaches have appeared successful in studies with simulated data, their translation to successful experimental studies is limited.

In our experience, the difficulties arising in translation to practice are not necessarily due to the image reconstruction approach. Rather, the experimental setup fails to reproduce the idealized simulated acquisition environment. Factors such as reflections from components in the measurement setup, positioning uncertainties, uncertainties in the performance of the antennas and the electronics, system noise and inadequate calibration all cause misleading results during image reconstruction. Evaluating the ability of the experimental setup to provide data of adequate quality is therefore an essential first step toward translating an imaging method to clinical practice.

The process of evaluating diagnostic equipment is commonplace in medical diagnostics. It is referred to as quality assurance or quality control (QC) [17–19]. One common QC evaluation protocol identifies the actual spatial resolution of the system by acquiring the system-specific point spread function (PSF) [17]. A PSF describes the impulse response of an imaging system. It can be acquired through the measurement of a small scattering object within a uniform background medium. Complex QC protocols based on multiple scattering probes generating unique PSFs have been created to account for the numerous system-specific influences on the actual image resolution [20, 21]. These protocols ensure that the estimated theoretical resolution is physically achieved.

Designing an experimental microwave imaging system to achieve a particular estimate of resolution starts with four fundamental factors: frequency bandwidth, antenna beamwidth, spatial sampling, and frequency (or temporal) sampling [11]. Such an estimate, however, depends on simplifying assumptions such as uniform and open background medium as well as far-zone modes of propagation. These assumptions do not hold in microwave tissue imaging, which is a typical near-field scenario. Such non-ideal background conditions along with the simplifying approximations in the forward model of scattering necessitate a QC protocol for evaluating the actual system-specific resolution of the imaging system.

Here, we propose a QC protocol for evaluating the ability of an experimental system to achieve the resolution necessary to identify critical tissue targets (e.g. cancer). The protocol uses an algorithm which computes the contrast-to-noise ratio (CNR) of a PSF at each measurement frequency. A case study is performed on the acquisition setup used for tissue-imaging experiments in [22]. The protocol also provides visual information to help determine the cause of poor CNR. The CNR QC protocol generates a metric which can be used to compare the current setup with similar acquisition systems.

3.2 Quality Control Protocol for Specified Resolution

The evaluated microwave imaging setup is a planar scanning system illustrated in Fig. 3.1. However, the QC protocol described next can be extended to systems employing cylindrical or hemispherical scanning surfaces and even surfaces of non-canonical shapes with nonuniform spatial sampling.

3.2.1 Point Spread Function Measurements

A point spread function (PSF) describes the impulse response of an imaging system. The PSF data consists of complex-valued scattering parameters from the measurement of a small scattering probe in a background medium, the volume of which includes the volume of a typical object-under-test (OUT). The protocol requires the measurement of two specifically constructed objects (phantoms) to derive the PSF: the reference object (RO) and the calibration object (CO).

The RO is a uniform phantom which fills the maximum capacity of the imaged volume V. Its measurement captures the incident-field response of the acquisition system, which includes system-specific features such as background clutter generated at interfaces between the equipment and surrounding air. The RO permittivity is designed to represent averaged tissue permittivity, weighted according to the percentage volume of each major tissue constituent in the anatomical model of the targeted organ. Note that the RO does not approximate complex tissue structures in the organ. Its purpose is to provide a baseline measurement in the absence of an OUT, which captures the dominant features of the system itself.

The CO phantom is comprised of: a) the uniform medium used in the RO measurement, and b) a scattering probe inserted within the uniform medium. The permittivity of the probe is selected to mimic a tissue structure of interest, e.g., a tumor. Its size corresponds to the desired spatial resolution. As an example, breast-cancer screening aims to detect sub-centimeter tumors [12]. Therefore, the size of the probe should be less than or equal to a cubic centimeter whereas the permittivity should approximate that of cancerous tissue. It is common for the permittivity of any given tissue type to have significant variance at any given frequency; e.g., for breast tumors, the real part of the relative permittivity may vary from 50 to 70 in the low-GHz range [23,24]. The scattering probe permittivity is selected within this range.

A variety of tissue mimicking mixtures exist for designing the RO and CO structures. Oil-based phantoms can be easily constructed and maintained [25–28]. Carbon rubber mixtures have also shown reasonable success at achieving the required permittivities while also having substantial lifespans [29–31]. It should also be noted that many commercially available products (both organic and non-organic) appear to be viable candidates as long as their complex permittivity matches adequately the expected averaged tissue permittivity. Materials such as lard, peanut butter, and jam have been used in microwave phantoms [32–34]. This is not a novel approach; MRI phantoms are regularly designed using household items, including jams, jellies, and egg whites [35,36].

The scattering probe is usually placed at the center of the imaged domain V, which is also the center of the RO and CO phantoms. We note that it is beneficial to place the scattering probe at different locations within the uniform phantom since different positions may correspond to somewhat different spatial resolution estimates as dictated by the width of the PSF. However, this comes at the cost of increased measurement effort. For the purposes of this work, CO measurements with a single probe position are carried out since the planar-scanning setup, where the antennas are aligned along boresight, features a PSF that is rather insensitive to the location of the probe.

3.2.2 Formulating the Point Spread Function

When the CO data set is measured, the total measured response is due to: a) scattered waves due to the scattering probe, and b) incident waves, which are independent of the probe and which form the baseline measurement. Only the scattered portion of the signal carries information about the scatterer; thus, it needs to be extracted from the total-field response. In the case of the PSF measurement, its scattered-field portion, $S_{ik}^{\mathrm{sc,PSF}}(\mathbf{r};f)$, can be extracted assuming a simple superposition of the incident and scattered field components [11]:

$$S_{ik}^{\mathrm{sc,PSF}}(\mathbf{r};f) \approx S_{ik}^{\mathrm{tot,CO}}(\mathbf{r};f) - S_{ik}^{\mathrm{RO}}(\mathbf{r};f)\,. \tag{3.1}$$

Here, $S_{ik}^{\mathrm{tot,CO}}(\mathbf{r};f)$ is the total measured response of the CO, and $S_{ik}^{\mathrm{RO}}(\mathbf{r};f)$ is the measured response of the RO.

The subtraction of the RO data from the total data aims at de-embedding the undesirable impact of the background measurement, which, in practice, is neither

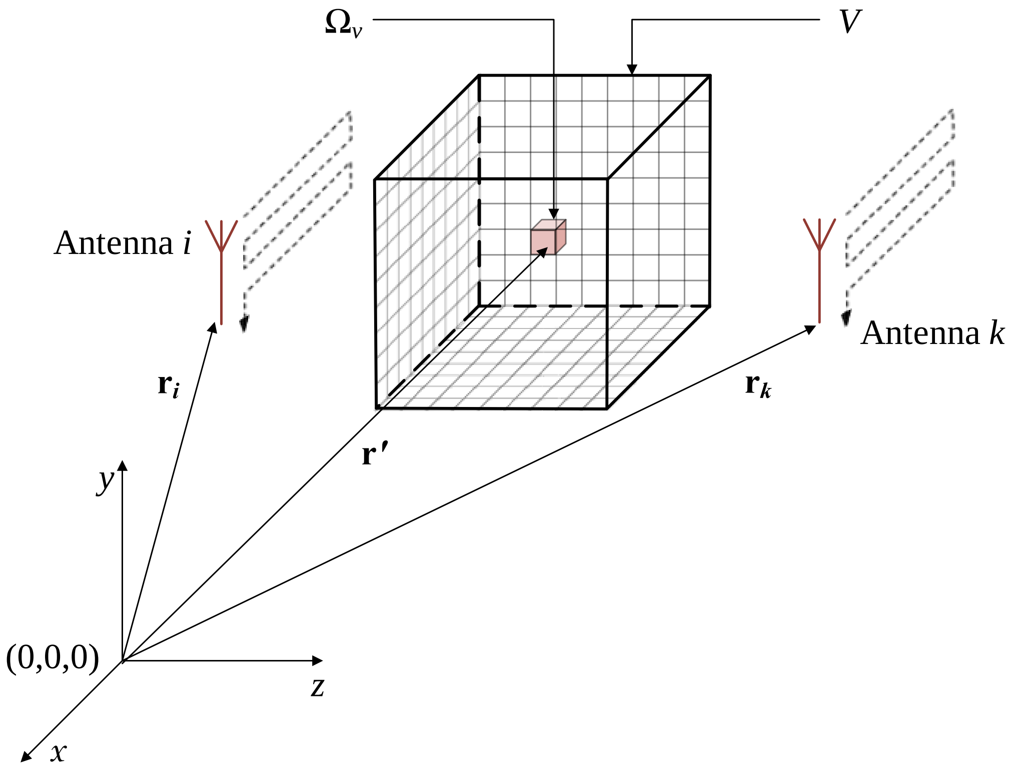

Figure 3.1: Illustration of a planar acquisition setup. The antennas are scanned mechanically along the two parallel acquisition planes on both sides of the imaged volume V. If antennas i and k are both used as transmitting (Tx) and receiving (Rx) antennas, then the scattering parameters S_{ii}, S_{ik}, S_{ki}, S_{kk} are acquired as 2D complex-valued data sets at each frequency. Figure adapted from [37].

uniform nor perfectly repeatable. This issue is a major contributor to the measurement uncertainties of the particular system. The RO (or baseline) measurement is commonplace in microwave imaging and it is a mandatory step in the calibration of the system before proceeding with imaging an OUT [11].

Eq. (3.1) is a simple and widely used approach to the extraction of the scattered portion of a response. It is based on the first-order Born approximation [11]. However, using Rytov's approximation of scattering [11] is equally effective in the case of a PSF response. Details on the implementation of the Rytov data approximation are found in [32, 37, 38].

3.2.3 Contrast-to-Noise Ratio of the PSF

To evaluate the PSF measurement, each data set (for a given antenna pair and frequency) is divided into three regions of interest, as shown in Fig. 3.2: the signal region (A_s), the background region (A_b), and the exclusion region (A_e). The signal region A_s is the location where the majority of the scattered signal power is located. It is defined as all the voxels where the signal strength is within the 3 dB level relative to the maximum signal magnitude. The background region A_b is defined as the largest possible region containing no signal from the scattering probe. The exclusion region A_e is the region where the signal and noise components are difficult to separate. In A_e, ripple-like diffraction effects exists and they must be avoided in the CNR calculations described next.

In the context of this work, the signal-to-noise ratio (SNR) of a data set should be defined as

$$\mathrm{SNR}(f) = \frac{\mathrm{average}\left(S_{ik}^{\mathrm{tot,CO}}(A_\mathrm{s}, f)\right)}{\mathrm{std}(S_{ik}^{\mathrm{tot,CO}}(A_\mathrm{b}, f))}, A_\mathrm{s}, A_\mathrm{b} \in D \tag{3.2}$$

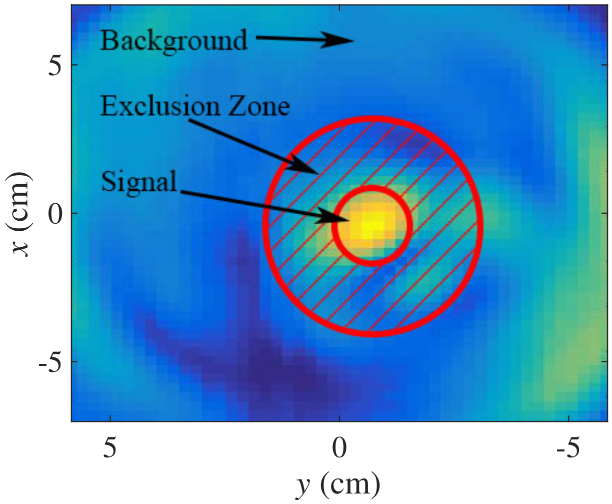

Figure 3.2: Magnitude plot of acquired 2D PSF data at one frequency. Three regions are highlighted: a) the signal region, b) the background region, and c) the exclusion region. Image adapted from [22].

where $S_{ik}^{\text{tot,CO}}(A_\text{s})$ is the total-field response in the signal region A_s contained within the scanned 2D domain D and $S_{ik}^{\text{tot,CO}}(A_\text{b})$ is the total-field response in the background region A_b. Here, std denotes the standard deviation function. As shown in [39], the average value and the standard deviation are calculated to produce real-positive values as:

$$\text{average}(\boldsymbol{d}) = \left| \frac{1}{N} \sum_{i=1}^{N} d_i \right|, \tag{3.3}$$

$$\text{std}(\boldsymbol{d}) = \left(\frac{1}{N-1} \sum_{i=1}^{N} |d_i - \bar{d}|^2 \right)^{\frac{1}{2}}, \bar{d} = \frac{1}{N} \sum_{i=1}^{N} d_i, \tag{3.4}$$

where d_i is a single measurement at a particular location in the specified region (an element of the data vector $\boldsymbol{d}$), and N is the number of elements in $\boldsymbol{d}$.

In imaging, SNR can be a misleading metric, especially in cases where the incident-field component is stronger than the scattered-field component. This is because the reconstruction algorithm works with a signal which, ideally, contains only a scattered-field component. Therefore, using the scattered-field portion of the data sets is preferable.

Unfortunately, the incident-field response cannot be de-embedded from the PSF data completely, in part due to the near-field nature of the measurement, for which the superposition assumption in Eq. (3.1) does not hold strictly. The measurement uncertainties have a detrimental effect as well. Thus, instead of the SNR, a similar metric, referred to as the contrast-to-noise ratio (CNR), is preferable [22]:

$$\mathrm{CNR}(f) = \frac{\mathrm{average}(S_{ik}^{\mathrm{sc,PSF}}(A_{\mathrm{s}}, f)) - \mathrm{average}(S_{ik}^{\mathrm{sc,PSF}}(A_{\mathrm{b}}, f))}{\mathrm{std}(S_{ik}^{\mathrm{sc,PSF}}(A_{\mathrm{b}}, f))}, \tag{3.5}$$

$$A_{\mathrm{s}} \in D, A_{\mathrm{b}} \in D.$$

Here, the average and the standard deviation are computed using Eq. (3.3) and Eq. (3.4), respectively. The CNR measures the contrast between the scattered signal averaged over the signal region A_{s} and that averaged over the background region A_{b}, relative to the random contrasts (artifacts defining the data noise) that appear in the background region. Thus, CNR is insensitive to the incident-field responses which may not be removed completely during the de-embedding process.

After calculating the CNR for all data sets, a cut-off CNR is applied to determine whether a data set satisfies the QC requirements. Depending on the image-reconstruction algorithm, different CNR thresholds can be applied. In the case of quantitative microwave holography, a 3-dB threshold is suitable for determining whether the data quality is sufficient to accurately image scattering objects of the size and contrast similar to those of the scattering probe [22]. In a situation where

50% of the PSF data sets have a CNR below 3 dB, the system-specific resolution is deemed insufficient. In such cases, visual inspection of the two measured data sets (CO and RO) should be performed to identify system faults. As demonstrated in the case study described in section 3.3, such system faults can be usually remedied with simple modifications of the setup. A metric describing the overall system quality can be acquired from the mean CNR.

3.2.4 Quality Assurance Protocol

The CNR-based QC protocol can be summarized as follows:

1. Perform a measurement of the RO (uniform tissue mimicking phantom) to acquire $S_{ik}^{\mathrm{RO}}(\mathbf{r}, f)$.
2. Perform a measurement of the CO (uniform tissue mimicking phantom identical to the RO with a scattering probe embedded in the center) to acquire $S_{ik}^{\mathrm{tot,CO}}(\mathbf{r}, f)$.
3. Acquire the PSF $S_{ik}^{\mathrm{sc,PSF}}(\mathbf{r}, f)$ using Eq. (3.1).
4. At each frequency, identify the three regions of interest, referred to as the signal region A_{s}, the exclusion region A_{e}, and the background region A_{b}
5. Compute the CNR of each PSF data set using (3.5).
   (a) If 50% of the PSF data sets have a CNR above the 3 dB threshold, the acquisition setup has sufficient quality at the particular system-specific resolution.

(b) If 50% of the PSF frequencies have a CNR below the 3 dB threshold, the acquisition setup has insufficient quality. Perform visual inspections of the CO and RO data. Return to step 1) after the experimental setup has been improved.

3.2.5 Algorithmic Implementation

An algorithmic approach is implemented in MATLAB [40] to automate the division of a PSF data set into *signal*, *background* and *exclusion* regions and to compute the CNR (available online [41]). Details of the implementation are provided in [42]. The algorithm operates on the PSF data obtained with Eq. (3.1).

To identify the signal region, the maximum signal strength is located, followed by the localization of all pixels of signal strength within -3 dB of the maximum. These pixels are organized into clusters. If multiple clusters are detected, the cluster closest to the center of the image is selected. The cluster selection uses a rectangular search region, which is centered within the acquisition area and has an initial size of 25% of the length and width of that area. If a cluster is not found in the initial search region, the algorithm increases the region in 5% increments until it reaches the size of the image. A warning is issued if the cluster is located outside of the initial search region since this implies that the scattering probe is not centered in the imaged volume or that significant measurement artifacts corrupt the PSF data. If the cluster approach fails to identify A_{s}, a backup approach defines the signal region as a circle with a user-defined radius, centered on the maximum-strength pixel.

Note that the cluster selection is prone to errors when a data set is corrupted by strong measurement artifacts. The baseline measurement of the uniform RO phantom may produce a nonuniform RO data set due to reflections from interfaces and interactions with the setup. These deviations from uniformity are referred to as measurement artifacts. When these artifacts are strong, they are not removed adequately via subtraction (see (3.1)), due to positioning errors, temperature changes, and other sources of uncertainty as discussed in Section 3.3. As a result, multiple clusters of comparable strength may be present in the PSF, leading to uncertainty whether the algorithm has properly identified the signal region. In these scenarios, the CNR is always low (at or below 0 dB) due to the large variance in the background region. Thus, with poor quality data sets, the likelihood of the algorithm selecting the wrong "signal" cluster increases but this has little impact on the CNR which remains low regardless of the cluster selection.

Once the signal region A_{s} is identified, the exclusion region A_{e} is defined. This is accomplished by iteratively expanding a circular area which is centered on and is larger than A_{s}. The algorithm evaluates whether the variance of the signal ($\mathrm{variance}(A) = \mathrm{std}(A)^2$) outside of A_{e}, i.e., within A_{b}, changes by more than a user-defined value. This user-defined value is based on the requirement that the percentage change in the signal variance within A_{b} must not exceed the percentage change in the size of A_{e}. For example, if the current iterate of A_{e} is expanded by 5% of the size of the acquisition area, and the variance in A_{b} changes by less than 4%, the search is considered to have converged and the previous iterate for the size of A_{e} is selected. The assumption is that the majority of the scattering signal due to the probe is contained within A_{s} and A_{e} whereas the background region A_{b} contains only noise, the variance of which does not depend on its size. The example percentage values above have been selected empirically for the planar scanning used in [22]. They can be redefined for a different setup as long as A_{b} contains minimum amount of diffraction effects. Once A_{s} and A_{b} are defined, (3.5) calculates the CNR for the data set.

3.3 Case Study

A planar raster scanning system, utilizing one transmitting TEM horn antenna [43] and 9-element receiving bowtie array [44], is evaluated for the purposes of breast-phantom imaging experiments performed in [22]. For simplicity, only the evaluation of the central antenna of the bowtie array is shown here since all antennas achieved similar CNR values. The frequency range is from 3 GHz to 8 GHz, in 100 MHz increments. The imaged volume is a 5 litre plexiglass ($\epsilon_r \approx 2 - \mathrm{i}0.1$) tray, the walls of which are 4 mm thick. It holds the embedding medium ($\epsilon_r \approx 10 - \mathrm{i}5$) and a compressed breast-tissue phantom. The antennas are connected to an R3970 Advantest 16 port RF switch and an Advantest 3770 Advantest vector network analyzer. An RF-Lambda 8-W power amplifier is connected to the transmitting antenna. The scanning system is placed within a custom microwave-absorber shielded chamber. The acquisition chamber can be seen in Fig. 3.3a. The acquisition setup aims at detecting cancerous tissue approximately 1 cm^3 in size. In the case of planar scanning, the far-field resolution limits along *range* (z) and *cross-range* (x,y) are described by [11]:

$$\delta z \approx \frac{c_{\mathrm{b}}}{2 \cdot \mathrm{BW}}, \tag{3.6}$$

and

$$\Delta\zeta_{\max} \approx \frac{\lambda_{\min}}{4 \sin \alpha_{\max}}, \zeta \equiv x, y \tag{3.7}$$

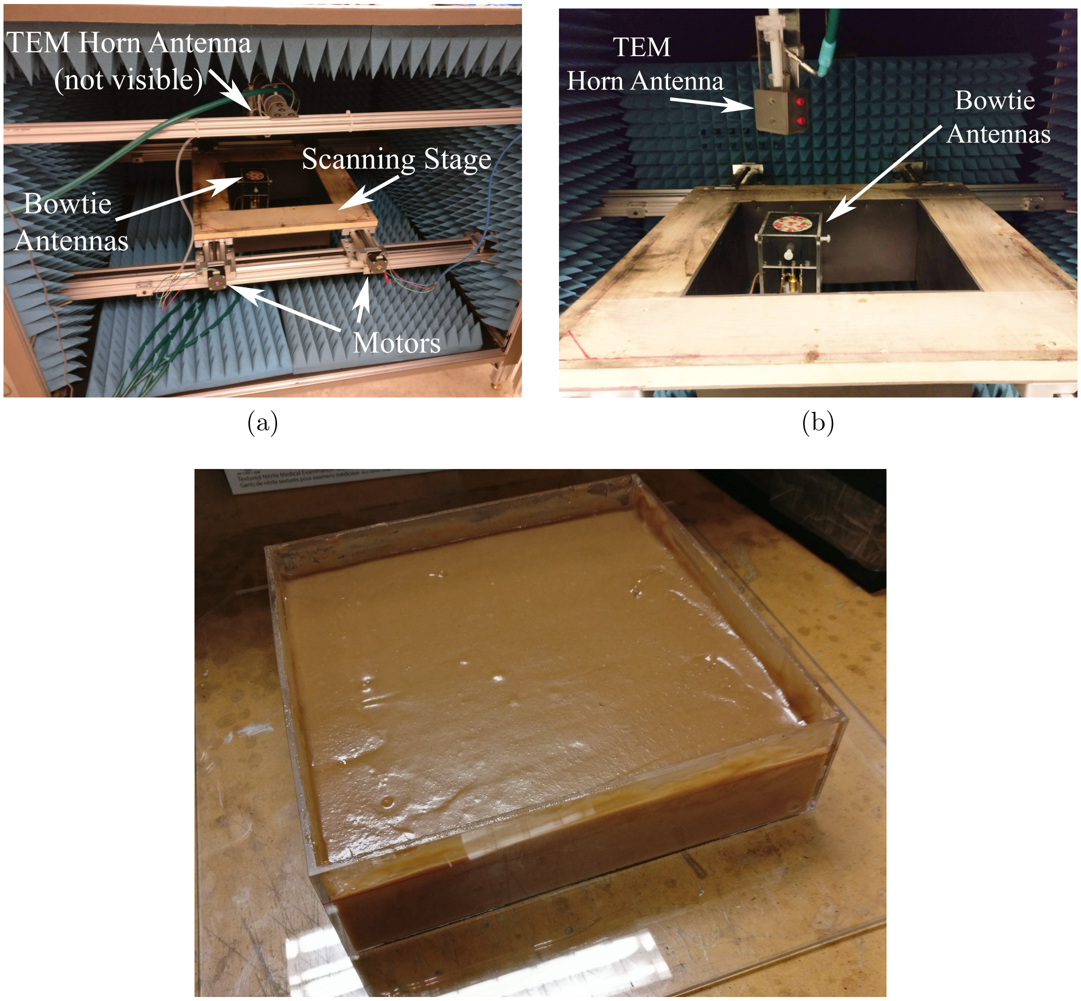

(a) (b)

(c)

Figure 3.3: Photos of the initial experimental setup: (a) the raster-scanning acquisition chamber in which the tray is placed, (b) inside the acquisition chamber, showing the TEM horn antenna and bowtie array aligned along boresight, and (c) a tray containing a uniform medium for the RO measurement.

where c_{b} is the speed of light in the background medium, BW is the frequency bandwidth, $\lambda_{\min}$ is the shortest wavelength of the radiation in the background medium, and $\alpha_{\max}$ is the largest angle of arrival (i.e. viewing angle) at which the scattered signal can be received. In practice, Eq. (3.7) is often approximated as $\Delta\zeta_{\max} = \frac{\lambda_{\min}}{2}$, which corresponds to an angle of arrival of 30° – a limit attributed to the antenna beamwidth or the aperture size, whichever results in a smaller $\alpha_{\max}$. In tissue, this assumption is reasonable regardless of the antenna beamwidths, bearing in mind that larger angles imply longer signal paths, leading to increasing signal attenuation. For this experiment, the range and cross-range theoretical resolution limits are estimated as $z \approx 9.5$ mm and $\zeta \approx 6$ mm.

To verify the acquisition setup quality, the CNR QC protocol is performed. The permittivity of the uniform medium in the RO is based on a Type-2 breast, which is comprised of mostly fat with scattered fibroglandular tissue. The averaged permittivity of this tissue is expected to be $\epsilon_r \approx 10 - \mathrm{i}5$ at the central frequency of 5 GHz. The embedding medium, which is constructed from a mixture of peanut butter and jam (PBJ), is designed to achieved this permittivity [34]. The resultant mixture is measured with a Keysight (formerly Agilent) Technologies dielectric slim form probe (85070E) to validate the mixture permittivity. The CO is constructed with the same uniform embedding medium, with the addition of a cylindrical dielectric scattering probe (diameter = 1 cm, height = 1 cm, $\epsilon_r \approx 50 - \mathrm{i}0.01$) placed in the center of the tray.

The CNR QC protocol described in Section 3.2 is applied and the initial CNR values of the central bowtie-array antenna are plotted *versus* frequency in Fig. 3.4. Most of the PSF data have CNR values below the 3 dB cutoff, indicating that the

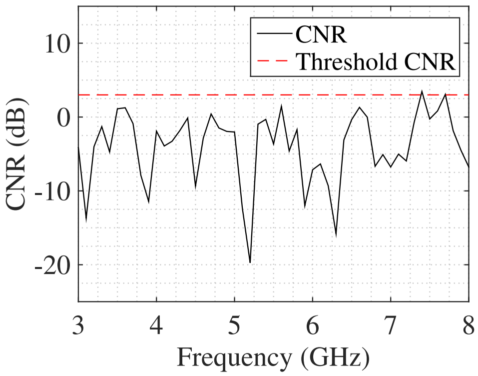

Figure 3.4: Plot of the CNR values of the initial experimental setup. Most of the frequencies have CNR below the 3 dB threshold, indicating insufficient resolution for a 1-cm^3 scattering probe. The mean CNR is -2.13 dB.

acquisition setup has insufficient resolution. The mean CNR of the data set is -2.13 dB. An example PSF (with the RO response de-embedded) at 5.4 GHz is shown in Fig. 3.5a. Large interference patterns appear to track along the x-axis. The strength of one of these patterns is actually greater than that of the scattering probe (see the center of the domain). These interference patterns are also very apparent in the CO and RO data sets shown in Figs. 3.5b and 3.5c, respectively. The background de-embedding procedure through superposition (see Eq. (3.1)) fails to completely remove the interference patterns, possibly due to slight position misalignment of the tray in the CO and RO measurements. While positional error is important, such a significant interference pattern hints at a poor experimental design where improvement is necessary in terms of suppressing reflections in the background environment.

The cause of the interference is identified by the interference patterns aligned with the edges of the tray. Significant contrast exists between the embedding medium ($\epsilon_r \approx 10 - \text{i}5$) and the plexiglass walls ($\epsilon_r \approx 1$). This contrast induces significant reflections which produce the interference pattern visible in the CO and RO data

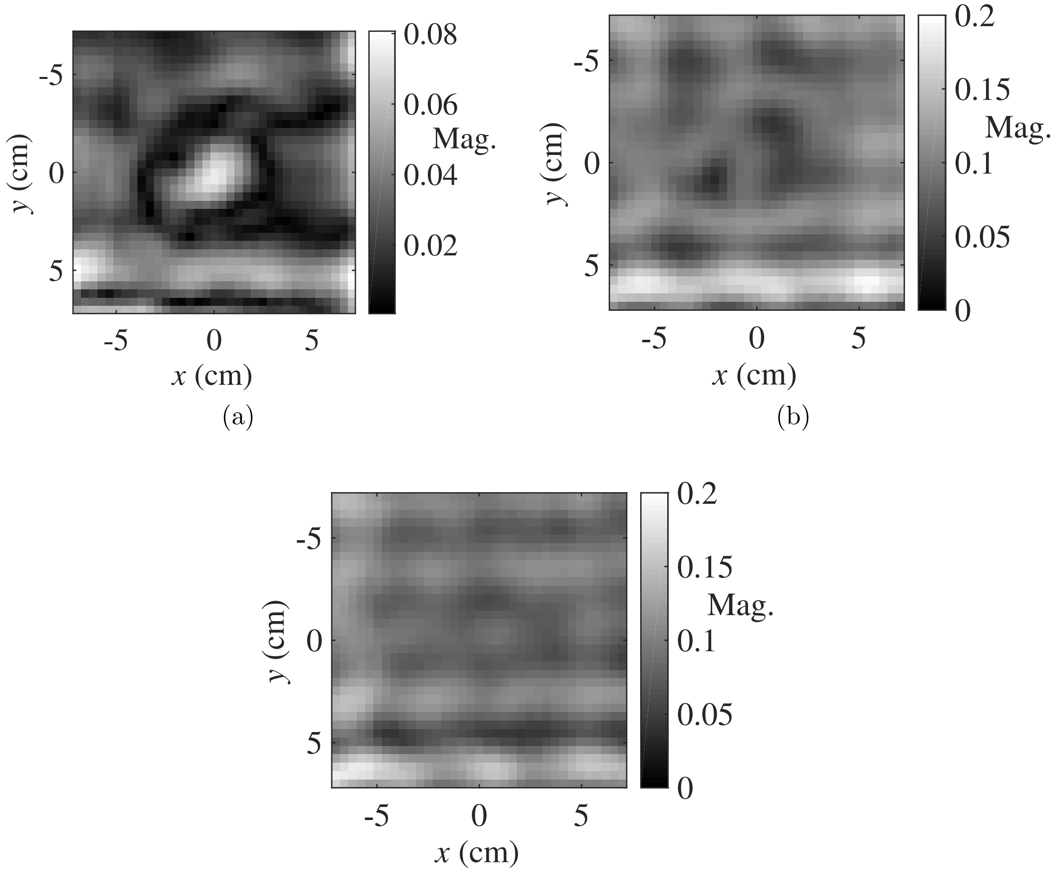

(a)

(b)

(c)

Figure 3.5: Magnitude of the (a) PSF, (b) CO, and (c) RO data at 5.4 GHz. The PSF data is obtained by subtracting the RO from from the CO data.

sets.

To suppress reflections at the tray walls, microwave absorbing foam is placed around the tray. The foam is well matched to the low permittivity of the plexiglass and it leads to significant reduction of the background interference patterns. Fig. 3.6 depicts the tray containing uniform embedding medium with the microwave absorbing foam. The RO and CO measurements are performed again.

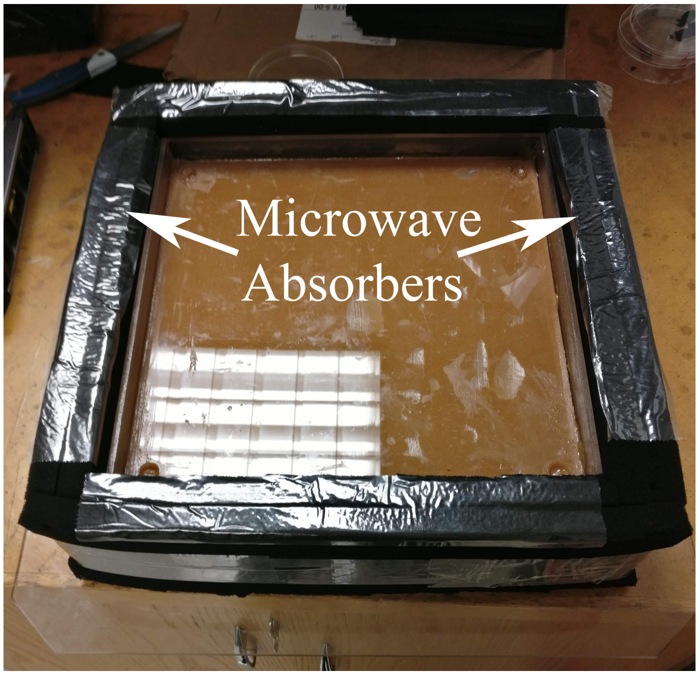

Figure 3.6: Photo of the tray, showing the microwave absorbers that reduce reflections from the interface at the plexiglass walls.

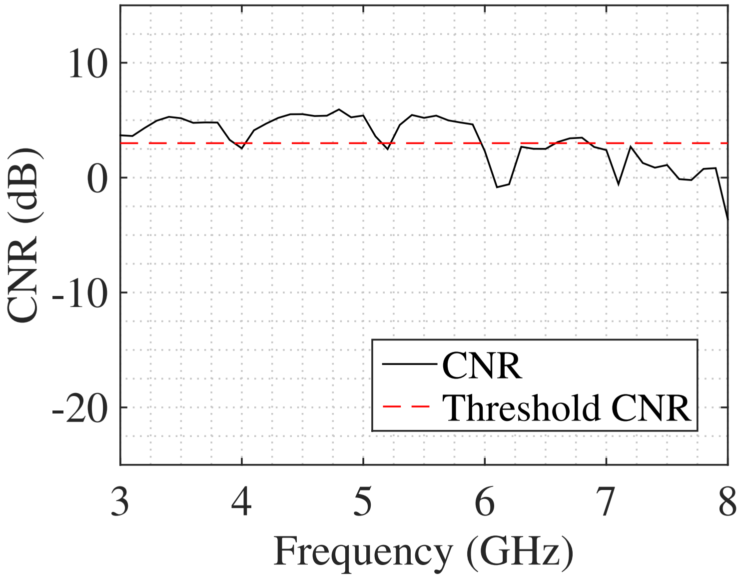

Figure 3.7: Plot of the CNR values of the setup using microwave absorbers. Over 50% of the frequencies have CNR above 3 dB indicating that the system has sufficient resolution. As expected, the CNR at the higher frequencies is lower due to the increased signal attenuation – an effect not observed in Fig. 3.4 due to the overwhelming impact of background interference patterns. The mean CNR is 3.73 dB.

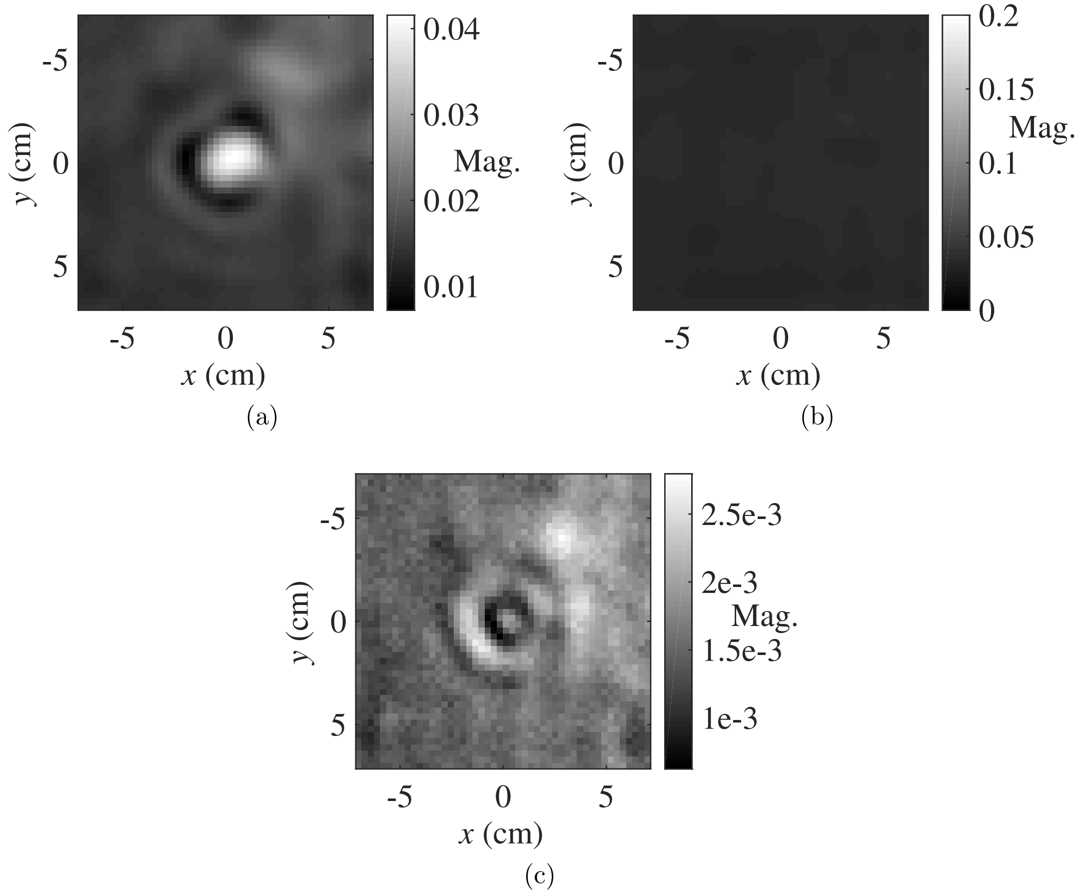

(a) (b) (c)

Figure 3.8: (a) Magnitude image of the PSF at 5.4 GHz after the addition of microwave absorbers to the tray in the experimental setup, (b) magnitude image of the RO after the addition of microwave absorbers to the tray in the experimental setup. It is scaled to match Fig. 3.5c), and (c) Magnitude image of the PSF at 7.1 GHz after the addition of microwave absorbers to the tray in the experimental setup. Note that the CNR is lower due to significant contributions remaining in the background region of the PSF.

The CNR QC protocol is applied to the PSF data sets obtained from the new CO and RO data sets. The results are shown in Fig. 3.7. The CNR is now above the cutoff threshold of 3 dB for more than 50% of the frequencies. The mean CNR across all frequencies is 3.73 dB. At the same example frequency of 5.4 GHz, the PSF is far more clearly defined and no major interference pattern is visible (see Fig. 3.8a).

Indeed, the RO data at 5.4 GHz (see Fig. 3.8b, scaled to match Fig. 3.5c) no longer contains significant interference patterns. These results confirm that the modified acquisition setup has sufficient system-specific resolution.

Fig. 3.8c shows the magnitude of the PSF measured at 7.1 GHz, which has a CNR below the threshold. Note the presence of a measurement artifact in the top right of the image, which is stronger than that in Fig. 3.8a. This leads to the reduced CNR. Fig. 3.8c also demonstrates the reduction of the overall signal strength as well as the size of the probe's scattering footprint at higher frequencies. It highlights a key trade-off in microwave tissue imaging: higher frequencies facilitate higher resolution at the cost of lower signal strength.

Utilizing quantitative microwave holography [37,45], a Fourier-based direct-inversion technique, image reconstruction of a breast tissue phantom has been performed with the modified acquisition setup [22]. The improved acquisition setup lead to successful imaging results discussed in detail in [22]. There, data filtering is applied to remove frequencies below the CNR threshold, leading to higher quality images.

3.4 Discussion and Conclusions

A quality control (QC) approach for the evaluation of the system-specific resolution of an experimental setup for microwave tissue imaging is proposed. It utilizes the measurement of two separate structures (phantoms), and generates a system-specific point-spread function (PSF). The contrast-to-noise ratio (CNR) of the PSF is then calculated to determine if the signal quality is sufficient. If over 50% of the PSF data set have a CNR below 3 dB, the system has insufficient signal quality to resolve objects of size similar to that of the scattering probe. An algorithm evaluating the

CNR is provided [41, 42], and a case study is performed with a planar microwave imaging acquisition used in [22]. The result demonstrates that the CNR QC protocol is able to identify insufficient resolution and to provide evidence pointing to the cause of poor signal quality. Addressing these causes leads to significant improvement of the system-specific resolution.

The CNR QC protocol generates a metric (mean CNR) which can be used to compare similar system implementations. This approach can be extended to multistatic setups in other antenna configurations including cylindrical and hemispherical arrangements. To implement the QC protocol, similar RO and CO structures need to be constructed and measured, where the permittivities and the probe's size would depend on the intended application. The scattering probe is usually placed in the center of the imaged volume. This placement does not provide an accurate resolution estimate for every position within the imaged domain, but represents a typical value which can be used to evaluate and compare imaging setups.

It is emphasized that the CNR metric must operate on the scattered portion of the CO response, which estimates the probe's impact on the measured responses and thus tests the sensitivity of the acquisition system to a very small source of scattering. There are reconstruction methods that operate on the scattered portion of the responses (e.g., microwave holography and synthetic focusing) and there are those that may operate on the total responses (e.g., microwave tomography). In both cases, however, the ability to measure reliably the difference between the background (the RO) response and that of the same background in the presence of a probe (the CO) is critical to the success of the reconstruction.

Finally, the protocol's definitions of *signal* and *background* regions in a PSF data set have been proposed and tested here for the case of planar acquisition surfaces. These definitions need to be modified for the cases of cylindrical and spherical acquisition surfaces. The modifications must preserve the physical meaning behind the concept so that *the signal region captures most of the scattering occurring at the probe* whereas *the background region captures most of the noise, clutter and uncertainty* occurring in the setup. For example, in the case of a spherical surface and with the probe being at the center of the imaged volume, the signal region would expand to include the PSF values at all sampling positions on this surface because they are equidistant from the probe. At the same time, the background region would also include all of these positions so that the PSF variance is extracted to give a measure of the deviation from the ideal uniform PSF distribution over the spherical surface. The cylindrical case would have both the signal and the background regions extending over all angular positions of the PSF whereas the vertical (axial) positions would require the separation of the two with a 1D variant of the method described in Section 3.2.

A number of simple steps have been suggested to improve an experimental setup if the CNR QC protocol identifies an insufficient system-specific resolution. The addition of microwave absorbers around the antennas and other neighbouring structures reduces the impact of background clutter. Also, avoiding the use of system components such as plates and trays, which have high permittivity contrast with the objects being imaged, is beneficial. The use of an embedding medium for tissue measurements is very important since air-to-skin interfaces cause significant reflections and lower the signal penetration into the tissue.

Future work aims at two major objectives: a) methods for identifying the sources of error from measurement artifacts and b) developing and testing standard quality-control metrics for all microwave tissue imaging approaches, including those employing cylindrical and spherical acquisition surfaces. The first objective addresses a variety of errors including positional error, cabling/antenna uncertainties, calibration error, and system noise. The second objective requires extensive testing to ensure fair comparison among all acquisitions, and is entirely driven by the quality of the measured data, independent of the reconstruction method (i.e., how these data are processed).

In addition, designing calibration objects with several uncoupled scattering probes of varying sizes and contrasts can provide secondary metrics which more precisely characterize the system. A common QC metric in MRI evaluates the low-contrast detection capability using low-contrast probes [17]. Standardized QC structures have also been constructed for MRI, which utilize a number of different scattering probes of different shapes and contrasts. The design of similar QC structures for microwave tissue-imaging systems would provide a standardized tool for the evaluation and comparison of emerging prototypes, thus pushing this technology towards successful implementation in clinical settings.

Acknowledgment

We acknowledge the support of the Natural Sciences and Engineering Research Council of Canada (NSERC).

REFERENCES

[1] E. C. Fear, P. M. Meaney, and M. A. Stuchly, “Microwaves for breast cancer detection?” *IEEE Potentials*, vol. 22, no. 1, pp. 12–18, Feb. 2003.

[2] E. Porter, M. Coates, and M. Popović, “An early clinical study of time-domain microwave radar for breast health monitoring,” *IEEE Trans. Biomed. Eng.*, vol. 63, no. 3, pp. 530–539, Mar. 2016.

[3] D. O’Loughlin, M. O’Halloran, B. M. Moloney, M. Glavin, E. Jones, and M. A. Elahi, “Microwave breast imaging: Clinical advances and remaining challenges,” *IEEE Trans. Biomed. Eng.*, vol. 65, no. 11, pp. 2580–2590, Nov. 2018.

[4] D. Wörtge, J. Moll, V. Krozer, B. Bazrafshan, F. Hübner, C. Park, and T. J. Vogl, “Comparison of X-ray-mammography and planar UWB microwave imaging of the breast: First results from a patient study,” *Diagnostics*, vol. 8, no. 3, Aug. 2018.

[5] D. Ireland, K. Bialkowski, and A. Abbosh, “Microwave imaging for brain stroke detection using born iterative method,” *IET Microw. Antennas Propag.*, vol. 7, no. 11, pp. 909–915, Aug. 2013.

[6] R. Scapaticci, L. D. Donato, I. Catapano, and L. Crocco, “A feasibility study on microwave imaging for brain stroke detection,” *Prog. Electrom. Res. B*, vol. 40, pp. 305–324, Mar. 2012.

[7] I. Bisio, A. Fedeli, F. Lavagetto, M. Pastorino, A. Randazzo, A. Sciarrone, and E. Tavanti, “A numerical study concerning brain stroke detection by microwave

imaging systems," *Multimedia Tools and Applications*, vol. 77, no. 8, pp. 9341–9363, Apr. 2018.

[8] P. Mehta, K. Chand, D. Narayanswamy, D. G. Beetner, R. Zoughi, and W. V. Stoecker, "Microwave reflectometry as a novel diagnostic tool for detection of skin cancers," *IEEE Trans. Instrum. Meas.*, vol. 55, no. 4, pp. 1309–1316, Aug. 2006.

[9] S. M. Salvador, E. C. Fear, M. Okoniewski, and J. R. Matyas, "Exploring joint tissues with microwave imaging," *IEEE Trans. Microw. Theo. Tech.*, vol. 58, no. 8, pp. 2307–2313, Aug. 2010.

[10] P. M. Meaney, D. Goodwin, A. H. Golnabi, T. Zhou, M. Pallone, S. D. Geimer, G. Burke, and K. D. Paulsen, "Clinical microwave tomographic imaging of the calcaneus: A first-in-human case study of two subjects," *IEEE Trans. Biomed. Eng.*, vol. 59, no. 12, pp. 3304–3313, Dec. 2012.

[11] N. K. Nikolova, *Introduction to Microwave Imaging.* Cambridge University Press, 2017.

[12] ——, "Microwave imaging for breast cancer," *IEEE Microw. Mag.*, vol. 12, no. 7, pp. 78–94, Dec. 2011.

[13] R. Conceiçao, M. O'Halloran, and J. Mohr, *An Introduction to Microwave Imaging for Breast Cancer Detection.* Springer, Jul. 2016.

[14] A. C. Kak and M. Slaney, *Principles of Computerized Tomographic Imaging.* Society for Industrial and Applied Mathematics, 1988.

[15] S. Kwon and S. Lee, “Recent advances in microwave imaging for breast cancer detection,” *Int. J. Biomed. Imag.*, vol. 2016, p. 26 pages, Oct. 2016.

[16] K. D. Paulsen, P. M. Meaney, and L. C. Gilman, *Alternative Breast Imaging: Four Model-based Approaches*, 2004.

[17] M. J. Firbank, R. M. Harrison, E. D. Williams, and A. Coulthard, “Quality assurance for MRI: practical experience.” *British J. Radiol.*, vol. 73, no. 868, pp. 376–383, 2000, pMID: 10844863.

[18] R. R. Price, L. Axel, T. Morgan, R. Newman, W. Perman, N. Schneiders, M. Selikson, M. Wood, and S. R. Thomas, “Quality assurance methods and phantoms for magnetic resonance imaging: Report of AAPM nuclear magnetic resonance Task Group No. 1,” *Med. Phys*, vol. 17, no. 2, pp. 287–295, Apr. 1990. [Online]. Available: https://aapm.onlinelibrary.wiley.com/doi/abs/10.1118/1.596566

[19] R. T. Droege, “A quality assurance protocol for CT scanners,” *Radiol.*, no. 146, pp. 244–246, Jan. 1983.

[20] T. M. Ihalainen, N. T. Lönnroth, J. I. Peltonen, J. K. Uusi-Simola, M. H. Timonen, L. J. Kuusela, S. E. Savolainen, and O. E. Sipilä, “MRI quality assurance using the ACR phantom in a multi-unit imaging center,” *Acta Oncologica*, vol. 50, no. 6, pp. 966–972, 2011.

[21] P. Judy, S. Balter, D. Bassano, E. McCullough, J. Payne, and L. Rothenberg, *Phantoms for Performance Evaluation and Quality Assurance of CT scanners*, 1st ed., American Association of Physicists in Medicine (AAPM), 1977.

[22] D. Tajik, J. Trac, and N. K. Nikolova, "Spatial resolution evaluation of a microwave system for breast cancer screening," in *13th Euro. Conf. Antennas Propag. EuCAP*. IEEE, Jun. 2019, pp. 1–5.

[23] A. Martellosio, M. Pasian, M. Bozzi, L. Perregrini, A. Mazzanti, F. Svelto, P. E. Summers, G. Renne, L. Preda, and M. Bellomi, "Dielectric properties characterization from 0.5 to 50 ghz of breast cancer tissues," *IEEE Trans. Microw. Theory Tech.*, vol. 65, no. 3, pp. 998–1011, Mar. 2017.

[24] M. Lazebnik, D. Popovic, L. McCartney, C. B. Watkins, M. J. Lindstrom, J. Harter, S. Sewall, T. Ogilvie, A. Magliocco, T. M. Breslin, W. Temple, D. Mew, J. H. Booske, M. Okoniewski, and S. C. Hagness, "A large-scale study of the ultrawideband microwave dielectric properties of normal, benign and malignant breast tissues obtained from cancer surgeries," *Phys. Med. Biol.*, vol. 52, no. 20, p. 6093, Oct 2007. [Online]. Available: http://stacks.iop.org/0031-9155/52/i=20/a=002

[25] M. O'Halloran, S. Lohfeld, G. Ruvio, J. Browne, F. Krewer, C. O. Ribeiro, V. C. I. Pita, R. C. Conceicao, E. Jones, and M. Glavin, "Development of anatomically and dielectrically accurate breast phantoms for microwave imaging applications," in *Proc. SPIE 9077, Rad. Sens. Tech. XVIII*, vol. 9077, 2014.

[26] N. Joachimowicz, C. Conessa, T. Henriksson, and B. Duchêne, "Breast phantoms for microwave imaging," *IEEE Antennas Wireless Propag. Let.*, vol. 13, pp. 1333–1336, Jul. 2014.

[27] Y. Baskharoun, A. Trehan, N. K. Nikolova, and M. D. Noseworthy, "Physical phantoms for microwave imaging of the breast," in *2012 IEEE Topical Conf.*

Biomed. Wireless Tech. Networks Sens. Sys. (BioWireleSS), Jan. 2012, pp. 73–76.

[28] A. Trehan, "Numerical and physical models for microwave breast imaging," Master of Applied Science Thesis, McMaster University, 2009.

[29] J. Garrett and E. Fear, "Stable and flexible materials to mimic the dielectric properties of human soft tissues," *IEEE Antennas Wireless Propag. Let.*, vol. 13, pp. 599–602, Mar. 2014.

[30] A. Santorelli, O. Laforest, E. Porter, and M. Popović, "Image classification for a time-domain microwave radar system: Experiments with stable modular breast phantoms," in *9th Euro. Conf. Antennas Propag. (EuCAP)*, Apr. 2015, pp. 1–5.

[31] J. Moll, D. Wõrtge, V. Krozer, A. Santorelli, M. Popović, B. Bazrafshan, F. Hübner, T. J. Vogl, and N. Nikolova, "Quality control of carbon-rubber tissue phantoms: Comparative MRI, CT, X-ray and UWB microwave measurements," in *11th European Conf. Antennas Propag. EuCAP*, Mar. 2017, pp. 2723–2727.

[32] D. Tajik, D. S. Shumakov, and N. K. Nikolova, "An experimental comparison between the Born and Rytov approximations in microwave tissue imaging," in *IEEE Int. Microw. Symp. (IMS)*, Jun. 2017.

[33] D. Tajik, D. S. Shumakov, A. S. Beaverstone, and N. K. Nikolova, "Quasi-real time reconstruction of the complex permittivity of tissue through microwave holography," *11th Eur. Conf. Antennas Propag. EuCAP*, pp. 3485–3488, Mar. 2017.

[34] D. Tajik, F. Foroutan, D. S. Shumakov, A. D. Pitcher, and N. K. Nikolova, "Real-time microwave imaging of a compressed breast phantom with planar scanning," *IEEE J. Electrom. RF Microw. Med. Bio.*, vol. 2, no. 3, pp. 154–162, Sep. 2018.

[35] G. P. Liney, D. J. Tozer, and L. W. Turnbull, "A simple and realistic tissue-equivalent breast phantom for MRI," *J. Magn. Resonance Imag.*, vol. 10, pp. 968–971, 1999.

[36] M. Freed, J. A. de Zwart, J. T. Loud, R. H. El Khouli, K. J. Myers, M. H. Greene, J. H. Duyn, and A. Badano, "An anthropomorphic phantom for quantitative evaluation of breast MRI," *Med. Phys.*, vol. 38, no. 2, pp. 743–753, 02 2011. [Online]. Available: https://www.ncbi.nlm.nih.gov/pubmed/21452712

[37] D. Tajik, A. D. Pitcher, and N. K. Nikolova, "Comparative study of the Rytov and Born approximations in quantitative microwave holography," *Prog. Electrom. Res. B*, Oct. 2017.

[38] D. S. Shumakov and N. K. Nikolova, "Fast quantitative microwave imaging with scattered-power maps," *IEEE Trans. Microw. Theo. Techn.*, vol. 66, no. 1, pp. 439–449, Jan. 2018.

[39] J. J. McCombe and N. K. Nikolova, "SNR assessment of microwave imaging systems," in *2014 IEEE Antennas Propag. Symp. (APSURSI)*, Jul. 2014, pp. 149–150.

[40] "MATLAB Signal Processing Toolbox," The MathWorks, Natick, MA, USA, 2014.

[41] N. K. Nikolova, “Matlab codes,” [Accessed Feb. 15, 2019]. [Online]. Available: http://www.ece.mcmaster.ca/faculty/nikolova/IntroMicrowaveImaging/MatlabCodes

[42] J. Trac, “Classifying the quality of point spread functions with contrast-to-noise ratios,” McMaster University, Tech. Rep., Aug. 2018. [Online]. Available: http://www.ece.mcmaster.ca/faculty/nikolova/IntroMicrowaveImaging/MatlabCodes/CNRevaluation/

[43] R. K. Amineh, A. Trehan, and N. K. Nikolova, “TEM horn antenna for ultra-wide band microwave breast imaging,” *Prog. Electrom. Res. B*, vol. 13, no. 13, pp. 59–74, Jan. 2009.

[44] R. K. Amineh, J. J. McCombe, A. Khalatpour, and N. K. Nikolova, “Microwave holography using point spread functions measured with calibration objects,” *IEEE Trans. Instrum. Meas.*, vol. 64, no. 2, pp. 403–417, Feb. 2015.

[45] D. Tajik, J. R. Thompson, A. S. Beaverstone, and N. K. Nikolova, “Real-time quantitative reconstruction based on microwave holography,” *IEEE Intern. Symp. Antennas Propag. (APS/URSI)*, pp. 851–852, Jun. 2016.

CHAPTER 4

REAL-TIME IMAGING WITH SIMULTANEOUS USE OF BORN AND RYTOV APPROXIMATIONS IN QUANTITATIVE MICROWAVE HOLOGRAPHY

Preface

This chapter is a reproduction of the following published article:

D. Tajik, R. Kazemivala, and N. K. Nikolova, “Real-time imaging with simultaneous use of Born and Rytov approximations in quantitative microwave holography,” in *IEEE Transactions on Microwave Theory and Techniques*, vol. 70, no. 3, pp. 1896–1909, Mar. 2022. doi: 10.1109/TMTT.2021.3131227.

This article is open access under the Creative Commons 4.0 licensing agreement.

I designed and performed the measurements both simulated and experimental, implemented the quantitative microwave holography (QMH) algorithm using the Born and Rytov combination in code, performed the image reconstruction, and wrote/edited the manuscript. Romina Kazemivala assisted in the development and testing of the combined Born/Rytov technique and reviewed the manuscript. Natalia K. Nikolova assisted in the development of the combined Born/Rytov technique and edited the manuscript.

4.1 Introduction

Microwave and millimeter-wave imaging methods have been extensively developed over the last half-century, with the more recent focus being on close-range imaging such as concealed weapon detection and security inspection, through-the-wall imaging, nondestructive testing, and biomedical imaging [1–11]. The advantages include good penetration through most optically opaque nonmetallic materials, nonionizing radiation, low equipment cost, and spatial resolution on the order of millimeters.

However, many of the objects of interest have significant heterogeneity with wavelength-size structural components, which lead to high propagation complexity and significant forward-model errors corrupting the image quality. Much work is still needed in the development of advanced algorithms and application-specific technologies, especially for near-field and real-time imaging.

The mathematical models of electromagnetic (EM) scattering are critically important for accurate image reconstruction. They utilize a variety of approximations in their kernels, i.e., the total electric field and/or Green's function, to reduce the computational complexity [9]. The *linear* models of EM scattering employ linearizing (weak-scattering) approximations of the inherently nonlinear kernel, leading to real-time reconstruction speeds. Yet, image fidelity may suffer, depending on the adequacy of the approximation for the given object under test (OUT). *Nonlinear* models, on the other hand, enable rigorous inverse-problem solutions through alternating computations of the dielectric profile of the target and the total internal field [10–13]. The computational effort is significant but the image fidelity and spatial resolution are often improved [14]. A common requirement in both the linear and nonlinear reconstruction methods is the input of the scattered-field responses, which are extracted from the measured total-field responses. Errors in this extraction are as detrimental to the image quality as measurement noise and uncertainties, or, errors in the total-field and Green's function distributions.

This has motivated significant research effort in comparing the Born and Rytov approximations as strategies for scattered data extraction [15–17]. To the authors' knowledge, all prior work implements both strategies separately and compares their performance. An alternative approach is offered in [18], where a unifying mathematical model is tuned through a single *ad hoc* parameter to operate as Born's approximation, Rytov's approximation or in-between the two. Neither of these approaches addresses the main problem in using Rytov's approximation with coherent measurements, namely, the possible failure in unwrapping the phase of the total-field responses across the acquisition aperture [15]. Note that phase unwrapping is a prerequisite for successful image reconstruction with Rytov's approximation. Such failure may occur when the OUT is strongly heterogeneous and/or the signal path through it exceeds several wavelengths. Strong coupling and multiple scattering between the antennas and the OUT in near-field imaging may also lead to phase-unwrapping failure. This failure is the likely reason why Rytov's data approximation remains largely unused in microwave and millimeter-wave imaging with coherent data.

Here, we propose a method to utilize Rytov's approximation of the OUT data by completely circumventing its phase unwrapping. At the same time, the method preserves the magnitude and phase information of the kernel of the scattering model; thus, it is still capable of reconstructing the OUT complex permittivity. Further, to make the best use of the complementarity in the advantages of the Born and Rytov approximations, we propose an inversion algorithm that uses both of them simultaneously. The proposed method also balances the limitations associated with each of these approximations, leading to the suppression of image artifacts. We show that the resulting image fidelity is equivalent to or better than those of the two separate algorithms (Born-based and Rytov-based). The proposed method is implemented in the framework of quantitative microwave holography (QMH), which has been developed recently for the purpose of real-time quantitative imaging [17]. QMH is particularly suitable for near-field measurement scenarios since the kernel of its scattering model can be derived from the measured system point-spread function (PSF) [19]. Note that the measured PSF, too, needs scattered-field response extraction.

We note that the proposed approach of combining Born's and Rytov's data approximations is in principle applicable to any image-reconstruction method where the scattered-field response is extracted from total-field measurements.

In [20], we have reported the first experimental verification of the benefits of using the Born and Rytov approximations in tandem. Higher quality images of a breast phantom with near-field measurements have been obtained while maintaining the real-time speed of the QMH reconstruction. Here, the theory underlying the combined Born-Rytov approximation approach is derived and the implementation in a straightforward QMH inversion algorithm is detailed. Common phase-wrapping errors are discussed that arise in the near-field imaging of complex structures. Examples based on simulated data highlight the situations where the Born and Rytov approximations have unique advantages over one another. The advantage of combining both in a single inversion algorithm is also demonstrated. An experimental example further demonstrates the benefits of utilizing both approximations in tandem.

4.2 Background: Quantitative Microwave Holography

A brief overview of QMH [9, 17, 21, 22] is provided below to aid understanding of the changes necessary to combine the Born and Rytov scattered-data extraction approaches. QMH is based on a linearized model of scattering, but utilizes the measurement of a scattering probe to produce a system-specific data point-spread function (PSF). The measured PSF is used in the inversion process to accurately account for the field distributions in the imaged volume, providing an advantage over simulation-based or analytical approximations, especially in near-field imaging. It also enables the reconstruction of *quantitative* images, which depict estimates of the permittivity and conductivity of the imaged object. This is a significant advantage over previous linear-reconstruction methods, which only produce *qualitatitve* images of the target reflectivity.

4.2.1 Measurement Setup

Holographic reconstruction (QMH included) can be applied on data collected over planar, cylindrical or spherical surfaces [23]. Here, all examples are based on a planar scanning arrangement (along x and y), which is illustrated in Fig. 4.1. The acquisition planes are on both sides of the imaged object allowing for reflection and/or transmission measurements.

Two preliminary measurements are necessary before the imaging of OUTs. The first measurement is that of the reference object (RO) illustrated in Fig. 4.1a. The RO is composed of the background medium along with the antennas and the components

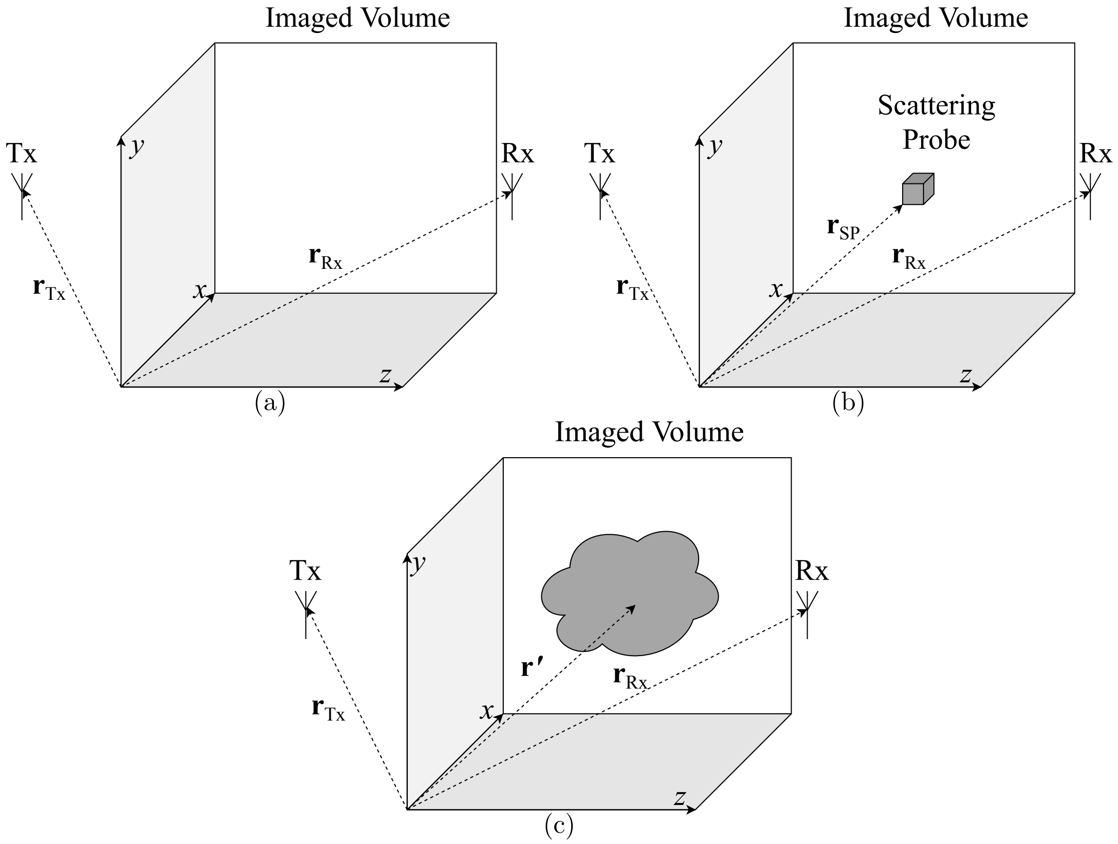

Figure 4.1: Illustration of the setup for measuring: (a) the reference object (RO), (b) the calibration object (CO), and (c) the object under test (OUT). The RO captures the incident-field portions of the measured responses, which depend on the antennas as well as the impact of the environment. The position vectors of the transmitting (Tx) and receiving (Rx) antennas are denoted as $\mathbf{r}_{\text{Tx}}$ and $\mathbf{r}_{\text{Rx}}$, respectively. The CO contains a small scattering probe (SP) at $\mathbf{r}'_{\text{sp}}$ of known size and permittivity, the measurement of which produces the data PSF. A position within the OUT is denoted by $\mathbf{r}'$.

of the positioning mechanism. It provides the incident-field responses, which are needed in the extraction of the scattered-field responses. Note that the background medium is not necessarily air. For example, in the case of breast-cancer imaging, the tissue can be embedded in a dielectric medium designed to reduce reflections at the interface between the tissue and the background [22].

The second measurement is that of the calibration object (CO); see Figure 4.1b. The CO is identical to the RO with the exception of an electrically-small scattering probe (SP) embedded in the center of the background medium. This measurement provides the data PSF, which enables quantitative image reconstruction.

The selection of the size and permittivity of the SP requires careful consideration, as it impacts the quantitative accuracy of the reconstruction [19, 24]. The SP size should be less than $\lambda_{\text{min}}/4$, where λ_{min} is the shortest wavelength. This allows for the assumption that the electric field within the probe is uniform, simplifying the forward model. Yet, the probe cannot be too small since this results in very weak scattering and poor signal-to-noise ratio (SNR) of the acquired PSFs. The best quantitative result is achieved if the permittivity of the probe satisfies [19]:

$$\epsilon_{\text{sp}}(\omega) \approx \epsilon(\mathbf{r}'; \omega) \,, \tag{4.1}$$

or

$$|\epsilon(\mathbf{r}'; \omega)| \,, |\epsilon_{\text{sp}}(\omega)| \ll |\epsilon_{\text{b}}(\omega)| \,. \tag{4.2}$$

Here, $\epsilon(\mathbf{r}'; \omega)$ is the permittivity of the OUT at the location $\mathbf{r}' = (x', y', z')$ within the imaged volume V' and at the angular frequency ω, $\epsilon_{\text{sp}}(\omega)$ is the permittivity of the scattering probe, and $\epsilon_{\text{b}}(\omega)$ is the permittivity of the background medium. As per (4.1), the probe's permittivity should be selected to be close to that of the OUT. In the case of highly heterogeneous OUTs, the SP is selected to match particular structures of interest embedded within. For example, in breast-cancer imaging, ϵ_{sp} is selected to match closely the permittivity of cancerous tissue [17, 22, 25]. The alternative suggested by (4.2) requires a background permittivity that is significantly higher than that of the OUT or the SP. This is not practical in real-time image reconstruction since a large contrast between the OUT and the background leads to multiple scattering effects, which are not accounted for in the linearized scattering models. Furthermore, depending on the imaged target, it may prove challenging to find a material with sufficiently higher permittivity.

4.2.2 Forward Model of Scattering

For brevity, only a short description of the forward model of scattering employed by the QMH method is shown here. More detailed derivations are available in [9,17]. The QMH forward model was original cast in terms of the scattered electric field, and is derived from the vector Helmholtz equation [26,27]. However, electric-field responses do not directly translate into measured responses such as S-parameters. Beaverstone *et al.* derived the exact forward model of scattering in terms of S-parameters as [28]:

$$S_{jk}^{\mathrm{sc}}(\mathbf{r}_{\mathrm{Rx}}, \mathbf{r}_{\mathrm{Tx}}; \omega) = \frac{j\omega\epsilon_0}{2\alpha_j\alpha_k} \cdot \iiint\limits_{V'} \Delta\epsilon_{\mathrm{r}}(\mathbf{r}')\mathbf{E}_j^{\mathrm{inc}}(\mathbf{r}_{\mathrm{Rx}}; \mathbf{r}'; \omega) \cdot \mathbf{E}_k^{\mathrm{tot}}(\mathbf{r}_{\mathrm{Tx}}; \mathbf{r}'; \omega) d\mathbf{r}' \,, \tag{4.3}$$

where S_{jk}^{sc} is the scattered portion of the S-parameter measured with the OUT, wherein the receiving (Rx) antenna j is positioned at $\mathbf{r}_{\mathrm{Rx}} = (x_{\mathrm{Rx}}, y_{\mathrm{Rx}}, z_{\mathrm{Rx}})$, the transmitting (Tx) antenna k is at $\mathbf{r}_{\mathrm{Tx}} = (x_{\mathrm{Tx}}, y_{\mathrm{Tx}}, z_{\mathrm{Tx}})$, and ω is the angular frequency.

Also, ϵ_0 is the permittivity of free space, α_ξ, $\xi = j, k$, are the root-power waves exciting the respective ports, $\Delta\epsilon_{\mathrm{r}}(\mathbf{r}')$ is the permittivity contrast within the OUT at position $\mathbf{r}' = (x', y', z')$, $\mathbf{E}_j^{\mathrm{inc}}$ is the incident field due to the Rx antenna if it were to operate in a transmitting mode excited by α_j, and $\mathbf{E}_k^{\mathrm{tot}}$ is the total internal field due to the Tx antenna.

The approximation of the total internal field as being the same as the respective incident field, $\mathbf{E}_k^{\mathrm{tot}} \approx \mathbf{E}_k^{\mathrm{inc}}$,[1] leads to the *linearized* S-parameter model of scattering in terms of the data PSF [9, 17, 20]:

$$S_{jk}^{\mathrm{sc}}(\mathbf{r}_{\mathrm{Rx}}, \mathbf{r}_{\mathrm{Tx}}; \omega) \approx \frac{1}{\Delta\epsilon_{\mathrm{r,sp}}\Omega_{\mathrm{sp}}} \cdot \iiint\limits_{V'} \Delta\epsilon_{\mathrm{r}}(\mathbf{r}') H_{jk}(\mathbf{r}_{\mathrm{Rx}}, \mathbf{r}_{\mathrm{Tx}}; \mathbf{r}'; \omega) d\mathbf{r}' \,, \tag{4.4}$$

where H_{jk} is the scattered-field response of the measurement system due to an electrically small (point-like) scatterer (the SP) of volume Ω_{sp} and contrast $\Delta\epsilon_{\mathrm{r,sp}} = \epsilon_{\mathrm{r,sp}} - \epsilon_{\mathrm{r,b}}$ at $\mathbf{r}'$. This is exactly the data PSF characterizing the particular measurement system. Mathematically, the data PSF represents the linearized resolvent kernel of (4.3) since

$$H_{jk}(\mathbf{r}_{\mathrm{Rx}}, \mathbf{r}_{\mathrm{Tx}}; \mathbf{r}'; \omega) \approx \frac{j\omega\epsilon_0}{2\alpha_j\alpha_k} \left[\Delta\epsilon_{\mathrm{r,sp}}\Omega_{\mathrm{sp}}\right]_{\mathbf{r}'} \mathbf{E}_j^{\mathrm{inc}}(\mathbf{r}_{\mathrm{Rx}}; \mathbf{r}'; \omega) \cdot \mathbf{E}_k^{\mathrm{inc}}(\mathbf{r}_{\mathrm{Tx}}; \mathbf{r}'; \omega) \,, \tag{4.5}$$

where the subscript $\mathbf{r}'$ of the term in the square brackets emphasizes the position of the SP. Thus, the linearized scattering model in (4.4) is in essence the first-order Born approximation of the scattered-field S-parameter response.

The model in (4.4) implies that the PSF H_{jk} is needed for a probe at all positions $\mathbf{r}'$ in the imaged volume. However, in a laterally uniform (layered) isotropic medium,

---

[1] This is commonly referred to as Born's zero-order approximation of the total internal field. This also occurs in Rytov's zero-order approximation.

the PSF can be assumed translationally invariant in (x, y) and (4.4) is written as

$$S^{\text{sc}}_{jk}(\mathbf{r}^{\text{Rx}}_{xy}, z_{\text{Rx}}; \mathbf{r}^{\text{Tx}}_{xy}; z_{\text{Tx}}; \omega) \approx \iiint\limits_{V'} \rho(\mathbf{r}')\cdot$$
$$H_{jk}(\mathbf{r}^{\text{Rx}}_{xy} - \mathbf{r}'_{xy}, z_{\text{Rx}}; \mathbf{r}^{\text{Tx}}_{xy} - \mathbf{r}'_{xy}, z_{\text{Tx}}; z'; \omega) dx'dy'dz' \,. \quad (4.6)$$

Here, $\mathbf{r}^{\text{Rx}}_{xy} \equiv (x_{\text{Rx}}, y_{\text{Rx}})$, $\mathbf{r}^{\text{Tx}}_{xy} \equiv (x_{\text{Tx}}, y_{\text{Tx}})$, $\mathbf{r}'_{xy} \equiv (x', y')$, and

$$\rho(\mathbf{r}') = \frac{\Delta\epsilon(\mathbf{r}')}{\Delta\epsilon_{\text{r,sp}}\Omega_{\text{sp}}} \quad (4.7)$$

is the complex *reflectivity function* to be reconstructed. The PSF H_{jk} is acquired with the SP at the center of the $z' = \textit{const}$. plane, $\mathbf{r}'_{xy} = 0$. Since the scan is two-dimensional (along x and y with fixed z_{Rx} and z_{Tx}), coordinate translation cannot be employed along z unless the PSF dependence on the z distances (from the Tx and Rx antennas to the probe) is approximated analytically. Such approximation is limited to far-field behavior in a uniform background and is not considered here. Thus, in order to generate three-dimensional (3D) images, N_z PSFs are needed, where the SP is always centered laterally ($\mathbf{r}'_{xy} = 0$) but is shifted along z to each desired range slice. This requires N_z CO measurements with the SP at $(0, 0, z_n)$, $n = 1, \ldots, N_z$.

4.2.3 Inversion with Quantitative Microwave Holography

Consider the application of the forward model (4.6) to the case of monostatic and/or bi-static scenarios, where the Rx and Tx antennas in each jk pair are in a fixed mutual position, i.e., $\mathbf{r}_{\text{Tx}}$ and $\mathbf{r}_{\text{Rx}}$ can be described by a single position vector $\mathbf{r}$ relative to the scanned OUT. For example, in a monostatic setup $\mathbf{r}_{\text{Tx}} = \mathbf{r}_{\text{Rx}} = \mathbf{r}$. In the bi-static setup in Fig. 4.1, the Rx and Tx antennas are aligned along boresight (z-axis) and scan on two opposing sides of the OUT, so that $\mathbf{r}_{\mathrm{Rx}} \equiv \mathbf{r}$ and $\mathbf{r}_{\mathrm{Tx}} = \mathbf{r} - \hat{\boldsymbol{z}}d$, where $\hat{\boldsymbol{z}}$ is the unit vector along z and d is the distance between the antennas. In this case, (4.6) is written as

$$S_{jk}^{\mathrm{sc}}(\mathbf{r}_{xy}, \bar{z}; \omega) \approx \iiint\limits_{V'} \rho(\mathbf{r}') \cdot H_{jk}(\mathbf{r}_{xy} - \mathbf{r}'_{xy}, \bar{z}; z'; \omega) dx' dy' dz' \,, \tag{4.8}$$

where $\mathbf{r}_{xy} \equiv (x, y)$ and $\bar{z} = const.$ define the plane scanned by the Rx antenna. We reiterate that the scan position $(\mathbf{r}_{xy}, \bar{z})$ also defines uniquely the position of the Tx antenna since the jk antenna pair is in a mutually fixed configuration during the scan. For simpler notations, hereafter, the subscript jk is replaced with a single subscript ξ ($\xi = 1, \ldots, N_{\mathrm{T}}$), indicating the *type* of response.

Since (4.8) is a convolution in x and y, it can be efficiently solved in the 2D Fourier space (k-space) where the convolution becomes multiplication. After discretization of the integral over z' into a sum, the k-space equations are given by

$$\widetilde{S}_{\xi}^{\mathrm{sc}}(\boldsymbol{\kappa}, \bar{z}; \omega_n) \approx \sum_{m=1}^{N_z} \tilde{\rho}(\boldsymbol{\kappa}, z'_m) \cdot \widetilde{H}_{\xi}(\boldsymbol{\kappa}, z'_m; \omega_n) \cdot \Omega_{\mathrm{v}} \,, \tag{4.9}$$

where *tilde* represents the Fourier transformed quantity, $\boldsymbol{\kappa} = (k_x, k_y)$ is the 2D Fourier variable, $\Omega_{\mathrm{v}} = \Delta x' \Delta y' \Delta z'$ is the volume of a voxel, ω_n, $n = 1, \ldots, N_\omega$, is the n-th frequency sample, and $m = 1, \ldots, N_z$ indicates the imaged slice along z. Note that $\bar{z}$ (the position of the observation plane) is omitted from the argument of $\widetilde{H}_{\xi}$ for brevity.

To solve for $\tilde{\rho}(\boldsymbol{\kappa}, z'_m)$, $m = 1, \ldots, N_z$, (4.9) is cast in the form of a linear system of equations at each point $\boldsymbol{\kappa}$ in Fourier space, where there are $N_{\mathrm{T}} N_\omega$ equations for the N_z unknown contrast values [17]. The systems solved at all points in Fourier space are small since N_T, N_ω and N_z are on the order of 1 to 10, 10 to 100 and 1 to 10, respectively. Thus, they are solved very quickly. The number of solved systems is $N_x \times N_y$, where N_x and N_y are the samples along x and y, respectively. With 2D FFT, the number of spatial samples equals that in k-space. The QMH inversion is fast and is typically completed within seconds even in problems where the number of voxels is on the order of 10^5. The computations are also amenable to parallel computing since each small system is solved independently.

Once $\tilde{\rho}(\boldsymbol{\kappa}, z'_m)$, $m = 1, \ldots, N_z$, is found, its real-space counterpart $\rho(x', y', z'_m)$ is recovered through 2D inverse FFT and the quantitative estimate of the complex permittivity contrast $\Delta\epsilon_\mathrm{r}(\mathbf{r}')$ is computed using (4.7). We emphasize that the quantitative output in QMH is achieved through the measured data PSF, since it is quantitatively accurate with respect to the permittivity contrast of a scatterer.

The computational complexity of QMH is comparable to that of well-established highly efficient k-space 3D image-reconstruction methods such as 3D synthetic aperture radar (SAR) range migration algorithm (RMA) [29–32] and closely related microwave holography [1,2,33–35]. At the same time, QMH has the added advantage of quantitative image output and the ability to handle equally well near-field and far-field measurements. The QMH computational complexity is dominated by: (i) the 2D FFT of the OUT data and the PSFs, $O(N_\mathrm{T}N_\omega(N_z+1) \cdot N_xN_y\log_2(N_xN_y))$, (ii) the solution of the k-space systems of equations, $O(N_xN_y \cdot N_\omega N_\mathrm{T}N_z^2)$ for a pseudo-inverse solver, and (iii) the 2D slice-by-slice inverse FFT of the reflectivity, $O(N_z \cdot N_xN_y\log_2(N_xN_y))$. On the other hand, microwave holography and the SAR RMA involve 2D FFT of the OUT data, too, with the same computational complexity as in QMH. To cast the 3D k-space reflectivity into real space, a 3D inverse FFT is needed with computational complexity of $O(N_xN_yN_z\log_2(N_xN_yN_z))$. Also, Stolt's mapping (also known as Stolt's interpolation) adds a computational complexity estimated as $O(N_iN_xN_y)$, where N_i depends on the chosen interpolator and the length of the interpolated sequence [36]. Note that Stolt's interpolation is not needed in QMH.

Another common real-time image-reconstruction method is the back-projection algorithm (BPA). In its original implementation, the BPA operates in real (x, y, z) space (see, e.g., [32]) and it has high computational complexity of $O(N_x^2N_y^2N_zN_\omega)$. However, fast BPAs have been proposed, which achieve reduced complexity of $O(N^{5/2})$, or even $O(N^2\log N)$, for a 2D reconstruction of size $N \times N$ [37]. Even the fast BPAs do not outperform the RMA and holography in terms of speed.

Finally, it is important to note that QMH is orders of magnitude faster than the traditional quantitative inverse-scattering methods, which employ iterative updates (e.g., nonlinear optimization) and simulation-based electromagnetic forward models. Such methods can potentially yield very accurate quantitative estimates with improved spatial resolutions but their computational complexity is prohibitive for real-time imaging due the use of full-wave simulators [9, 11].

4.3 Extracting Scattered Data

An important aspect of the scattering model is the approximation used to extract the scattered-field responses in the left-hand side of (4.4) from the measured total-field and incident-field responses. Two common approaches are deduced from the Born and Rytov first-order approximations [9, 15, 18, 26]. Under the first-order Born approximation of the external field, the total measured response is a superposition of the incident-field (or RO) response and the desired scattered-field response, which, in turn, is represented by the linearized scattering model in (4.4). In itself, (4.4) is a superposition integral, which neglects higher-order scattering effects such as mutual coupling and multiple scattering, leading to an effective representation of the imaged object as a collection of independent (or uncoupled) point scatterers.

The Rytov approximation, on the other hand, represents the total field as a complex phase correction on the incident field. Each approximation has distinct advantages and limitations that lead to unique image reconstructions when performed independently.

The QMH forward model (4.6) operates on the scattered-field responses that are extracted from the CO measurements with the scattering probe[2] and from the OUT measurements. The CO and RO (incident-field) measurements provide the input for the extraction of the data PSFs, i.e., $H_\xi \equiv S_\xi^{\mathrm{sc,CO}}$, whereas the OUT and RO measurements provide the input for the extraction of the OUT data S_ξ^{sc}.

It is worth noting that the data from monostatic reflection measurements are often assumed to be purely scattered-field responses, which is not true in practice; they do include object-independent effects such as the reflection at the antenna terminals and the reflections from the imaging-hardware components. Removing all RO signal components, measured in the absence of an OUT, is critical for maximizing the fidelity of the reconstruction.

---

[2] The selection of the SP for the CO determines the region of validity for which the forward model remains accurate. Ideally, the probe's permittivity is selected to match closely the permittivity of the target. In the case of highly heterogeneous targets, it should be close to the permittivity of structural components that are of particular interest, e.g., the cancerous tissues in breast-cancer screening. Details about the selection of the CO permittivity can be found in [19].

4.3.1 Born's Approximation

Born's first-order approximation of the external-field responses provides a simple method for extracting the scattered-field portion of the S-parameters from the measured incident-field and total-field responses:

$$S_{\xi}^{\mathrm{sc}}(\mathbf{r};\omega) \approx S_{\xi}^{\mathrm{tot}}(\mathbf{r};\omega) - S_{\xi}^{\mathrm{inc}}(\mathbf{r};\omega)\,, \tag{4.10}$$

where S_{ξ}^{inc} is the incident-field response from the RO measurement (see Fig. 4.1a) and S_{ξ}^{tot} is the total-field response from an object's measurement (see Fig. 4.1b and Fig. 4.1c). Note that the subtraction (4.10) is applied to the total-field responses of both the OUT, S_{ξ}^{tot}, and the CO, $S_{\xi}^{\mathrm{tot,CO}}$, to obtain the OUT data and the PSFs, respectively. As implied by Born's first-order approximation of the external field, the so extracted S_{ξ}^{sc} data are represented by the approximate (linearized) scattering model in (4.4) or (4.6).

The limitation of the first-order external-field Born approximation in the size and permittivity contrast of the scattering object must be kept in mind [9,15]:

$$2a|k(\mathbf{r}',\omega) - k_{\mathrm{b}}(\omega)|_{\max} < \pi\,, \tag{4.11}$$

where $k(\mathbf{r}',\omega)$ is the wavenumber inside the scatterer, k_{b} is the background wavenumber, and a is the radius of the smallest sphere circumscribing the scatterer. In the case of the scattering probe in the CO, k is constant in its volume. The limitation (4.11) is satisfied in the case of the CO as long as the probe is chosen properly; see Section 4.2.1. However, it may not always be satisfied by the OUT, which leads to image artifacts in regions where higher-order scattering effects exist due to mutual coupling and multiple scattering. Note that in near-field measurements such effects may exist not only within the OUT but also between the OUT and the antennas.

4.3.2 Rytov's Approximation

Rytov's first-order approximation represents the total-field response as a complex-phase correction on the incident-field response as [9]:

$$S_\xi^{\text{tot}}(\cdot) = S_\xi^{\text{inc}}(\cdot) \cdot \exp\left[S_\xi^{\text{sc}}(\cdot)/S_\xi^{\text{inc}}(\cdot)\right], \tag{4.12}$$

where the scattered-field response S_ξ^{sc} in the numerator of the complex phase is represented by the linearized scattering model (4.4). The expression is rearranged to express the extracted data S_ξ^{sc} in terms of the measured incident and total field responses [17]:

$$S_\xi^{\text{sc}}(\mathbf{r};\omega) \approx S_\xi^{\text{inc}}(\mathbf{r};\omega) \cdot \ln\left[\frac{S_\xi^{\text{tot}}(\mathbf{r};\omega)}{S_\xi^{\text{inc}}(\mathbf{r};\omega)}\right]. \tag{4.13}$$

Unlike Born's approximation, Rytov's approach is limited only by the permittivity contrast of the object, and not its size:[3]

$$|[k(\mathbf{r}') - k_\text{b}]/k_\text{b}| \ll 1\,. \tag{4.14}$$

However, Rytov's approximation is far more sensitive to errors arising when the left side of (4.14) exceeds several percent. Also, (4.13) is inherently prone to errors due

---

[3] Slaney [15] sums up the limitations of the two approximations in the data equation of scattering as: "... first-order Born approximation to be valid for objects where the product of the change in refractive index and the diameter is less than 0.35λ, and the first-order Rytov approximation for changes in the refractive index of less than a few percent, with essentially no constraint on the object size."

to phase wrapping [20]. Consider the breakdown of the logarithm in (4.13) into real and imaginary parts:

$$\ln\left[\frac{S_{\xi}^{\text{tot}}(\mathbf{r};\omega)}{S_{\xi}^{\text{inc}}(\mathbf{r};\omega)}\right] \approx \left\{\ln\frac{|S_{\xi}^{\text{tot}}(\mathbf{r};\omega)|}{|S_{\xi}^{\text{inc}}(\mathbf{r};\omega)|} + \mathrm{i}\left[\angle S_{\xi}^{\text{tot}}(\mathbf{r};\omega) - \angle S_{\xi}^{\text{inc}}(\mathbf{r};\omega)\right]\right\}. \tag{4.15}$$

Note that the imaginary part is a difference of phases, which are wrapped between $-\pi$ and π in measurements. Without unwrapping, this difference exhibits sharp discontinuities in the three-dimensional (3D) observation space (x, y, ω). The discontinuities in (x, y) adversely affect all inversion strategies that rely on Fourier transforms (FTs) which cast the data from the (x, y) space into the wavenumber space (k-space). Note that unwrapping along frequency ω does not ensure unwrapping in (x, y). Unwrapping the incident-field phase $\angle S_{\xi}^{\text{inc}}$ in (x, y) is usually successful since the background is laterally uniform. However, unwrapping $\angle S_{\xi}^{\text{tot}}$ is often problematic, since there is ambiguity whether a particular sharp transition in phase is due to reaching the π limit or if a true rapid phase transition has occurred. Consider Fig. 4.2a, which depicts the wrapped phase of an OUT measurement of a breast-tissue phantom at a particular frequency. A rapid phase change from $-\pi$ to π marks a portion of the left-side edge of the phantom, where the unwrapping is successful as seen in Fig. 4.2b. Meanwhile, other regions, including the phantom's interior, exhibit rapid phase transitions within the 2π limit as well as transitions from $-\pi$ to π, which may or may not be due to the actual properties of the object. This ambiguity is the fundamental reason for the unsatisfactory unwrapped phase distribution in Fig. 4.2b.

The applicability of the Rytov approximation (4.13) is conditional upon the successful phase unwrapping of the data in (x, y). Unfortunately, the unwrapping may

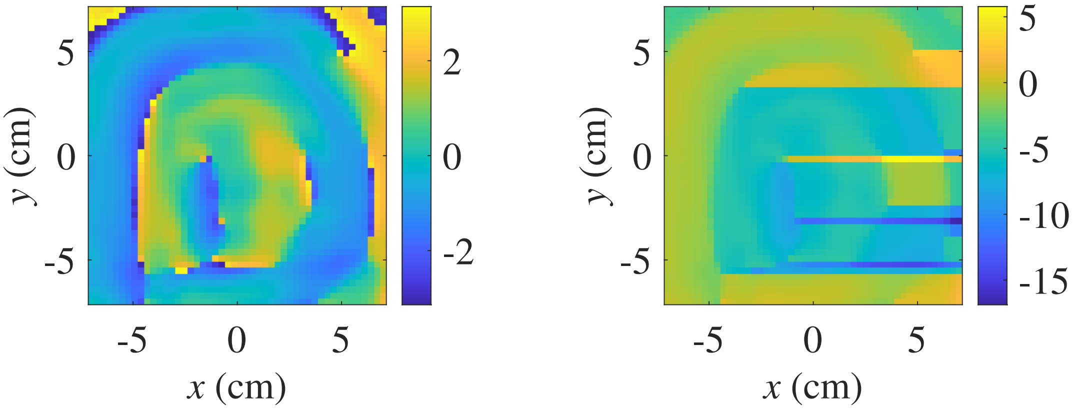

(a) (b)

Figure 4.2: Phase response (in radians) of a breast phantom measurement at 7.9 GHz: (a) phase wrapped, and (b) unsuccessful phase unwrapped response using Itoh's sequenced 1D unwrapping approach. The unwrapping is unable to adequately determine phase transition boundaries and leads to image artifacts in the form of streaking effects. Different unwrapping algorithms can yield different artifacts.

fail if significant property discontinuity exists within the OUT. This is the likely reason for the limited use of Rytov's approximation in microwave and millimeter-wave imaging with coherent data.

4.3.3 Comparing the Born and Rytov Data Approximations

Consider a cube of variable edge length and permittivity when it is placed in a background medium of $\epsilon_{\mathrm{r,b}} = 10 - \mathrm{i}2$ and is measured at 8 GHz.[4] Depending on the cube's size and permittivity, it may violate the limits of one or both of the approximations. Fig. 4.3a visualizes the limits of the Born and Rytov first-order approximations as calculated using (4.11) and (4.14) for this case. It is clear that the range of size and permittivity values where both approximations are of acceptable accuracy (area

---

[4] This background permittivity and frequency is selected due to its previous use in biomedical imaging for breast-cancer detection [22].

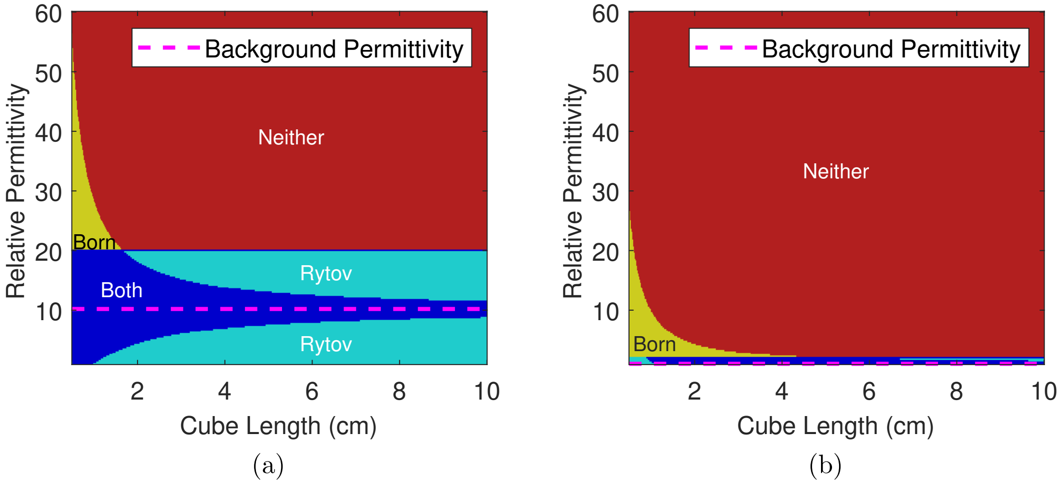

Figure 4.3: Maps of values identifying the regions where the Born and Rytov approximations valid or invalid for a cube of variable size and permittivity. The comparison is performed at 8 GHz in a background of: (a) $\epsilon_{\mathrm{r,b}} = 10 - \mathrm{i}2$, (b) $\epsilon_{\mathrm{r,b}} = 1 - \mathrm{i}0$ (vacuum). Four regions are identified by their color: (i) valid for both approximations (dark blue), (ii) valid only for Born's approximation (yellow), (iii) valid only for Rytov's approximation (light blue), and (iv) both the Born and Rytov limits are violated (red).

in dark blue) is limited. In this range, the two approximations yield images that are very similar to one another and the unwrapping of the phase of the OUT data for the Rytov approximation is usually successful. The complementarity of the two approximations is exemplified by the regions in yellow and light blue, where their simultaneous use can be beneficial. Another case is illustrated in Fig. 4.3b for a background of vacuum. In this case, the validity range of the Rytov approximation is extremely limited around the permittivity of vacuum, making it unsuitable for most dielectric targets.

The boundaries shown in Fig. 4.3 do not indicate strict cutoff for image reconstruction with the two linearizing approximations. The reconstruction degradation is gradual as the object's size and permittivity go beyond the limits. It manifests as

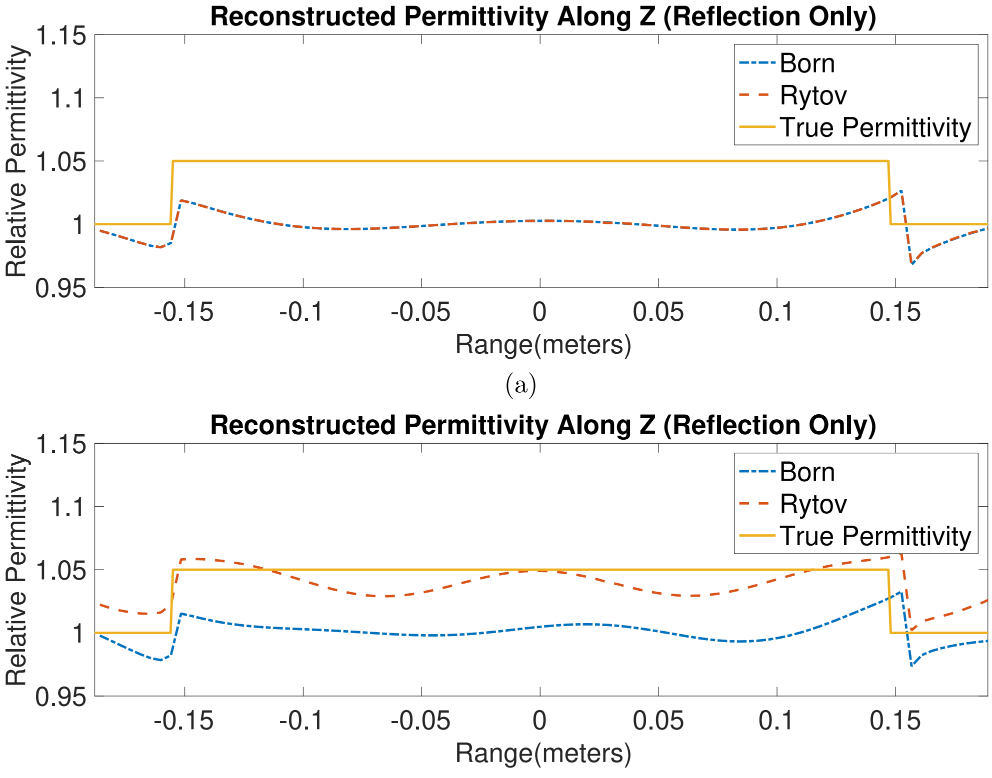

(a)

(b)

Figure 4.4: Holographic reconstruction of a large slab of relative permittivity $\epsilon_\mathrm{r} = 1.05$ in vacuum: (a) using only the reflected signals, (b) using both reflected and transmitted signals. In the reflection-only reconstruction, the Born and Rytov data approximations lead to almost identical permittivity profile. However, the Rytov-based reconstruction shows a marked improvement in the permittivity reconstruction of the slab interior when both reflection and transmission signals are used.

image artifacts in regions where the total internal field differs significantly from its incident counterpart. Degradation in the quantitative accuracy of the reconstruction occurs as well.

The differences between the Born and Rytov data approximations are illustrated with a simple one-dimensional (1D) reconstruction example, where the data is acquired via simulations with the time-domain software MEFiSTo [38]. A uniform plane wave is excited as a pulse, the spectrum of which is between 10 GHz and 25

GHz (at -3 dB level). The simulator is set to operate in a 2D TM$_z$ mode with the electric and magnetic field vectors being along z and y, respectively. The 1D plane-wave propagation along x is enforced by two parallel magnetic-wall boundaries running along x. The x-extent of the structure is 410 mm and it is terminated by absorbing boundary conditions at both ends. The excitation is at the left end of the computational domain. Two field probes in a vacuum background define ports 1 and 2, capturing reflection and transmission measurements, respectively. They are placed 20 mm away from the ends of the computational domain, i.e., they are 370 mm apart. They record the incident, scattering-probe, and OUT data in three separate simulations.

The scattering probe is a 2-mm thick dielectric slab of $\epsilon_{\mathrm{r,sp}} = 1.1$ placed midway between the field probes. The OUT is an electrically large dielectric slab of $\epsilon_{\mathrm{r1}} = 1.05$ and length of 300 mm. This length corresponds to approximately 10 and 25 wavelengths at 10 GHz and 25 GHz, respectively. At this length, Born's approximation is valid up to about 23 GHz whereas Rytov's approximation is marginally valid across the frequency band.

The time-domain responses are cast in the frequency (ω) domain and the reconstructions are performed using (4.9), where the scattered data are extracted with either the Born or the Rytov approximation. The results are shown in Fig. 4.4. The two reconstructions, when using only the reflected signal at port 1, are practically identical, and both of them fail to estimate the permittivity of the slab's interior; only its edges are detected. However, when the transmission responses are added to the reflected ones, the Rytov-based reconstruction exhibits improved accuracy compared to the Born-based one. This result is important. It indicates that the benefits of using

Rytov's data approximation are significant in transmission (forward-scattered) measurements. This result reinforces the extensive comparisons of the two approximations in diffraction tomography [15,18,39] and in transmission electron microscopy [40,41], which consider applications with transmission measurements only. In contrast, the majority of the microwave and millimeter-wave imaging radars employ reflection responses (e.g., [2,4,42]), where the benefits of Rytov's approximation are insignificant. Yet, in applications such as breast-cancer imaging and non-destructive testing, transmission data are common since they provide better data SNR [6,43–47]. Moreover, the background permittivity in these applications is often relatively high, which expands the applicability of Rytov's approximation as already discussed through Fig. 4.3a.

The mathematical reason for the almost identical reconstructions when using only the reflection coefficients (see Fig. 4.4a) is a scattered response, which is much weaker than the incident one. It is well-known that when the ratio of scattered-to-incident response is very small, the first-order Rytov approximation converges toward that of Born [9]. In this example, the incident response is collected by the field probe at port 1 in the absence of a scatterer and it is two orders of magnitude stronger than the scattered one. In practical reflection measurements, where the same antenna is used to transmit and receive, the incident response is the antenna reflection coefficient in the absence of a scatterer. With typical absolute values between 0.1 and 0.3 for a well-matched antenna, this response is still expected to exceed by orders of magnitude the change in the reflection coefficient due to a weak scatterer.

4.3.4 Tunable Born/Rytov Approximation

In [18], an approximation is proposed for optical diffraction tomography based on an analytical expression unifying the Born and Rytov approximations. The approximation in (4.13) is cast in a form that expresses the logarithmic term as a limit:

$$S_\xi^{\mathrm{sc}}(\mathbf{r};\omega) \approx S_\xi^{\mathrm{inc}}(\mathbf{r};\omega) \cdot \lim_{n\to\infty} n \left(\left[\frac{S_\xi^{\mathrm{tot}}(\mathbf{r};\omega)}{S_\xi^{\mathrm{inc}}(\mathbf{r};\omega)} \right]^{1/n} - 1 \right) . \tag{4.16}$$

Notice that with the setting of $n = 1$, (4.16) is identical to the Born approximation in (4.10). Thus, by selecting a value of $1 \leq n < \infty$ in the expression

$$S_\xi^{\mathrm{sc}}(\mathbf{r};\omega) \approx n \cdot S_\xi^{\mathrm{inc}}(\mathbf{r};\omega) \cdot \left(\left[\frac{S_\xi^{\mathrm{tot}}(\mathbf{r};\omega)}{S_\xi^{\mathrm{inc}}(\mathbf{r};\omega)} \right]^{1/n} - 1 \right) , \tag{4.17}$$

one can select the Born, the Rytov, or an in-between approximation. The study in [18] highlights the key difference between the case of $n = 1$ and that when n is very large: "the tendency appears to be that the Born approximation reproduces the boundary well but not the interior, while the Rytov fills the interior but removes the boundary". This conclusion motivates efforts to combine the two approximations by striking a balance between boundary and interior object reconstruction. Unfortunately, the use of (4.17) does not eliminate the need to unwrap $\angle S_\xi^{\mathrm{tot}}$ since the complex nth root still leads to a phase ambiguity of $2\pi/n$.

4.4 Combined Born/Rytov QMH Reconstruction

It has already been demonstrated that the two approximations produce somewhat different results in near-field experiments with QMH image reconstruction [17,20]. It was observed that the Born-based QMH recovers well small high-permittivity inclusions whereas Rytov-based QMH recovers high-loss inclusions better. This complementarity adds to the discussions in sections 4.3.3 and 4.3.4.

In this work, we propose a method of utilizing the Born and Rytov approximations in tandem in a single reconstruction step where unwrapping the total-field data is not necessary. To this end, we exploit the ability of the QMH reconstruction to "stack" equations of the form (4.9) into a linear system of equations at each point in k-space. This allows for incorporating the equations resulting from the two approximations in a common solution.

Further, to circumvent the problematic phase unwrapping in Rytov's approximation of the OUT data, only the real part of the logarithm term in (4.15) is used. To this end, the scattering model (4.8) is pre-multiplied as [20]:

$$\frac{\left|S_\xi^{\text{inc}}(\mathbf{r}_{xy},\bar{z};\omega)\right|}{S_\xi^{\text{inc}}(\mathbf{r}_{xy},\bar{z};\omega)}\cdot S_\xi^{\text{sc}}(\mathbf{r}_{xy},\bar{z};\omega)\approx \frac{\left|S_\xi^{\text{inc}}(\mathbf{r}_{xy},\bar{z};\omega)\right|}{S_\xi^{\text{inc}}(\mathbf{r}_{xy},\bar{z};\omega)}\iiint_{V'}\rho(\mathbf{r}')\cdot H_\xi(\mathbf{r}-\mathbf{r}'_{xy},\bar{z};z';\omega)dv'. \quad (4.18)$$

The substitution of S_ξ^{sc} in the left side of (4.18) with Rytov's approximation (4.13) results in a complex-valued expression, the real part of which is

$$S_{\xi,\text{Re}}^{\text{sc,RA}}(\cdot)=\left|S_\xi^{\text{inc}}(\cdot)\right|\cdot\ln\left[\frac{|S_\xi^{\text{tot,OUT}}(\cdot)|}{|S_\xi^{\text{inc}}(\cdot)|}\right]. \quad (4.19)$$

Here, $(\cdot)$ stands for $(\mathbf{r}_{xy}, \bar{z}; \omega)$. This represents the real part of the modified Rytov-approximated OUT data. Since the factor $|S_\xi^{\text{inc}}(\cdot)|/S_\xi^{\text{inc}}(\cdot)$ in (4.18) does not depend on $\mathbf{r}'$, it can be inserted in the integral in (4.18) and applied to the PSF $H_\xi(\cdot)$, resulting in the respective modified Rytov-based PSF:

$$H_\xi^{\text{RA}}(\mathbf{r}_{xy}, \bar{z}; z'; \omega) = \left|S_\xi^{\text{inc}}(\mathbf{r}_{xy}, \bar{z}; \omega)\right| \cdot \ln \left[\frac{S_\xi^{\text{tot,CO}}(\mathbf{r}_{xy}, \bar{z}; z'; \omega)}{S_\xi^{\text{inc}}(\mathbf{r}_{xy}, \bar{z}; \omega)} \right] . \tag{4.20}$$

Note that the PSF H_ξ^{RA} is complex and it requires the unwrapping of $\angle S_\xi^{\text{tot,CO}}$ in (x, y). However, the probe is a weak scatterer that imparts minimal phase shift, which is reasonably handled by any 2D phase-unwrapping algorithm [48–50].

Also, the multiplicative factor $|S_\xi^{\text{inc}}(\mathbf{r}; \omega)|$, which is present in the data and PSF terms on both sides of the scattering model, is not reduntant. It preserves the magnitude of the modified Rytov-approximated OUT scattered data, which is important in the subsequent integration of the Rytov-based and Born-based scattering equations.

In order to construct a system of equations containing both the Born model and the real part of the modified Rytov model (4.18)–(4.20), their complex-valued integral equations are broken into real and imaginary components:

$$\begin{aligned} S_{\xi,\text{Re}}^{\text{sc,BA,RA}}(\mathbf{r}_{xy}, \bar{z}; \omega) \approx \iiint\limits_{V'} & \rho_{\text{Re}}(\mathbf{r}') \cdot H_{\xi,\text{Re}}^{\text{BA,RA}}(\mathbf{r}_{xy} - \mathbf{r}'_{xy}, \bar{z}; z'; \omega) \\ & - \rho_{\text{Im}}(\mathbf{r}') \cdot H_{\xi,\text{Im}}^{\text{BA,RA}}(\mathbf{r}_{xy} - \mathbf{r}'_{xy}, \bar{z}; z'; \omega) dx'dy'dz', \end{aligned} \tag{4.21}$$

$$S^{\text{sc,BA}}_{\xi,\text{Im}}(\mathbf{r}_{xy},\bar{z};\omega) \approx \iiint\limits_{V'} \rho_{\text{Re}}(\mathbf{r}') \cdot H^{\text{BA}}_{\xi,\text{Im}}(\mathbf{r}_{xy}-\mathbf{r}'_{xy},\bar{z};z';\omega) + \rho_{\text{Im}}(\mathbf{r}') \cdot H^{\text{BA}}_{\xi,\text{Re}}(\mathbf{r}_{xy}-\mathbf{r}'_{xy},\bar{z};z';\omega)dx'dy'dz'. \quad (4.22)$$

Here, the subscripts Re and Im denote the respective components of a complex quantity whereas the superscripts BA and RA indicate the data approximation.

Similar to the QMH procedure in section 4.2.3, a 2D FFT is applied to all three real-valued datasets ($S^{\text{sc,BA}}_{\xi,\text{Re}}$, $S^{\text{sc,BA}}_{\xi,\text{Im}}$, $S^{\text{sc,RA}}_{\xi,\text{Re}}$) and the four real-valued PSFs ($H^{\text{BA}}_{\xi,\text{Re}}$, $H^{\text{BA}}_{\xi,\text{Im}}$, $H^{\text{RA}}_{\xi,\text{Re}}$, $H^{\text{RA}}_{\xi,\text{Im}}$). This allows for casting (4.21) and (4.22) into the k-space equations:

$$\widetilde{S}^{\text{sc,BA,RA}}_{\xi,\text{Re}}(\boldsymbol{\kappa};\omega_n) \approx \Omega_{\text{v}} \cdot \sum_{m}^{N_z} \tilde{\rho}_{\text{Re}}(\boldsymbol{\kappa},z'_m) \cdot \widetilde{H}^{\text{BA,RA}}_{\xi,\text{Re}}(\boldsymbol{\kappa},z'_m;\omega_n) - \tilde{\rho}_{\text{Im}}(\boldsymbol{\kappa},z'_m) \cdot \widetilde{H}^{\text{BA,RA}}_{\xi,\text{Im}}(\boldsymbol{\kappa},z'_m;\omega_n)\,, \quad (4.23)$$

$$\widetilde{S}^{\text{sc,BA}}_{\xi,\text{Im}}(\boldsymbol{\kappa};\omega_n) \approx \Omega_{\text{v}} \cdot \sum_{m}^{N_z} \tilde{\rho}_{\text{Re}}(\boldsymbol{\kappa},z'_m) \cdot \widetilde{H}^{\text{BA}}_{\xi,0,\text{Im}}(\boldsymbol{\kappa},z'_m;\omega_n) + \tilde{\rho}_{\text{Im}}(\boldsymbol{\kappa},z'_m) \cdot \widetilde{H}^{\text{BA}}_{\xi,0,\text{Re}}(\boldsymbol{\kappa},z'_m;\omega_n)\,. \quad (4.24)$$

Here, $\widetilde{S}^{\text{sc,BA}}_{\xi,\text{Re}}(\boldsymbol{\kappa};\omega_n)$ and $\widetilde{S}^{\text{sc,BA}}_{\xi,\text{Im}}(\boldsymbol{\kappa};\omega_n)$ are the 2D FTs of the real and imaginary parts of the Born-approximated OUT data $S^{\text{sc,BA}}_{\xi}(\mathbf{r}_{xy},\bar{z};\omega_n)$, respectively. For brevity, the position of the acquisition plane $\bar{z}$ has been omitted in the argument of the Fourier-transformed data. Analogously, $\widetilde{H}^{\text{BA}}_{\xi,\text{Re}}(\boldsymbol{\kappa},z'_m;\omega_n)$ and $\widetilde{H}^{\text{BA}}_{\xi,\text{Im}}(\boldsymbol{\kappa},z'_m;\omega_n)$ are the 2D FTs of the real and imaginary parts of the PSF $H^{\text{BA}}_{\xi}(\mathbf{r}_{xy},\bar{z};z';\omega_n)$. The FTs of the real and imaginary parts of $\rho(\mathbf{r}'_{xy},z'_m)$ are denoted by $\tilde{\rho}_{\text{Re}}(\boldsymbol{\kappa},z'_m)$ and $\tilde{\rho}_{\text{Im}}(\boldsymbol{\kappa},z'_m)$, respectively.

In order to solve for the reflectivity function, a system of equations is now constructed:

$$\mathbf{A}(\boldsymbol{\kappa})\widetilde{\boldsymbol{\rho}}(\boldsymbol{\kappa}) = \mathbf{b}(\boldsymbol{\kappa}), \tag{4.25}$$

where the system matrix takes the form

$$\mathbf{A}(\boldsymbol{\kappa}) = \left[\mathbf{A}_1(\boldsymbol{\kappa}) \cdots \mathbf{A}_{N_\mathrm{T}}(\boldsymbol{\kappa})\right]^T \ , \tag{4.26}$$

$$\mathbf{A}_\xi(\boldsymbol{\kappa}) = \begin{bmatrix} \mathbf{A}_\xi^{\mathrm{BA,Re}}(\boldsymbol{\kappa}) & -\mathbf{A}_\xi^{\mathrm{BA,Im}}(\boldsymbol{\kappa}) \\ \mathbf{A}_\xi^{\mathrm{BA,Im}}(\boldsymbol{\kappa}) & \mathbf{A}_\xi^{\mathrm{BA,Re}}(\boldsymbol{\kappa}) \\ \mathbf{A}_\xi^{\mathrm{RA,Re}}(\boldsymbol{\kappa}) & -\mathbf{A}_\xi^{\mathrm{RA,Im}}(\boldsymbol{\kappa}) \end{bmatrix}, \xi = 1, \ldots, N_\mathrm{T}\,, \tag{4.27}$$

$$\mathbf{A}_\xi^{\mathrm{a,b}}(\boldsymbol{\kappa}) = \begin{bmatrix} \widetilde{H}_{\xi,0}^{\mathrm{a,b}}(\boldsymbol{\kappa}, z_1', \omega_1) & \cdots & \widetilde{H}_{\xi,0}^{\mathrm{a,b}}(\boldsymbol{\kappa}, z_{N_z}', \omega_1) \\ \vdots & \ddots & \vdots \\ \widetilde{H}_{\xi,0}^{\mathrm{a,b}}(\boldsymbol{\kappa}, z_1', \omega_{N_\omega}) & \cdots & \widetilde{H}_{\xi,0}^{\mathrm{a,b}}(\boldsymbol{\kappa}, z_{N_z}', \omega_{N_\omega}) \end{bmatrix},$$

$$\mathrm{a} \equiv \mathrm{BA}, \mathrm{RA},\ \mathrm{b} \equiv \mathrm{Re}, \mathrm{Im}\,. \tag{4.28}$$

Accordingly, the data vector $\mathbf{b}$ is arranged as:

$$\mathbf{b}(\boldsymbol{\kappa}) = \left[\mathbf{b}_1(\boldsymbol{\kappa}) \cdots \mathbf{b}_{N_\mathrm{T}}(\boldsymbol{\kappa})\right]^T \ , \tag{4.29}$$

$$\mathbf{b}_\xi(\boldsymbol{\kappa}) = \left[\mathbf{b}_\xi^{\mathrm{BA,Re}}(\boldsymbol{\kappa}) \quad \mathbf{b}_\xi^{\mathrm{BA,Im}}(\boldsymbol{\kappa}) \quad \mathbf{b}_\xi^{\mathrm{RA,Re}}(\boldsymbol{\kappa}),\right]^T, \xi = 1, \ldots, N_\mathrm{T}\,, \tag{4.30}$$

$$\mathbf{b}_\xi^{\mathrm{a,b}}(\boldsymbol{\kappa}) = \left[\widetilde{S}_{\xi,\mathrm{b}}^{\mathrm{sc,a}}(\boldsymbol{\kappa}, \omega_1) \cdots \widetilde{S}_{\xi,\mathrm{b}}^{\mathrm{sc,a}}(\boldsymbol{\kappa}, \omega_{N_\omega})\right]^T, \mathrm{a} \equiv \mathrm{BA}, \mathrm{RA},\ \mathrm{b} \equiv \mathrm{Re}, \mathrm{Im}\,. \tag{4.31}$$

The system (4.25) is solved at each point $\boldsymbol{\kappa}$ in Fourier space using a least-squares solver[5] to obtain the solution vector $\tilde{\boldsymbol{\rho}}$:

$$\tilde{\boldsymbol{\rho}}(\boldsymbol{\kappa}) = \Omega_{\mathrm{v}} \cdot \left[\tilde{\rho}_{\mathrm{Re}}(\boldsymbol{\kappa}, z'_1) \cdots \tilde{\rho}_{\mathrm{Re}}(\boldsymbol{\kappa}, z'_{N_z}), \tilde{\rho}_{\mathrm{Im}}(\boldsymbol{\kappa}, z'_1) \cdots \tilde{\rho}_{\mathrm{Im}}(\boldsymbol{\kappa}, z'_{N_z})\right]^T . \tag{4.32}$$

From $\tilde{\boldsymbol{\rho}}(\boldsymbol{\kappa})$, the real and imaginary parts of the reflectivity function $\rho(x', y', z'_m)$, $m = 1, \ldots, N_z$, are recovered using 2D inverse Fourier transform, from which the complex permittivity is obtained via (4.7).

4.5 Validation Through Simulation

In order to demonstrate the effectiveness of the proposed reconstruction method, the measurement of an OUT composed of several objects is emulated through simulations in FEKO [52] (see Fig. 4.5). The objects are embedded in a uniform background medium with $\epsilon_{\mathrm{r,b}} = 10 - \mathrm{i}0$. The first object is a large prism of dimensions 4 cm by 4 cm by 3 cm and relative permittivity $\epsilon_{\mathrm{r}} = 25 - \mathrm{i}5$. The small cubes (1 cm on a side) are also present. Their relative permittivity is $\epsilon_{\mathrm{r}} = 40 - \mathrm{i}8$. One of these cubes is embedded in the large prism offset from the center, and the other resides in the background medium.

The measurement is performed by six half-wavelength (at each frequency) dipole antennas. Only the two dipoles residing on the z axis on both sides of the OUT transmit (one at a time) whereas all six antennas receive, leading to a total of 12 data sets. The antennas perform a raster scan along x and y at 5 mm increments across a 15 cm by 15 cm aperture. The frequency is swept from 3 GHz to 7 GHz in 1 GHz

---

[5] One example is the pseudoinverse function *pinv* provided by *MATLAB ver. R2020a* [51].

intervals. The selection of the frequency bandwidth and interval are based on the desired range resolution and the maximum range associated with the imaged volume (which, in turn, ensures no aliasing along frequency) [9]. The antennas are located either at $z = 60$ mm or $z = -60$ mm.

The data PSFs are acquired in three separate simulations with the same background and antenna arrangement as in the OUT simulation, where the scattering object is a cuboidal scattering probe of edge length 1 cm ($\epsilon_{\mathrm{r,sp}} = 40 - \mathrm{i}8$) at the center, $x' = y' = 0$, of each of three planes $z' = 50, 60, 70$ mm. These are the planes where the image slices are generated.

The 3D reconstructions of the complex permittivity using the Born, the modified Rytov, the Marks, and the proposed combined Born/Rytov QMH reconstructions are shown in Figs. 4.6 and 4.7. The Born-based and the modified Rytov-based reconstructions do not require the phase unwrapping of the OUT data along (x, y). We reiterate that the modified Rytov reconstruction, based on (4.21), employs only the absolute values of the OUT data whereas the respective PSFs are complex. Since the proposed combined Born/Rytov approach, too, utilizes (4.21), it does not require OUT data phase unwrapping either. Both, the modified-Rytov and the combined Born/Rytov reconstructions need the phase unwrapping of the CO responses in order to extract the complex Rytov-based PSFs. This phase unwrapping is performed with Itoh's method [48] and it is successful. On the other hand, the phase unwrapping of the OUT data is necessary for the reconstruction based on the Marks approximation. In this example, the OUT data unwrapping is successful.

The Born reconstruction (Figs. 4.6a and 4.6b) outlines well the structures of the large prism and the external small cube. It also correctly shows the increased

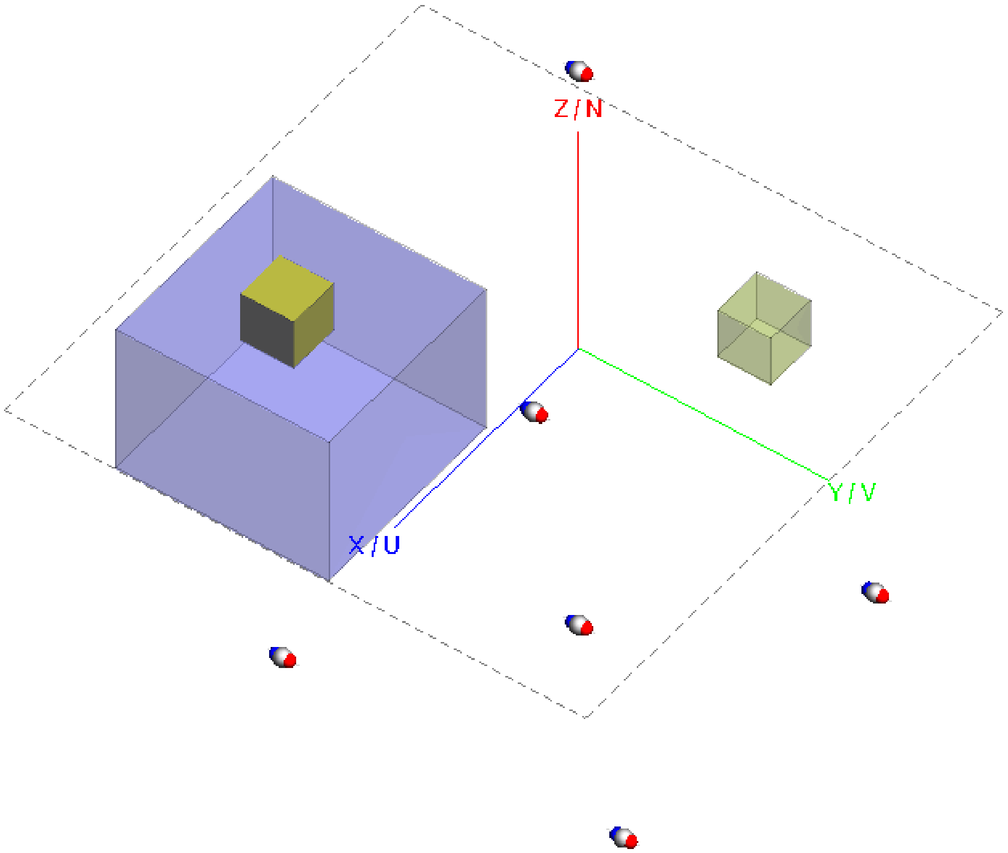

Figure 4.5: The simulation setup emulating the measurement of the OUT, which consists of three prisms: two cubes with edge lengths of 1 cm ($\epsilon_\mathrm{r} = 40 - \mathrm{i}8$) and a larger prism of size 4 cm by 4 cm by 3 cm ($\epsilon_\mathrm{r} = 25 - \mathrm{i}5$). The background permittivity is $\epsilon_\mathrm{r,b} = 10 - \mathrm{i}0$. All six dipole antennas receive but only the center two dipoles transmit (one at a time).

contrast of the external small cube relative to the larger prism. However, it fails to clearly identify the embedded cube within the prism at $z = 60$ mm, and to estimate its higher contrast relative to that of the large prism. The reconstruction also incorrectly reconstructs a very low permittivity in the $z = 60$ mm slice of the large prism.

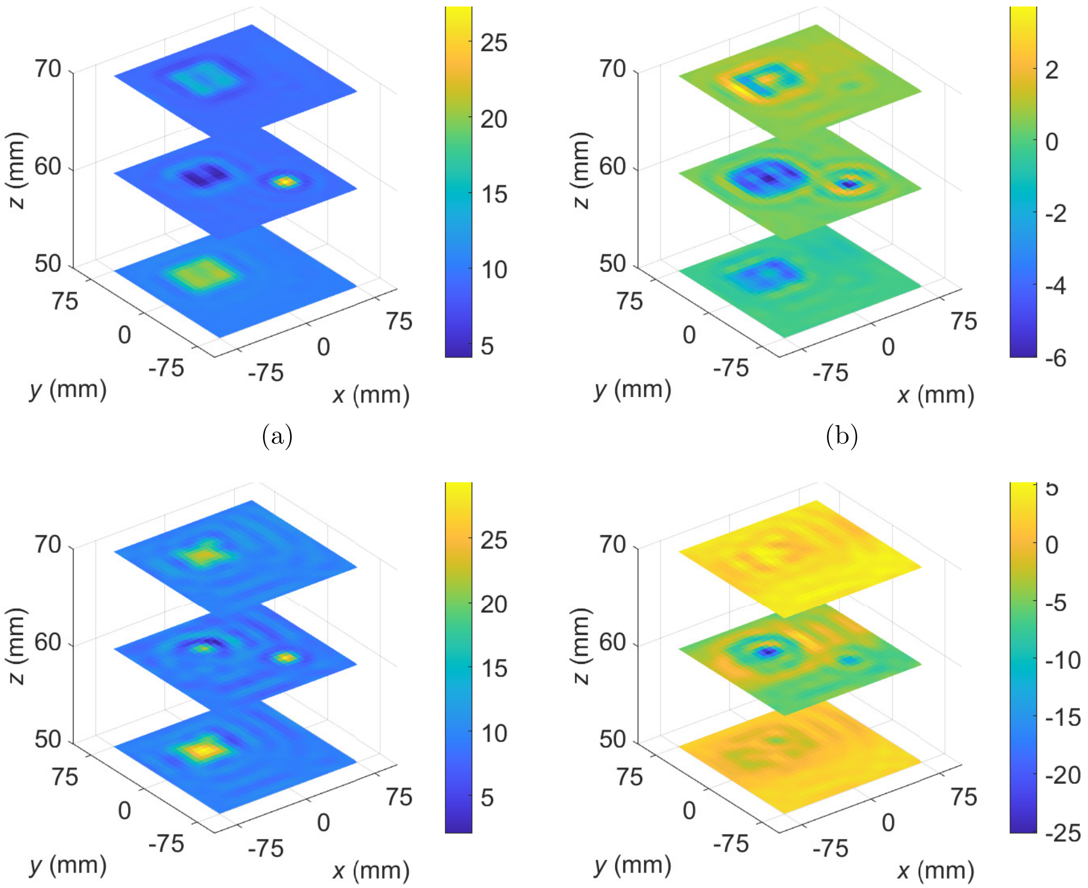

(a) (b)

(c) (d)

Figure 4.6: 3D reconstructed images of the simulated objects in terms of the real part (left) and the imaginary part (right) of the permittivity: (a,b) Born-based reconstruction, (c,d) modified Rytov-based reconstruction, (e,f) Marks' reconstruction ($n = 2$), and (g,h) proposed combined Born/Rytov reconstruction.

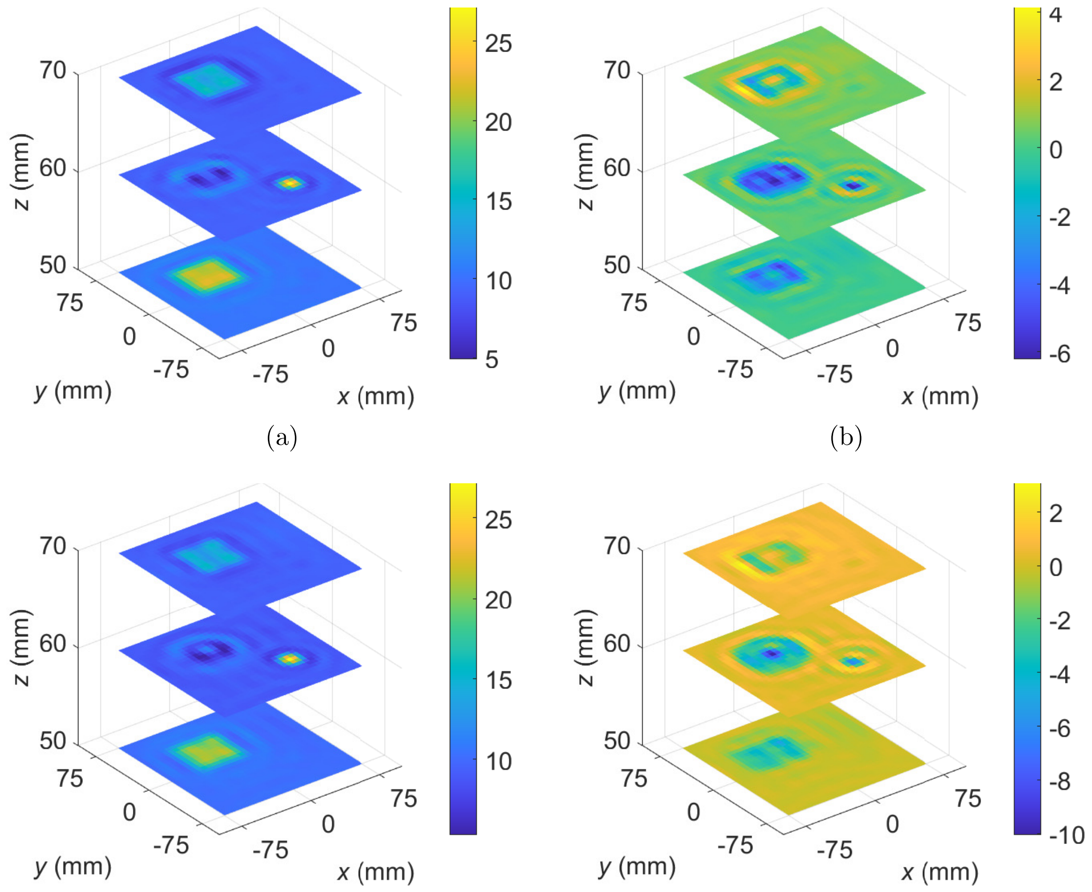

(a) (b)

(c) (d)

Figure 4.7: 3D reconstructed images of the simulated objects in terms of the real part (left) and the imaginary part (right) of the permittivity: (a,b) Marks' reconstruction ($n = 2$), and (c,d) proposed combined Born/Rytov reconstruction.

The modified Rytov approximation, on the other hand, produces less structurally accurate representations of the three objects, especially that of the large prism (see Fig. 4.6c and 4.6d). However, the presence of a strong scatterer in the large prism is apparent in the slice $z = 60$ mm. The small external cube is also reconstructed nearly identically to that of the Born-based reconstruction. Rippling artifacts are observed, which are often encountered in k-space reconstruction, especially when Rytov-based

Table 4.1: Root Mean Square Error of Real and Imaginary Relative Permittivity Reconstructed in the Simulation-based Example

Approximation	Real Part	Imaginary Part
Born-based QMH	3.7446	1.1994
Rytov-based QMH	3.2628	3.8154
Marks' QMH	3.4818	1.1477
Combined Born/Rytov QMH	3.5405	1.1829

data approximations are used. These are Gibbs' effects caused by sharp transitions either in real (x, y) or in Fourier (k_x, k_y) space [53].

The reconstruction using Marks' tunable approach (with $n = 2$) provides an in-between reconstruction between the two approximations, with slightly enhanced detection of the embedded cube at $z = 60$ mm (see Figs. 4.7a and 4.7b) Also, the small *ad hoc* value of n is low and the possibility of errors due to the $2\pi/n$ ambiguity is low.

The combined Born/Rytov approach produces an image that retains the structural accuracy of the Born approximation while also detecting the embedded cube in the larger prism (see Figs. 4.7c and 4.7d). The rippling artifacts are suppressed and the reconstruction is improved relative to the individual Born and modified-Rytov reconstructions.

The root-mean square error of the real and imaginary parts of the permittivity for each reconstruction is shown in Table 4.1. Note that while the Rytov approach has an overall lower error in the real part of the permittivity relative to the other methods, the error in the imaginary part is significantly larger than the other methods. On average, the Marks approach and the combined Born/Rytov approach show improvement versus using solely the Born or Rytov approximations. However, we must reiterate that the performance of Marks' approach is subject to the successful phase unwrapping of the OUT data whereas the proposed combined Born/Rytov approach does not require this phase-unwrapping step, which ensures wider and more robust applicability.

Note that all the image reconstructions generate some nonphysical values, particularly in the imaginary part of the permittivity. This effect can be expected when reconstructing images near the permittivity bounds ($\epsilon_{\mathrm{r}}' = 1$ and $\epsilon_{\mathrm{r}}'' = 0$), and are due to the Gibbs effects as well as the limitation of the employed linearized scattering model.

4.6 Validation Through Experiments

4.6.1 Measurement Setup

The example discussed here is based on the transmission S-parameter measurements used previously in [20, 25]. A compressed breast phantom is measured to evaluate the ability of QMH to detect breast-tumor simulants with planar-scan data. The phantom is constructed from five 1.1 cm carbon-rubber sheets, with permittivity values shown in Table 4.2; see also Fig. 4.8. These permittivity values are selected to match the average permittivity of BI-RADS Type 2 breast tissue, which has scattered fibroglandular content of less than 50% of the overall tissue mass [54]. Inside two of the five sheets, sections are hollowed out and cancerous tissue simulants (circled in blue in Figs. 4.8a and 4.8b) as well as fibroglandular tissue simulants (white structure in Fig. 4.8b) are inserted. The remaining space is filled with a matching medium whose permittivity (see Table 4.2) is close to that of the carbon-rubber sheets. It is

Table 4.2: Averaged Dielectric Properties of Phantom Materials from 3 GHz to 8 GHz [20]

Material (Structure)	ϵ'	ϵ''
Carbon-rubber Sheet (Averaged Breast Tissue)	10.91	2.84
Embedding/Matching Medium	10.41	5.07
Tumour Simulant	55.27	16.63
Fibroglandular Tissue Simulant	23.83	11.27
Scattering Probe (PSF)	50.00	0.05

important to remove the air pockets as they present high permittivity contrast that may lead to image artifacts. All five carbon-rubber sheets are stacked to form the completed phantom (see Fig. 4.8c), wherein Layers 2 and 4 contain the inclusions described above. Layers 1, 3, and 5 are homogeneous. Plastic wrap is used to secure the inclusions in Layers 2 and 4 as well as to hold together the phantom.

The acquisition is performed in an RF-shielded chamber (see Fig. 4.9a) with 1 TEM-horn transmitting antenna [55] and a 9-element receiving array of bowtie antennas [56] (see Fig. 4.9b). The antennas are designed to deliver maximum power when they are in direct contact with or are very close to (within 2 mm) the breast-tissue phantom. Of the 9 available bowtie antennas, only the 5 co-polarized antennas are used; the remaining are connected to 50Ω loads. This is because the data SNR of the cross-polarized signals is poor as determined through the quality control evaluation of the experimental setup [24]. The chamber contains a platform, which is moved laterally by stepper motors. In the current experiment, the spatial sampling step is 3 mm.

The phantom is placed in a *Plexiglas* tray and surrounded by an embedding medium, the permittivity of which is listed in Table 4.2; see also Fig. 4.9c. The

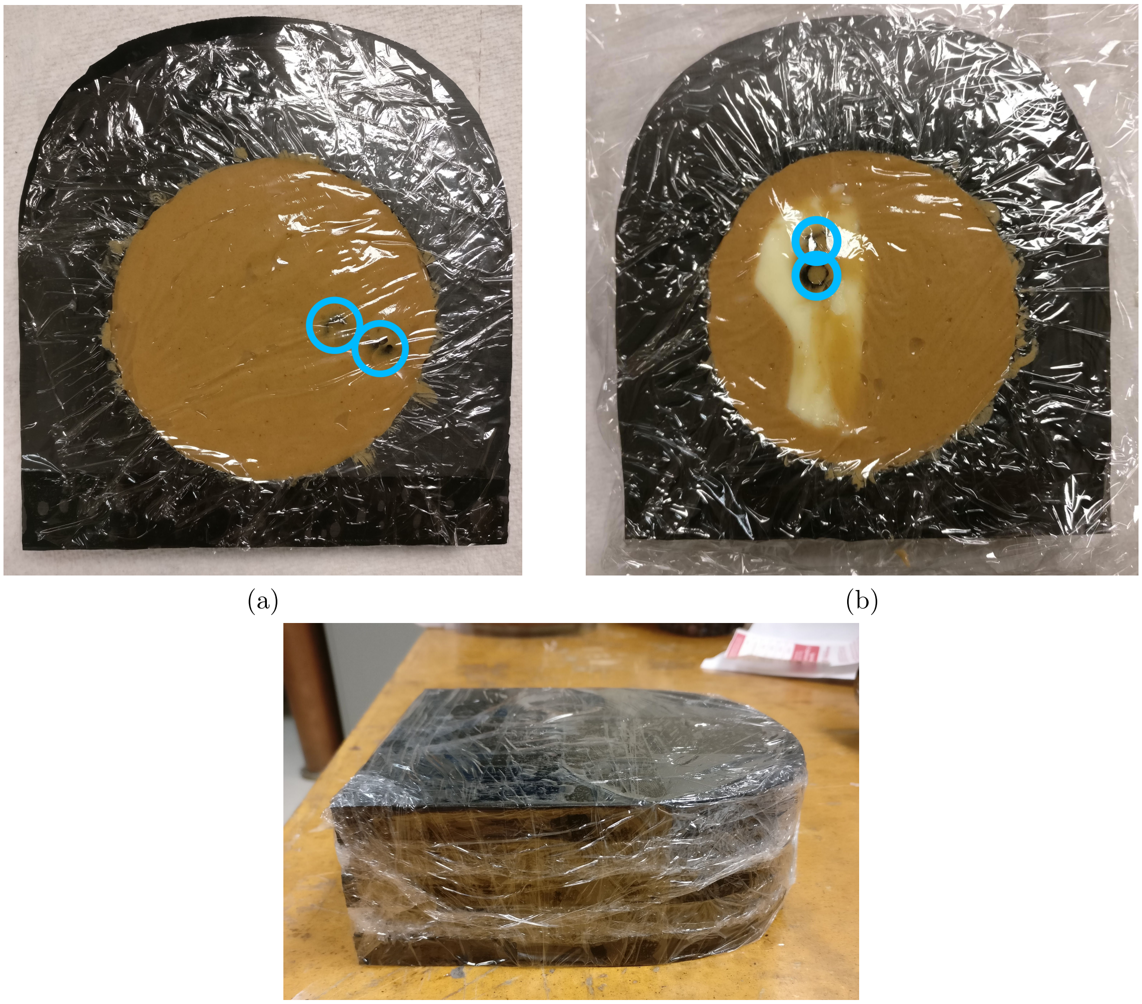

(a) (b)

(c)

Figure 4.8: Photos of the breast phantom: a) layer 2, containing two tumour simulants (circled in photo) in the embedding medium, b) layer 4, containing two tumour simulants (circled in photo) within the fibroglandular simulant (white color) in the embedding medium, and c) the assembled phantom. Photos taken from [25].

embedding medium is necessary to reduce reflections at the boundary of the phantom and reduce the image artifacts. To further reduce reflections at the *Plexiglas*/air interface, a 4 cm thick layer of microwave absorbing foam is placed around the side walls of the tray. This has been shown to significantly reduce artifacts produced by the tray itself [24]. The tray is covered with a *Plexiglas* lid (4 mm thick) and placed on the measurement platform.

An Advantest R3770 VNA paired with an Advantest R3970 RF switch performs a measurement at every sampled position from 3 GHz to 8 GHz in 100 MHz increments. Since the attenuation through the embedding medium is significant (at 8 GHz, it exceeds 65 dB), a power amplifier is used between the VNA and the TEM horn, supplying 39 dBm to the TEM horn antenna. Only transmission measurements are acquired across the bowtie antennas, since reflection measurements cannot be acquired because of the nonreciprocal amplification stage.

The measurement setup is calibrated through two RO (or background) measurements, and one CO (scattering probe) measurement. The CO measurement is constructed with five uncut circular carbon rubber sheets made of the same material as the sheets used to make the compressed phantom. A cylindrical SP of permittivity $\epsilon_{\mathrm{r,sp}} = 50 - \mathrm{i}0.05$ (made of microwave ceramics), and of diameter and height of 1 cm, is placed in the central sheet (Layer 3). Constructing the CO in this manner guarantees that the SP remains fixed in the desired central position during the movement of the platform.

Two RO measurements are performed to acquire S^{inc} for each of the CO and the OUT measurements. The first RO consists of the *Plexiglas* tray filled only with the matching medium. It is used to extract the scattered data from the breast-phantom

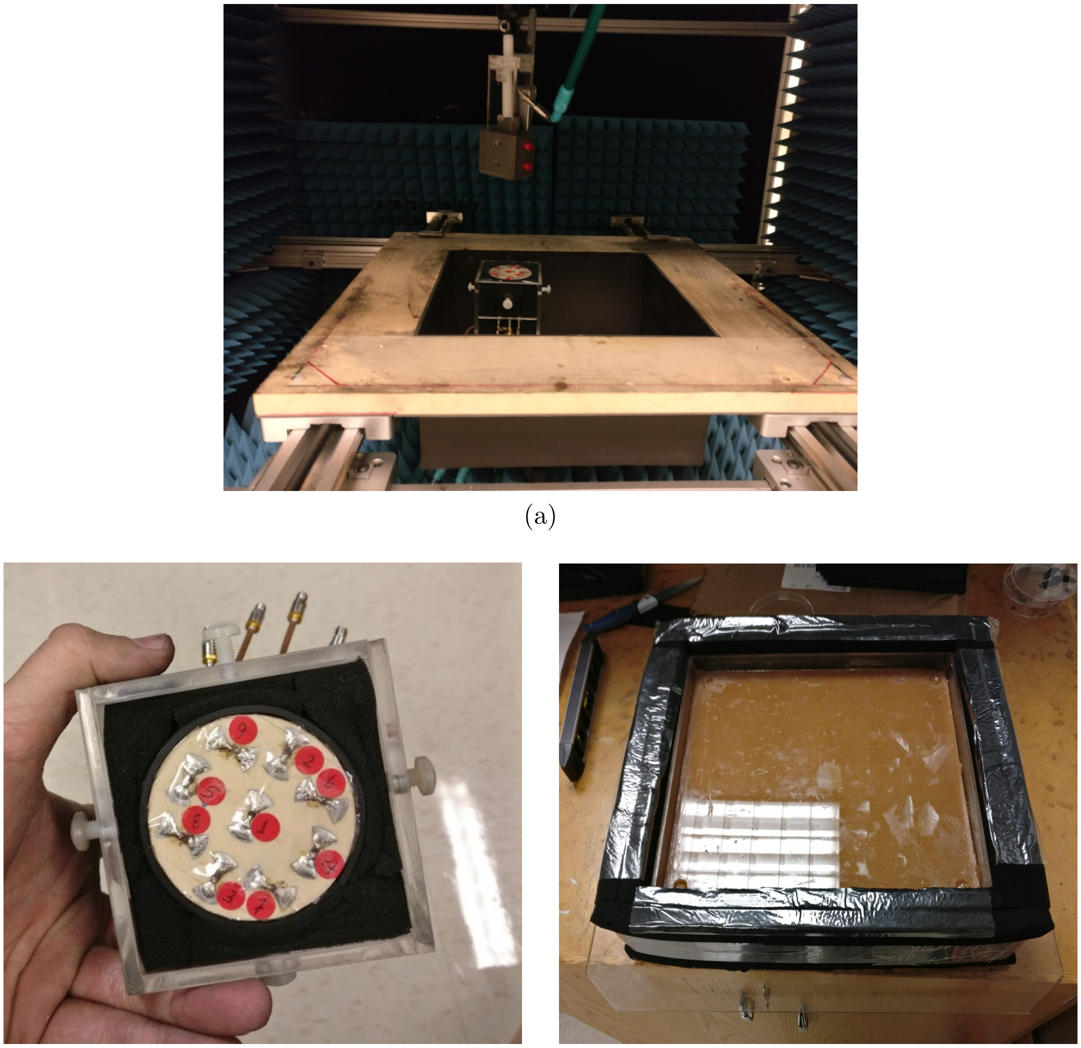

(a)

(b) (c)

Figure 4.9: Photos of the experimental setup: (a) the raster-scanning acquisition chamber containing the TEM horn (top) and the 9-element bowtie array (bottom), (b) a close-up image of the bowtie array and its fixture, and (c) the RO measurement comprised of an embedding medium, a tray enclosing it, and additional microwave absorbers reducing reflections at the *Plexiglas* walls and edges. Photo (c) taken from [24].

measurements. The second RO includes not only the tray but also the uncut carbon rubber sheets without the SP. It is used to extract the PSFs. Since the CO contains carbon rubber sheets that secure the probe in place, the highest PSF SNR is achieved with an RO that matches the CO arrangement (without the probe).

The OUT is comprised of the compressed breast phantom placed in the embedding medium in the tray.

4.6.2 Results

QMH reconstructions of the phantom using the Born, the modified Rytov, the Marks, and the proposed combined Born/Rytov approach are shown in Figs. 4.10 and 4.11. The phase unwrapping of the OUT data, which is necessary for the reconstruction based on the Marks approximation, fails at several frequencies as illustrated in Fig. 4.2. Nonetheless, the Marks de-embedding formula (4.17) is applied with $n = 2$ for comparison.

The 2D images in Figs. 4.10 and 4.11 are projections of the 3D complex-permittivity distribution of the phantom onto the $z' = 0$ plane. 3D imaging is not feasible with this setup since it provides transmission measurements only, where the receiving antennas are either aligned with the transmitting-antenna boresight or are only slightly off-boresight. This results in loss of range resolution [9, 57]. The range resolution can be improved by increasing the lateral (xy) distance between the transmitting and receiving antennas. Unfortunately, this increases the signal path and thus the attenuation, leading to poor data SNR. When operating in 2D mode, the QMH algorithm uses only one PSF, namely, the PSF corresponding to the position $z' = 0$ of the scattering probe. In this case, the system matrix in (4.28) has only one column, i.e., $N_z = 1$, and the k-space solution vector $\tilde{\boldsymbol{\rho}}(\boldsymbol{\kappa})$ in (4.32) has a single value at each $\boldsymbol{\kappa} \equiv (k_x, k_y)$. In effect, the permittivity values displayed in Figs. 4.10 and 4.11 are averaged over the thickness (5.5 cm) of the phantom. This is why the locations of the tumor simulants yield a relatively small permittivity increase over that of the carbon-rubber material.

We note that the 2D reconstructions in Figs. 4.10 and 4.11 demonstrate a marked improvement of the quantitative accuracy compared to the those reported in [20]. The improvement is due to a new k-space low-pass filtering strategy. Low-pass filtering is common in all methods performing the inversion in k-space in order to remove the high-frequency artifacts that are generated by the 2D FFT of the data; see [17] for the application of such filtering with QMH. Here, an energy-conserving low-pass filter is proposed. In [17], a 4th-order Butterworth low-pass filter with a maximum value of 1 is used. This setting reduces significantly the aggregate complex-permittivity image energy in k-space, resulting in underestimating the permittivity values in (x, y) space. To conserve the image energy, the filter's maximum value M is determined so that its overall energy equals that of the unity square filter, leading to the expression

$$M = \frac{N_x N_y}{\sum_{k_x} \sum_{k_y} \hat{B}(k_x, k_y)^2} \, . \tag{4.33}$$

Here, $\hat{B}(k_x, k_y)$ is the Butterworth filter of unity maximum and $B(k_x, k_y) = M \cdot \hat{B}(k_x, k_y)$ is its energy-conserving counterpart. The number of samples along k_x and k_y is N_x and N_y, respectively.

The Born reconstruction (see Fig. 4.10a) outlines the fibroglandular structure and the cancerous inclusions marginally well in the real part of the permittivity. The

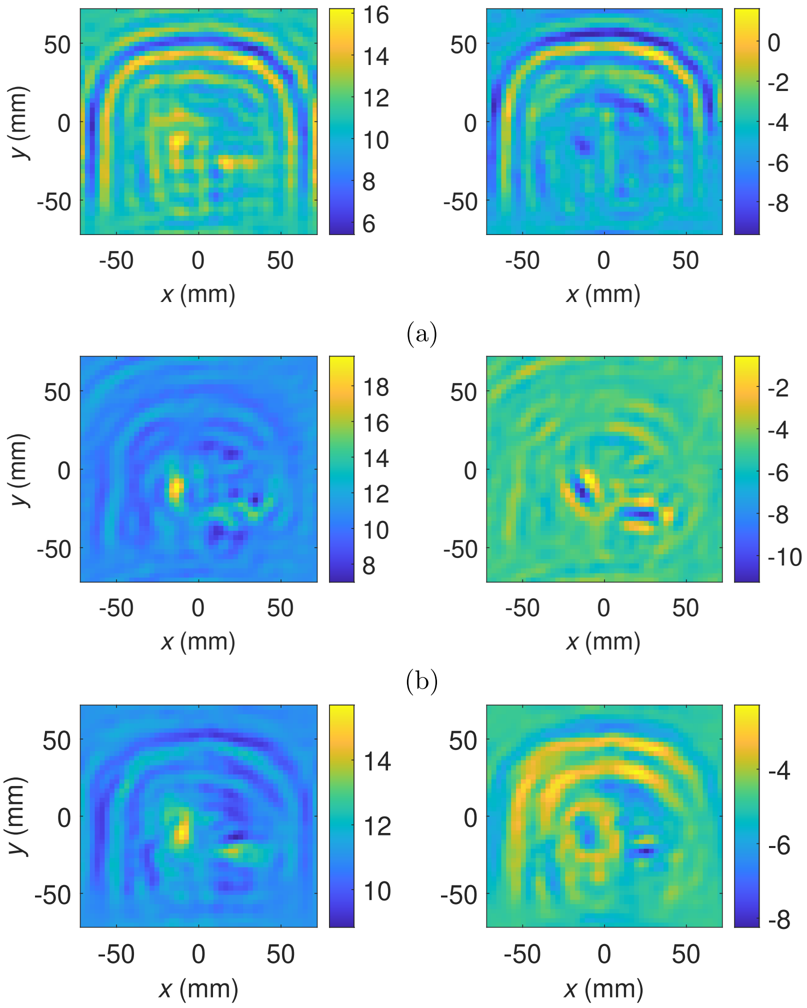

(a)

(b)

(c)

Figure 4.10: 2D QMH reconstructions of the real part (left) and the imaginary part (right) of the relative permittivity of the breast phantom: (a) Born-based reconstruction, (b) Rytov-based reconstruction, (c) Marks' hybrid approach. A k-space low-pass filter is employed to suppress spatial frequencies beyond $\kappa_{\max} > 2\pi/\lambda_{\min}$ along with an apodization filter in (x, y) [17].

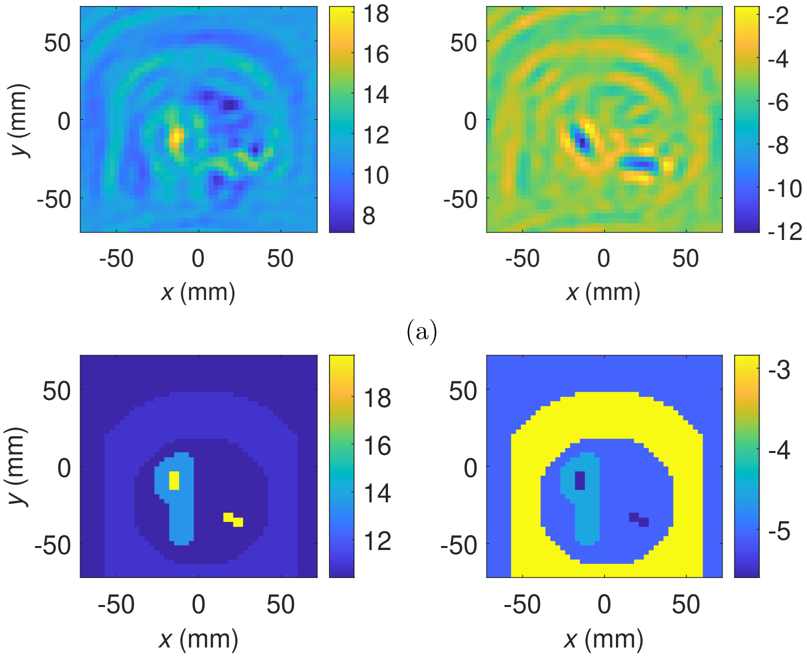

(a)

(b)

Figure 4.11: 2D QMH reconstructions of the real part (left) and the imaginary part (right) of the relative permittivity of the breast phantom using (a) the proposed combined Born/Rytov reconstruction. (b) is the averaged permittivity map across the phantom. A k-space low-pass filter is employed to suppress spatial frequencies beyond $\kappa_{\text{max}} > 2\pi/\lambda_{\text{min}}$ along with an apodization filter in (x, y) [17].

imaginary-permittivity image identifies only the tumor inclusions inside the fibroglandular tissue simulant. The Gibb's (ripple) artifacts at the phantom-background interface are strong. They are caused by the abrupt change in the imaginary part of the permittivity at this interface (see Table I for the imaginary-permittivity values of the carbon-rubber and matching materials) as well as the gaps introduced by the plastic wrap and the air gaps trapped in it. Also, the size of the phantom is large, violating the first-order Born approximation limit.

In the modified-Rytov reconstruction (see Fig. 4.10b), the two tumor-simulant groups, particularly in the imaginary part of the permittivity, are visible very well. Indeed, the response in the imaginary part of the permittivity is so significant that Gibbs artifacts are generated at their boundaries. This is due to the loss affecting significantly the magnitude of the measured OUT transmission coefficients. Importantly, the images are much less affected by ripple artifacts at the phantom edges. This is explained by the fact that only the magnitude of the OUT data is used, which is less sensitive to the presence of the very small gaps formed by the plastic wrap.

Utilizing the Marks approximation (with $n = 2$) leads to an increase in the overall noise of the reconstruction (see Fig. 4.10c) due to phase-wrapping problems. The artifacts clutter the image and reduce its overall fidelity, in particular in the imaginary response. Nonetheless, the real-permittivity image localizes the tumor simulants.

The proposed combined Born/Rytov approach produces images, which contain structural features from both the Born-based and the Rytov-based reconstructions, which is expected. The significant rippling artifacts from the Born approximation are reduced. This results in a much clearer estimate of the fibroglandular structure while at the same time preserving the image features due to the embedded tumors.

Overall, the image quality exceeds that of the images generated with the previous three approaches.

We note that the individual tumor simulants (two at each location) cannot be differentiated in neither of the images. The tumor simulants are spherical with 1 cm diameter and they are touching each other at both locations, i.e., the center-to-center distance is 1 cm. This is expected bearing in mind that the shortest wavelength in the carbon-rubber material is 11.3 mm and the target viewing angle is severely limited by attenuation.

4.7 Conclusion

In this work, the combined Born/Rytov quantitative microwave holography approach is proposed and explored via simulation-based and experimental imaging examples. The Born and Rytov approximations, when applied separately, yield markedly different images in the cases where their respective limits are violated. Depending on the specific imaging scenario, one approximation outperforms the other. The Born approximation performs better in recovering small scatterers and it tolerates a much wider range of object permittivity values in a low-permittivity background. However, when electrically large objects in a high-permittivity background are imaged, the Rytov-based reconstruction is advantageous and it exhibits an ability to better identify smaller scatterers embedded in larger objects, especially with transmission measurements. A major drawback of Rytov's approximation is its susceptibility to phase-unwrapping errors. This drawback is eliminated in the proposed approach, which removes the need to phase-unwrap the data. It only requires phase unwrapping of the system PSF, which is generally successful due to the fact that the PSF is the response to a weak point-like scatterer. The integration of the two approximations into one approach allows to leverage their advantages without increasing the computational complexity of the reconstruction and preserving its real-time performance. We note that the experimental and simulation-based reconstructions presented here are computed in MATLAB [51] within 2 to 3 seconds on a personal laptop without any parallel computing or code optimization.

One of the main applications of QMH is near-field biomedical imaging. In this application, the real-time reconstruction ability is critical since it dramatically increases the diagnostic capability. Within a minute, various image sets can be generated and image enhancement can be performed by: (i) tuning the *ad hoc* parameters of apodization and Fourier-space filters, (ii) changing the data approximation strategy (e.g., Born or the proposed combined approach), and (iii) employing system PSFs acquired in different backgrounds and with different scattering probes. Furthermore, it can potentially enable imaging during dynamic processes (e.g., breathing and circulation) in real time.

Future work aims to explore the use of multiple PSFs acquired with varying permittivities of the background and the scattering probe to improve the quantitative accuracy of the images. The best quantitative accuracy is achieved in regions of the imaged objects, the permittivity of which is close to that of the scattering probe [19]. Since the permittivity of the scattering probe is known, it is in principle possible to determine which regions in the images have high quantitative accuracy and which need further enhancement. Also, further explorations into acquiring 3D images without measuring scattering probes at each z' slice could yield significant benefit by reducing system-calibration effort.

REFERENCES

[1] D. M. Sheen, D. L. McMakin, and T. E. Hall, “Three-dimensional millimeter-wave imaging for concealed weapon detection,” *IEEE Trans. Microw. Theory Techn.*, vol. 49, no. 9, pp. 1581–1592, Sep. 2001.

[2] D. Sheen, D. McMakin, and T. Hall, “Near-field three-dimensional radar imaging techniques and applications,” *Appl. Opt.*, vol. 49, no. 19, pp. E83–E93, Jun. 2010.

[3] R. Zoughi, *Microwave Non-destructive Testing and Evaluation Princples.* Kluwer Academic Publishers, 2012.

[4] L. Diener, “Microwave near-field imaging with open-ended waveguide—comparison with other techniques of nondestructive testing,” *Research in Nondestructive Evaluation*, vol. 7, no. 2–3, pp. 137–152, Jun 1995.

[5] R. Zoughi, *Microwave Nondestructive Testing and Evaluation.* Amsterdam, The Netherlands: Kluwer, 2000.

[6] D. O’Loughlin, M. O’Halloran, B. M. Moloney, M. Glavin, E. Jones, and M. A. Elahi, “Microwave breast imaging: Clinical advances and remaining challenges,” *IEEE Transactions on Biomedical Engineering*, vol. 65, no. 11, pp. 2580–2590, 2018.

[7] E. Porter, M. Coates, and M. Popović, “An early clinical study of time-domain microwave radar for breast health monitoring,” *IEEE Trans. Biomed. Eng.*, vol. 63, no. 3, pp. 530–539, Mar. 2016.

[8] L. Kranold, C. Quintyne, M. Coates, and M. Popović, "Clinical study with a time-domain microwave breast monitor: Analysis of the system response and patient attributes," in *13th Eur. Conf. Antennas Propag. EuCAP*, 2019, pp. 1–5.

[9] N. K. Nikolova, *Introduction to Microwave Imaging.* Cambridge, United Kingdom: Springer Science & Business Media, 2017.

[10] M. Pastorino, *Microwave Imaging.* John Wiley & Sons, Ltd, 2010.

[11] M. Pastorino and A. Randazzo, *Microwave Imaging Methods and Applications.* Artech House Publishers, 2018.

[12] Y. M. Wang and W. C. Chew, "An iterative solution of the two-dimensional electromagnetic inverse scattering problem," *Int. J. Imag. Sys. Tech.*, vol. 1, no. 1, pp. 100–108, 1989.

[13] W. C. Chew and Y. M. Wang, "Reconstruction of two-dimensional permittivity distribution using the distorted Born iterative method," *IEEE Trans. Med. Imag.*, vol. 9, no. 2, pp. 218–225, Jun. 1990.

[14] K. Noritake and S. Kidera, "Boundary extraction enhanced distorted born iterative method for microwave mammography," *IEEE Antennas Wireless Propag. Lett.*, vol. 18, no. 4, pp. 776–780, 2019.

[15] M. Slaney, A. C. Kak, and L. E. Larsen, "Limitations of imaging with first-order diffraction tomography," *IEEE Trans. Microw. Theory Techn.*, vol. 32, no. 8, pp. 860–874, 1984.

[16] M. Kaveh, M. Soumekh, and R. Mueller, “A comparison of born and rytov approximations in acoustic tomography,” in *Acoustical Imaging*, J. P. Powers, Ed. Boston: Springer, 1982, ch. 10, pp. 325–335.

[17] D. Tajik, A. D. Pitcher, and N. K. Nikolova, “Comparative study of the Rytov and Born approximations in quantitative microwave holography,” *Prog. Electromagn. Res. B*, vol. 79, pp. 1–19, Jan. 2017.

[18] D. L. Marks, “A family of approximations spanning the Born and Rytov scattering series,” *Opt. Express*, vol. 14, no. 19, pp. 8837–8848, Sep. 2006. [Online]. Available: http://www.opticsexpress.org/abstract.cfm?URI=oe-14-19-8837

[19] S. Tu, J. J. McCombe, D. S. Shumakov, and N. K. Nikolova, “Fast quantitative microwave imaging with resolvent kernel extracted from measurements,” *Inverse Probl.*, vol. 31, no. 4, p. 045007, Apr. 2015.

[20] D. Tajik, N. K. Nikolova, and M. D. Noseworthy, “Improving quantitative microwave holography through simultaneous use of the Born and Rytov approximations,” in *16th Euro. Radar Conf. EuRAD*, Nov. 2019.

[21] D. S. Shumakov, D. Tajik, A. S. Beaverstone, and N. K. Nikolova, “Real-time quantitative reconstruction methods in microwave imaging,” in *The World of Applied Electromagnetics In Appreciation of Magdy Fahmy Iskander*, A. Lakhtakia and C. M. Furse, Eds. New York, USA: Springer, 2017, ch. 17, p. 415–442.

[22] D. Tajik, F. Foroutan, D. S. Shumakov, A. D. Pitcher, and N. K. Nikolova, “Real-time microwave imaging of a compressed breast phantom with planar scanning,”

IEEE J. Electromagn., RF, Microw. Med. Biol., vol. 2, no. 3, pp. 154–162, Sep. 2018.

[23] R. K. Amineh, M. Ravan, H. Wu, and A. Kasturi, "Three-dimensional holographic imaging using data collected over cylindrical apertures," *Microw. Opt. Technol. Lett.*, vol. 61, no. 4, pp. 907–911, Jul. 2019. [Online]. Available: https://onlinelibrary.wiley.com/doi/abs/10.1002/mop.31694

[24] D. Tajik, J. Trac, and N. K. Nikolova, "Quality control of microwave equipment for tissue imaging," *IEEE J. Electromagn., RF, Microw. Med. Biol.*, vol. 4, no. 1, pp. 52–60, Mar. 2019.

[25] D. Tajik, J. Trac, and N. K. Nikolova, "Spatial resolution evaluation of a microwave system for breast cancer screening," in *13th Euro. Conf. Antennas Propag. EuCAP*, Jun. 2019, pp. 1–5.

[26] W. C. Chew, *Waves and Fields in Inhomogeneous Media.* IEEE Press, 1990.

[27] R. K. Amineh, M. Ravan, A. Khalatpour, and N. K. Nikolova, "Three-dimensional near-field microwave holography using reflected and transmitted signals," *IEEE Transactions on Antennas and Propagation*, vol. 59, no. 12, pp. 4777–4789, 2011.

[28] A. S. Beaverstone, D. S. Shumakov, and N. K. Nikolova, "Integral equations of scattering for scalar frequency-domain responses," *IEEE Trans. Microw. Theory Techn.*, vol. 64, no. 4, pp. 1120–1132, Apr. 2015.

[29] X. Zhuge and A. G. Yarovoy, "Three-dimensional near-field MIMO array imaging using range migration techniques," *IEEE Trans. Image Process.*, vol. 21, no. 6, pp. 3026–3033, 2012.

[30] J. M. Lopez-Sanchez and J. Fortuny-Guasch, "3-d radar imaging using range migration techniques," *IEEE Trans. Antennas Propag.*, vol. 48, no. 5, pp. 728–737, 2000.

[31] C. Prati, F. Rocca, A. Guarnieri, and E. Damonti, "Seismic migration for SAR focusing: Interferometrical applications," *IEEE Trans. Geosci. Remote Sens.*, vol. 28, no. 4, pp. 627–640, 1990.

[32] G. Wang, F. Qi, Z. Liu, C. Liu, C. Xing, and W. Ning, "Comparison between back projection algorithm and range migration algorithm in terahertz imaging," *IEEE Access*, vol. 8, pp. 18 772–18 777, 2020.

[33] D. M. Sheen, D. L. McMakin, H. D. Collins, T. E. Hall, and R. H. Severtsen, "Concealed explosive detection on personnel using a wideband holographic millimeter-wave imaging system," *Proc. SPIE 2755, Signal Processing, Sensor Fusion, and Target Recognition V*, Jun. 1996.

[34] J. Gao, Y. Qin, B. Deng, H. Wang, and X. Li, "A novel method for 3-d millimeter-wave holographic reconstruction based on frequency interferometry techniques," *IEEE Trans. Microw. Theory Techn.*, vol. 66, no. 3, pp. 1579–1596, 2018.

[35] Y. Meng, C. Lin, J. Zang, A. Qing, and N. K. Nikolova, "General theory of holographic inversion with linear frequency modulation radar and its application

to whole-body security scanning," *IEEE Trans. Microw. Theory Techn.*, vol. 68, no. 11, pp. 4694–4705, 2020.

[36] " The Stolt Method," Stanford University, Oct. 2021. [Online]. Available: http://sepwww.stanford.edu/sep/prof/iei/omk/paper_html/node11.html

[37] A. Breglia, A. Capozzoli, C. Curcio, and A. Liseno, "NUFFT-based interpolation in backprojection algorithms," *IEEE Geosci. Remote Sens. Lett.*, pp. 1–5, 2020.

[38] Multi-purpose electromagnetic field simulation tool (MEFiSTo). [Online]. Available: http://www.wisethought.ca/Products.htm

[39] B. Chen and J. J. Stamnes, "Validity of diffraction tomography based on the first Born and the first Rytov approximations," *Appl. Opt.*, vol. 37, no. 14, pp. 2996–3006, May 1998. [Online]. Available: http://ao.osa.org/abstract.cfm?URI=ao-37-14-2996

[40] J. Krehl and A. Lubk, "The Rytov approximation in electron scattering," *Physical Review B*, vol. 95, 03 2017.

[41] T. E. Gureyev, T. J. Davis, A. Pogany, S. C. Mayo, and S. W. Wilkins, "Optical phase retrieval by use of first born- and rytov-type approximations," *Appl. Opt.*, vol. 43, no. 12, pp. 2418–2430, Apr 2004. [Online]. Available: http://ao.osa.org/abstract.cfm?URI=ao-43-12-2418

[42] N. Qaddoumi, A. H. El-hag, M. Al Hosani, I. A. Mansouri, and H. A. Ghufli, "Detecting defects in outdoor non-ceramic insulators using near-field microwave non-destructive testing," *IEEE Transactions on Dielectrics and Electrical Insulation*, vol. 17, no. 2, pp. 402–407, 2010.

[43] E. Fear, X. Li, S. Hagness, and M. Stuchly, “Confocal microwave imaging for breast cancer detection: localization of tumors in three dimensions,” *IEEE Transactions on Biomedical Engineering*, vol. 49, no. 8, pp. 812–822, 2002.

[44] M. Klemm, I. J. Craddock, A. Preece, J. Leendertz, and R. Benjamin, “Evaluation of a hemi-spherical wideband antenna array for breast cancer imaging,” *Radio Science*, vol. 43, no. 6, 2008. [Online]. Available: https://agupubs.onlinelibrary.wiley.com/doi/abs/10.1029/2007RS003807

[45] T. M. Grzegorczyk, P. M. Meaney, P. A. Kaufman, R. M. diFlorio Alexander, and K. D. Paulsen, “Fast 3-D tomographic microwave imaging for breast cancer detection,” *IEEE Transactions on Medical Imaging*, vol. 31, no. 8, pp. 1584–1592, 2012.

[46] H. Song, S. Sasada, T. Kadoya, M. Okada, K. Arihiro, X. Xiao, and T. Kikkawa, “Detectability of breast tumor by a hand-held impulse-radar detector: Performance evaluation and pilot clinical study,” *Nature Scientific Reports*, vol. 7, no. 1, p. 16353, 2017.

[47] T. Negishi, G. Gennarelli, F. Soldovieri, Y. Liu, and D. Erricolo, “Radio frequency tomography for nondestructive testing of pillars,” *IEEE Trans. Geosci. Remote Sens.*, vol. 58, no. 6, pp. 3916–3926, 2020.

[48] K. Itoh, “Analysis of the phase unwrapping algorithm,” *Appl. Opt.*, vol. 21, no. 14, pp. 2470–2470, Jul 1982. [Online]. Available: http://ao.osa.org/abstract.cfm?URI=ao-21-14-2470

[49] D. C. Ghiglia and L. A. Romero, “Robust two-dimensional weighted and unweighted phase unwrapping that uses fast transforms and iterative methods,” *J. Opt. Soc. Am. A*, vol. 11, no. 1, pp. 107–117, Jan 1994. [Online]. Available: http://josaa.osa.org/abstract.cfm?URI=josaa-11-1-107

[50] M. A. Herráez, D. R. Burton, M. J. Lalor, and M. A. Gdeisat, “Fast two-dimensional phase-unwrapping algorithm based on sorting by reliability following a noncontinuous path,” *Appl. Opt.*, vol. 41, no. 35, pp. 7437–7444, Dec 2002. [Online]. Available: http://ao.osa.org/abstract.cfm?URI=ao-41-35-7437

[51] “MATLAB Signal Processing Toolbox,” The MathWorks, Natick, MA, USA, 2014.

[52] Altiar FEKO, Electromagnetic Simulation Software. [Online]. Available: https://altairhyperworks.com/product/FEKO

[53] J. W. Goodman, *Introduction to Fourier Optics.* New York, USA: McGraw-Hill, 1996.

[54] J. Melnikow, J. J. Fenon, and E. P. Whitlock, *Supplemental Screening for Breast Cancer in Women With Dense Breasts: A Systematic Review for the U.S. Preventive Service Task Force.* Agency for Healthcare Research and Quality (US), Jan 2016, no. 126. [Online]. Available: http://ao.osa.org/abstract.cfm?URI=ao-41-35-7437

[55] R. K. Amineh, A. Trehan, and N. K. Nikolova, “TEM horn antenna for ultra-wide band microwave breast imaging,” *Prog. Electromagn. Res. B*, vol. 13, pp. 59–74, 2009.

[56] R. K. Amineh, J. J. McCombe, A. Khalatpour, and N. K. Nikolova, "Microwave holography using measured point-spread functions," *IEEE Trans. Instrum. Meas.*, vol. 64, no. 2, pp. 403–417, Feb. 2015.

[57] R. K. Amineh, M. Ravan, J. McCombe, and N. K. Nikolova, "Three-dimensional microwave holographic imaging employing forward-scattered waves only," *Int. J. Antennas and Propagation*, vol. 2013, p. 97287, 2013.

CHAPTER 5

ACCURATE RANGE MIGRATION FOR FAST QUANTITATIVE FOURIER-BASED IMAGE RECONSTRUCTION WITH MONOSTATIC RADAR

Preface

This chapter is a reproduction of a manuscript in preparation to be submitted to the Transaction on Microwave Theory and Techniques:

D. Tajik, R. Kazemivala, J. Nguyen, and N. K. Nikolova, "Accurate range migration for fast quantitative Fourier-based image reconstruction with monostatic radar," in *IEEE Transactions on Microwave Theory and Techniques*, Submitted Mar. 18, 2022.

I designed and performed the measurements (both simulated and experimental), assisted in the theoretical development of the range migration technique, implemented the quantitative microwave holography (QMH) algorithm and the range migration algorithm, performed the image reconstruction, and wrote/edited the manuscript. Romina Kazemivala assisted in the development and testing of the range migration technique and reviewed the manuscript. Jimmy Nguyen assisted in the experimental measurements and reviewed the manuscript. Natalia K. Nikolova developed the theoretical outline of the range migration technique and edited the manuscript.

5.1 Introduction

Fourier-based image reconstruction is used in numerous applications of wave scattering, including ground-penetrating radar, nondestructive testing, biomedical imaging, concealed weapon detection, target localization and tracking, and many more [1–11]. By acquiring the wavefront's magnitude and phase across a finite surface (the acquisition aperture), target localization and image generation is possible in a three-dimensional (3D) volume [12]. The benefit of performing the reconstruction in Fourier (or wavenumber) space is the remarkable computational speed. Since the inverse problem is cast as a deconvolution, solving it in Fourier space leads to drastic reduction of the computational complexity compared to the real-space solution [13].

A common challenge among the Fourier-based imaging algorithms is how to resolve objects along the range (or depth) dimension (see Fig. 5.1). Range migration (or range focusing) techniques have been previously developed for varying scenarios [14–18]. One common method in synthetic aperture radar (SAR) exploits the Stolt mapping [19–21], which maps the data frequency (ω) dependence into k_z dependence of the form $\sim \exp(-\mathrm{i}k_z z)$ (range migration), where k_z is the Fourier variable corresponding to the range (z) real-space variable and $\mathrm{i} = \sqrt{-1}$. This allows for target reflectivity recovery via 3D inverse Fourier transform. Range stacking [22–25] avoids the somewhat computationally expensive Stolt mapping but it, too, needs the range migration factor to represent analytically the z-dependence of the scattered field. Range migration approaches depend on the resolvent kernel of the chosen forward model of scattering. This kernel is proportional to the product of the total internal field (due to the transmitting antenna) and the background Green's function [13].

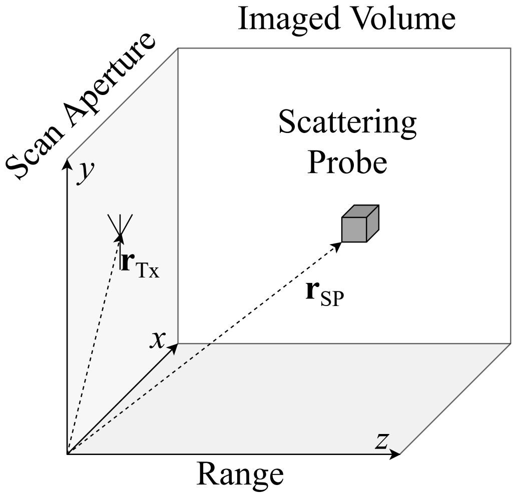

Figure 5.1: Image of a typical point-spread function measurement using a planar scanning aperture.

Since range migration is common in fast real-time image reconstruction, it is usually applied with linearized scattering models where the total internal field is replaced by the incident field due to the transmitting (Tx) antenna as per the 0th-order Born approximation. On the other hand, Green's function is equivalent to the incident field due to the receiving (Rx) antenna if this antenna were to transmit [13, 26]. In far-field imaging, both of these fields are approximated as plane waves, leading to the simple range-migration factor of $\sim \exp(-\mathrm{i}k_z z)$ in Fourier space; see, e.g., [27].

An improvement in accuracy is achieved by an assumption that, while the transmitted field is a plane wave, the scattering is a superposition of spherical waves emanating from the scattering centers building the object under test (OUT); see, e.g., [16, 25]. By reciprocity, this also means that Green's function is in the form of a spherical wave. The improvement is due to the ability of the spherical-wave model to account better for the amplitude variations of the measured data over the acquisition aperture especially in close-range applications, e.g., the whole-body imaging for concealed weapon detection.

The data amplitude dependence on the range distance to target is the most pronounced in near-field imaging where the extent of the acquisition aperture is much larger than the range distance to the target. In order to make Fourier-based real-time 3D imaging applicable to these scenarios, it is imperative to devise a range-migration strategy that takes into account the spherical spread of *both* the transmitted field and the Green function. Here, we propose an accurate range-migration formula, which is applicable directly in the Fourier-transformed data space. The result is analytical and thus it does not increase the running time.

The proposed range-migration approach is applicable not only to the conventional qualitative Fourier-based image reconstruction methods. Recently, Fourier-based quantitative image-reconstruction methods have been proposed [9,28–30]. The quantitative output, i.e., the reconstruction of the dielectric profile of an OUT, becomes possible with the use of measured system point-spread functions (PSFs) in place of analytical/simulated resolvent kernels. The PSF is the measured system response to an electrically small scattering probe and the acquisition of the PSF data sets is part of the system calibration. However, the use of a measured PSF is not without its drawbacks. One important drawback is the significant number of PSF measurements required for 3D imaging with dense sampling along range. Since each range slice in the image requires a PSF, the calibration effort may render the approach impractical. Thus, a method to analytically refocus a measured PSF (with the probe at one range distance) to any other desired range distance is desired.

The contribution of this work is the derivation of an accurate analytical representation of the range dependence of the resolvent kernel of the monostatic-radar scattering model in Fourier space. This representation can be employed directly in the qualitative Fourier-based image-reconstruction algorithms for improved accuracy without increasing the computational requirements. In quantitative Fourier-based imaging employing measured PSFs, the representation leads to a magnitude-and-phase scaling factor that is applied to the Fourier-transformed PSF in order to refocus it to any desired range-slice location. This range-migration technique reduces the calibration effort to a single PSF measurement, which is critically important for practical 3D imaging applications. A comparison with the conventional far-field range-migration approach confirms the improvement in the re-focused PSF accuracy and the final image structural and quantitative accuracy. We also highlight the limitations of the method related to the initial PSF measurement position and give recommendations for Fourier-domain filtering based on the maximum viewing angle relative to the refocused scattering-probe range location. The method is validated with both simulated and experimental data used in image reconstruction with quantitative microwave holography (QMH) [9,28,31].

5.2 Range Migration for Monostatic Radar

In the following derivations, we employ the stationary phase approximation (SPA), which is a method for approximating integrals in the form [32]:

$$\iint_{-\infty}^{\infty} f(x,y) e^{\mathrm{i}p\phi(x,y)} dx dy \approx K \cdot \frac{2\pi}{\sqrt{|\det \Phi|}} f(x_0,y_0) e^{\mathrm{i}p\phi(x_0,y_0)} \tag{5.1}$$

in the limit of the positive parameter $p \to \infty$. Here, $f(x,y)$ and $\phi(x,y)$ are real functions and their values $f(x_0,y_0)$ and $\phi(x_0,y_0)$ are at the *stationary phase* positions, where:

$$\frac{\partial \phi(x_0, y_0)}{\partial x} = \frac{\partial \phi(x_0, y_0)}{\partial y} = 0 \tag{5.2}$$

and

$$\Phi = \begin{bmatrix} \frac{\partial^2 \phi(x_0,y_0)}{\partial x^2} & \frac{\partial^2 \phi(x_0,y_0)}{\partial x \partial y} \\ \frac{\partial^2 \phi(x_0,y_0)}{\partial y \partial x} & \frac{\partial^2 \phi(x_0,y_0)}{\partial y^2} \end{bmatrix} \tag{5.3}$$

$$K = \begin{cases} \mathrm{i}, \text{ if } \det \Phi > 0, \operatorname{tr} \Phi > 0 \\ -\mathrm{i}, \text{ if } \det \Phi > 0, \operatorname{tr} \Phi < 0 \\ 1, \text{ if } \det \Phi < 0 \,. \end{cases} \tag{5.4}$$

Note that the approximation becomes more accurate as $p \to \infty$, but notations are simplified by setting $p = 1$ [32].

5.2.1 Range Migration for Monostatic Scattering

Consider a scattering probe (SP) at the center of the imaged volume $(x', y', z') = (0, 0, 0)$ and a monostatic measurement of the respective PSF, where the Tx and Rx antennas are co-located and scanning together on an acquisition plane at $\bar{z} = const$ ($\bar{z} > 0$) along x and y. In order to employ the well-known Green function of the scalar Helmholtz equation, we make the following assumptions about the measured PSF data: (i) it captures correctly the signal strength at the range distance $\bar{z}$ as determined by the system transmitter, (ii) it also captures the antennas' polarization and directivity properties, which are not expected to vary significantly when the range position of the point scatterer changes within the image z' extent, (iii) the evanescent field components are negligible. The remaining amplitude and phase dependence

$S(x, y)$ of the PSF on the distance between the Tx/Rx antennas and the SP is then:

$$S(x, y, k) = \frac{e^{-\mathrm{i}rk}}{4\pi r} \cdot \frac{e^{-\mathrm{i}rk}}{4\pi r} \tag{5.5}$$

where $r = \sqrt{x^2 + y^2 + \bar{z}^2}$, $k = 2\pi/\lambda$ is the background wavenumber $k \in \mathbb{R}$, and λ is the respective wavelength. The 2D Fourier transform (FT) of $S(x, y)$ is

$$\widetilde{S}(k_x, k_y, k) = \iint \frac{e^{-\mathrm{i}r2k}}{16\pi^2 r^2} \cdot e^{-\mathrm{i}(k_x x + k_y y)} dx dy\,. \tag{5.6}$$

Taking into account (5.1) and (5.2), the phase function for the given k is determined to be

$$\phi(x, y) = -r2k - k_x x - k_y y \tag{5.7}$$

and its derivatives are

$$\frac{\partial \phi(x, y)}{\partial x} = -2k\frac{x}{r} - k_x \tag{5.8}$$

$$\frac{\partial \phi(x, y)}{\partial y} = -2k\frac{y}{r} - k_y\,. \tag{5.9}$$

From (5.8) and (5.9), the stationary phase positions are obtained:

$$\frac{x_0}{r_0} = -\frac{k_x}{2k}\,, \quad \frac{y_0}{r_0} = -\frac{k_y}{2k} \tag{5.10}$$

where $r_0 = \sqrt{x_0^2 + y_0^2 + \bar{z}^2}$. The phase $\phi(x_0, y_0)$ at the stationary position is now obtained as:

$$\phi(x_0, y_0) = -\frac{r_0}{2k}(4k^2 - k_x^2 - k_y^2)\,. \tag{5.11}$$

We next introduce the spectral variable k_z as

$$k_z^2 = 4k^2 - k_x^2 - k_y^2\,. \tag{5.12}$$

Using (5.10) along with the definition in (5.12), leads to a relation between z and k_z, which is analogous to those for x and y in (5.10), namely,

$$\left(\frac{\bar{z}}{r_0}\right)^2 = \left(\frac{k_z}{2k}\right)^2\,. \tag{5.13}$$

Note that (5.10) along with (5.13) imply that:

$$\left(\frac{x}{\bar{z}}\right)^2 = \left(\frac{k_x}{k_z}\right)^2\,, \quad \left(\frac{y}{\bar{z}}\right)^2 = \left(\frac{k_y}{k_z}\right)^2\,. \tag{5.14}$$

Using these relations, we cast the stationary phase as a function of k_z and $\bar{z}$, which, in the case of $\bar{z} > 0$, is

$$\phi(x_0, y_0) = -\sqrt{k_z^2} \cdot \bar{z}\,. \tag{5.15}$$

It is now clear that if k_z is imaginary, i.e., $k_x^2 + k_y^2 > (2k)^2$, the phase function becomes imaginary and violates the SPA requirement that the phase function is real-valued. An imaginary k_z corresponds to modes evanescent along z and, indeed, such modes have been dismissed in the assumptions leading to the use of the monostatic resolvent kernel in (5.5). Hereafter, only real-valued k_z are considered, so that (5.15) is written as

$$\phi(x_0, y_0) = -k_z \bar{z} \tag{5.16}$$

where

$$k_z = \sqrt{4k^2 - k_x^2 - k_y^2}\,. \tag{5.17}$$

To determine the value of the constant K in (5.4), we need the determinant of $\Phi(x_0, y_0)$ in (5.3), which is found to be:

$$\det\Phi = k_z^2/r_0^2 > 0. \tag{5.18}$$

Further, the trace $\operatorname{tr}\Phi$ is found as:

$$\operatorname{tr}\Phi = -\frac{2k}{r_0}\left[1 - \left(\frac{x_0}{r_0}\right)^2 + 1 - \left(\frac{y_0}{r_0}\right)^2\right] < 0\,. \tag{5.19}$$

It then follows from (5.4) that

$$K = -\mathrm{i} \tag{5.20}$$

and the FT of $S(x, y, k)$ for a probe at $(0, 0, 0)$ is found as

$$\widetilde{S}(k_x, k_y, k; 0) = \frac{1}{\mathrm{i}16\pi k\cdot\bar{z}}e^{-\mathrm{i}k_z\bar{z}},\ \bar{z}, k, k_z > 0\,. \tag{5.21}$$

Here, the last argument in $(k_x, k_y, k; 0)$ emphasizes the probe's range position. The expression in (5.21) is the FT of the resolvent kernel in (5.5). As such it can be used directly in qualitative Fourier-based reconstruction algorithms (e.g., microwave holography and range stacking) bearing in mind that $\bar{z}$ represents the range distance from the probe to the acquisition aperture. Notice that, unlike previous range migration formulas, where $\widetilde{S} \sim e^{-\mathrm{i}k_z\bar{z}}$ or $\widetilde{S} \sim e^{-\mathrm{i}k_z\bar{z}}/k_z$, the expression in (5.21) also contains $\bar{z}$ in the denominator. This is a consequence of the kernel's amplitude dependence

$\sim 1/r^2$ in real space.

Consider now the case where the PSF has been measured with the probe at $(x', y', z') = (0, 0, 0)$ but the PSF for a probe at $(0, 0, z')$ is desired. Now, the range distance between the acquisition plane and the SP is $\bar{z} - z'$. Similarly to the case of $z' = 0$, we set $\bar{z} - z' > 0$. The FT of the corresponding kernel is

$$\widetilde{S}(k_x, k_y, k; z') = \frac{1}{\mathrm{i}16\pi k \cdot (\bar{z} - z')} e^{-\mathrm{i}k_z \cdot (\bar{z} - z')} \,. \tag{5.22}$$

Dividing (5.22) with (5.21) provides the range-migration scaling factor that can be applied to refocus any measured PSF to a new range location:

$$\frac{\widetilde{S}(k_x, k_y, k; z')}{\widetilde{S}(k_x, k_y, k; 0)} = \left(\frac{\bar{z}}{\bar{z} - z'} \right) e^{-\mathrm{i}k_z \cdot z_\xi} \,. \tag{5.23}$$

This is the factor used to refocus measured PSFs, such as those utilized in QMH. Its PSFs, denoted as $\widetilde{H}(k_x, k_y, z'; \omega)$, employ (5.23) in the form

$$\widetilde{H}(k_x, k_y, z_0 + \Delta z; \omega) = \widetilde{H}(k_x, k_y, z_0; \omega) \frac{z_0 e^{-\mathrm{i}k_z \Delta z}}{z_0 + \Delta z} \,, \tag{5.24}$$

where z_0 is the aperture-to-probe distance at which the PSF is measured and Δz is the increase ($\Delta z > 0$) or decrease ($\Delta z < 0$) of this distance when the PSF is refocused. Compare this to the conventional plane-wave range migration technique derived from the angular spectrum representation [32]:

$$\widetilde{H}(k_x, k_y, z_0 + \Delta z; \omega) = \widetilde{H}(k_x, k_y, z_0; \omega) e^{-\mathrm{i}k_z \Delta z} \,. \tag{5.25}$$

It is obvious that if the shift along range is insignificant relative to z_0, (5.25) is acceptable. Yet, in close-range imaging, where the imaged volume is sampled at range intervals of similar order of magnitude to z_0, the magnitude scaling factor is not negligible. This becomes especially important in quantitative imaging, where the accuracy of the approximation directly impacts the accuracy of the permittivity estimates.

5.2.2 Analytical Example With Finite Apertures

This example validates the result in (5.24) and is used to study the impact of the aperture size. The FT in (5.6) is first computed via the discrete Fourier transform (DFT) with the frequency set to 3 GHz ($\lambda \approx 0.1$ m). When computing the real-space function (5.5), the x and y spatial sampling steps are set to 0.025 m. The aperture extent is 12 m along x and y. The probe is positioned 0.2 meters away from the aperture. This DFT serves as a reference. The SPA solution (5.21) is also computed (with all imaginary values of k_z set to 0) and compared with the DFT result in Fig. 5.2.

It is clear that the SPA and the DFT results match well. A circle circumscribes the $4k^2 = k_x^2 + k_y^2$ region (of radius of $2k$), separating in the propagating and evanescent regions in k-space. At this circle (for the DFT case), minor Gibb's effects due to the Fourier transform of a finite aperture appears to create rippling artifacts at $k_x = \pm 125$, where the magnitude plot transitions rapidly [6]. It is especially clear in the DFT case that the contributions in the propagating region are much more dominant in magnitude than the evanescent region. By setting the evanescent region of k-space to zero, a close correlation with the DFT result is achieved since the attenuation (in the DFT case) is extremely rapid.

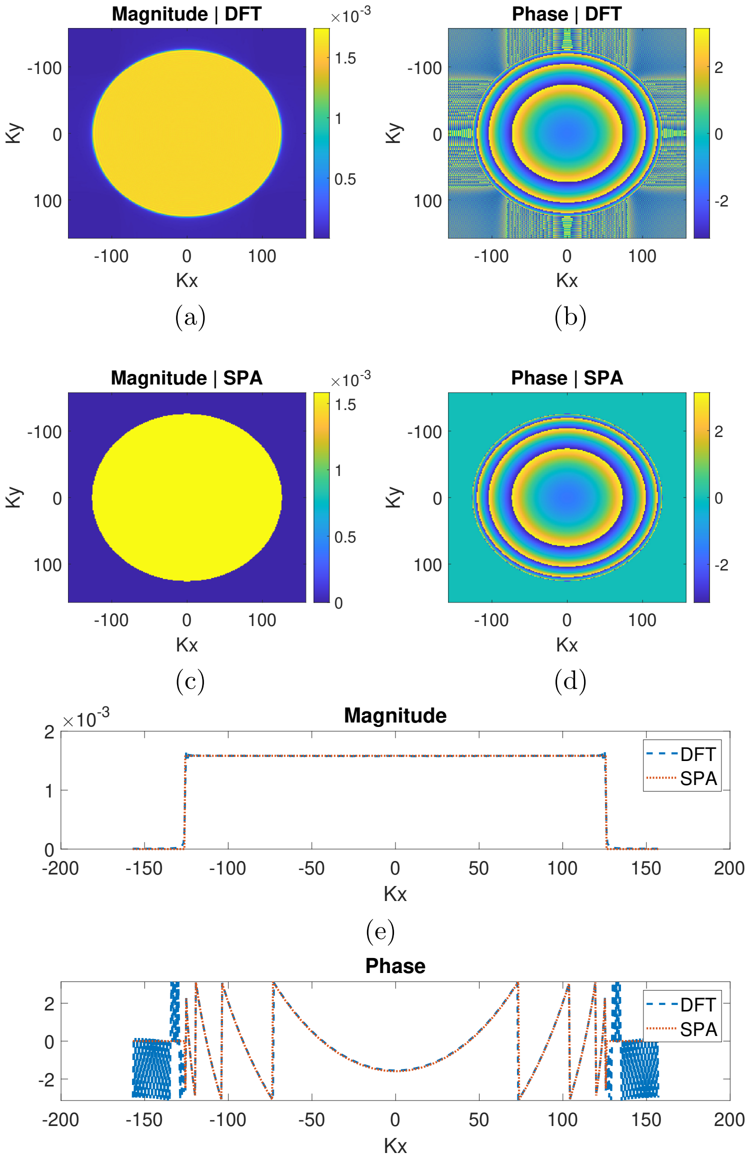

(a) (b)

(c) (d)

(e)

(f)

Figure 5.2: Fourier-domain counterpart of the monostatic kernel function (5.5) sampled on a 12×12 m^2 aperture with a probe positioned at $z = 0.2$ m from the aperture: (a) magnitude and (b) phase of the DFT of (5.5), (c) magnitude and (d) phase of the SPA solution (5.21), (e) magnitude and (f) phase 1-dimensional (1D) plots at $k_y = 0$ of the DFT and SPA approaches.

In practice, large apertures such as the one considered here (of extent 120λ in both x and y) are rarely implemented in near-field imaging. Consider instead a situation where the aperture is limited to a maximum viewing angle of 45° (aperture size of 0.4×0.4 m^2). The results are shown in Fig. 5.3. The Fourier domain sampling step is tied to the aperture size, and thus the lower k-space sampling step becomes apparent in Fig. 5.3.[1] Note also that the accuracy of the approximation is reduced, as large Gibb's artifacts are now present and distorting the DFT result.

It is well-known that the k-space region of the measured scattered-field propagating modes is also limited by the maximum target viewing angle α [13]. The viewing angle in monostatic measurements is the angle of arrival of the scattered wave relative to the aperture's unit normal. A reception at grazing angles ($\alpha \approx \pm 90°$) ensures the availability of propagating modes with wavenumbers k_x and k_y as high as to fulfill $k_x^2 + k_y^2 \approx (2k)^2$. However, often such reception is not achievable due to the finite size of the aperture or the limited beamwidth of the antennas. In this case, $\alpha < 90°$. and the values of k_x and k_y are limited by the projection of the wave vector $\mathbf{k}$ onto the acquisition aperture, i.e., $k_\alpha = k \sin \alpha$. In monostatic radar, this sets the k-space region to a circle of radius $2k_\alpha$:

$$k_x^2 + k_y^2 \leq (2k_\alpha)^2. \tag{5.26}$$

The two circles drawn on Figs. 5.3a and 5.3b highlight the $2k$ and $2k_\alpha$ radius circles which contain the propagating wave modes.

This example highlights an important aspect of the PSF range migration when

---

[1] A common method for increasing Fourier-domain sampling known as zero-padding can be applied, but it requires specific apodization filters and considerations for the behaviour of the PSF at the boundary of the aperture.

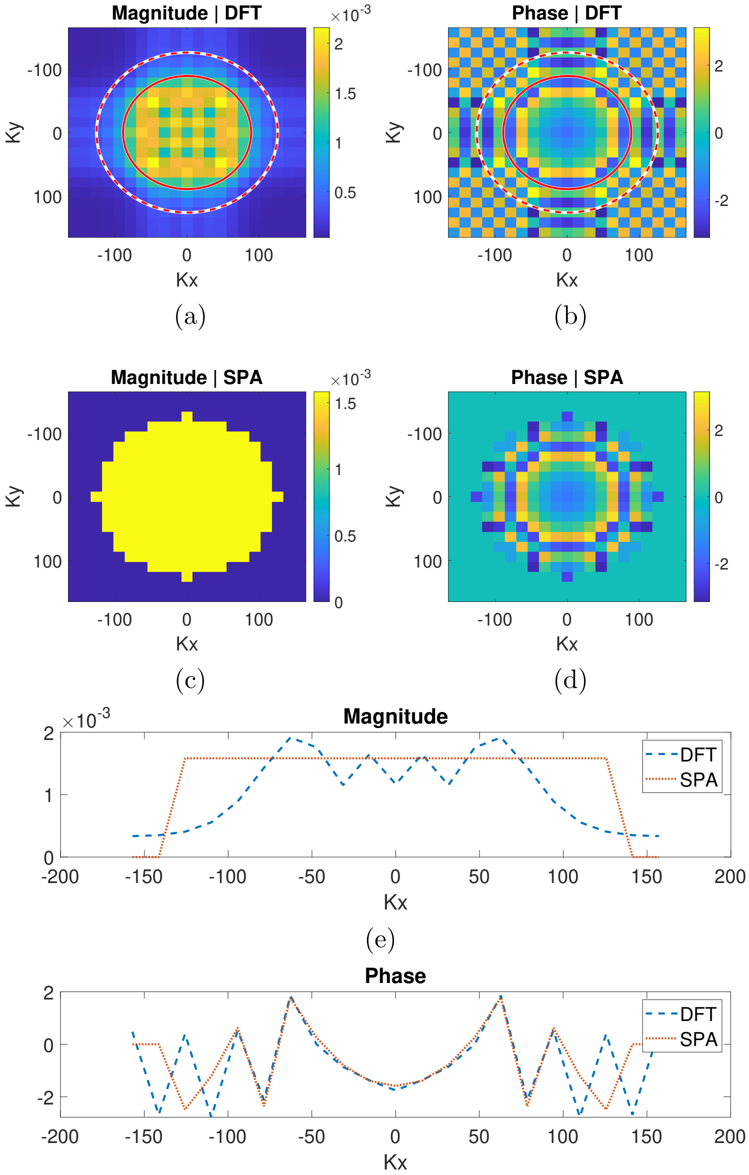

(a) (b)

(c) (d)

(e)

(f)

Figure 5.3: Fourier-domain counterpart of the monostatic kernel function (5.5) sampled on a 0.4×0.4 m^2 aperture with a probe positioned at $z = 0.2$ m from the aperture (maximum viewing angle $\alpha = 45°$) and a probe positioned at $z = 0.2$ m: (a) magnitude and (b) phase of the DFT of (5.5), (c) magnitude and (d) phase of the SPA solution (5.21), (e) magnitude and (f) phase 1D plots at $k_y = 0$ of the DFT and SPA approaches. Circles are drawn at the $2k$ radius boundary and the aperture-limited $2k_\alpha$ boundary to highlight how the change in aperture size affects the approximation.

the fixed-size aperture does not ensure large viewing angles. In the case where the probe is close to the aperture, the maximum viewing angle approaches 90°, and thus $2k_\alpha \approx 2k$. However, as the probe is shifted further from the aperture, the maximum viewing angle decreases, and thus the region containing the propagating modes shrinks. This observation is important in close-range imaging with measured PSFs. When a measured PSF is refocused from a further to a closer position (relative to the aperture), due to an increasing viewing angle, information beyond the $2k_\alpha$ boundary is required but is not available. This suggests that the initial probe location, at which the system PSF is measured, should be selected to maximize the viewing angle (the closest range location) and thus maximize the propagation-mode information within the $2k$-radius region.

5.3 Results

5.3.1 Simulation

An imaging experiment is simulated using the FEKO full-wave EM simulator [33]. Five half-lambda dipole antennas are positioned 10 mm apart in an 'X' configuration (see Fig. 5.4a), and perform a raster scan across a 60×60 mm^2 aperture in 2 mm increments. A frequency sweep is performed from 25 GHz to 40 GHz in 1 GHz increments, capturing 5 sets of monostatic measurements. The OUT comprises 3 structures, which can be seen in Fig. 5.4. Their permittivities are provided in the caption of Fig. 5.4. The background medium is vacuum.

To perform the reconstruction, the range migration factor in (5.24) is applied to the closest PSF measurement (probe at $z = 5$ mm) in order to refocus it to the slices

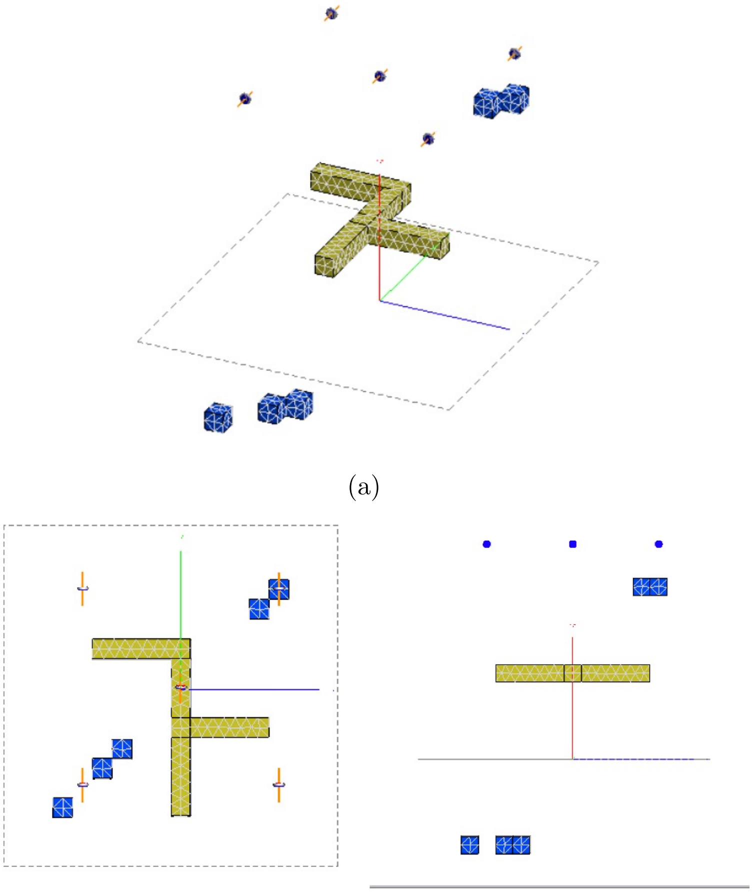

(a)

(b) (c)

Figure 5.4: Measurement setup and OUT structure in the simulated data acquisition: (a) isotropic view, (b) top view, and (c) side view. Background is vacuum. The permittivity values of the components are $\epsilon_r = 1.3$ for the large yellow structure, and $\epsilon_r = 1.5$ for the cuboidal structures (8 mm^3). Five half-lambda dipoles measure the scene independently through reflection coefficients. The components are positioned at three separate planes relative to the aperture: 5 mm, 15 mm, and 35 mm. Note that the components at the 5 mm range position are well within the near-field zone of the antennas when centered laterally.

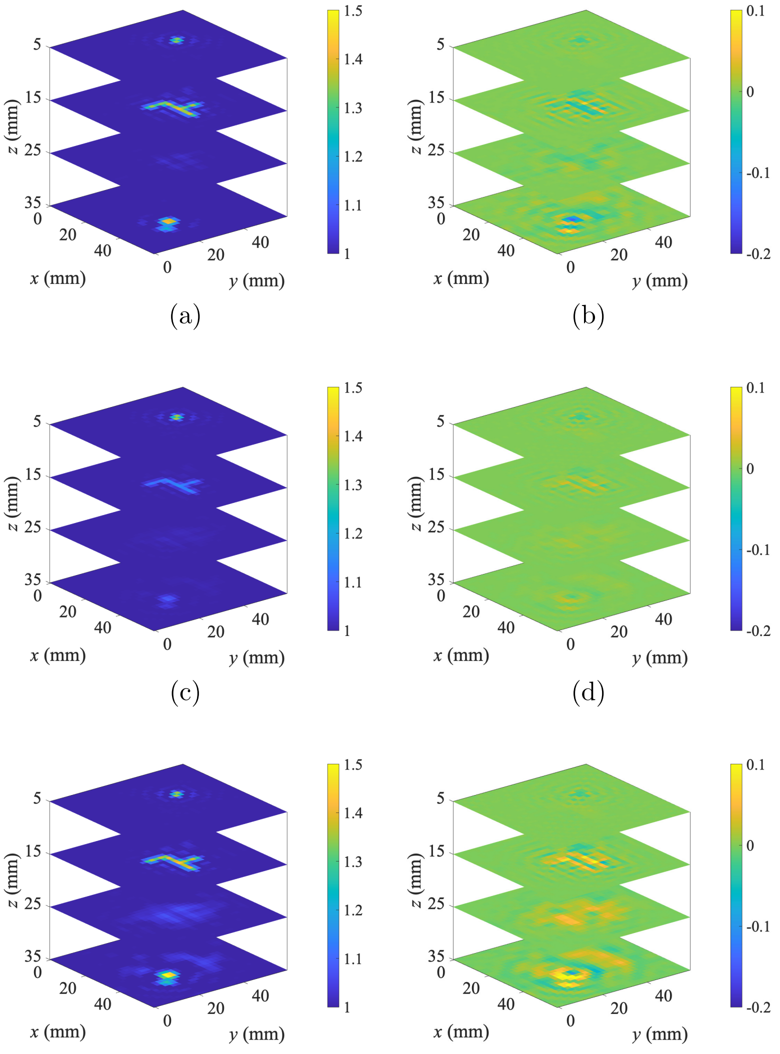

(a) (b)

(c) (d)

(e) (f)

Figure 5.5: QMH reconstructions of the simulated OUT shown in Fig. 5.4 using the combined Born/Rytov approach [9] : (a) real and (b) imaginary parts of the permittivity using measured PSFs at all slices, (c) real and (d) imaginary parts of the permittivity using a single measured PSF at $z = 5$ mm migrated to all other z positions with conventional plane wave migration (5.25), (e) real and (f) imaginary parts of the permittivity using a single measured PSF at $z = 5$ mm migrated to all other z positions with the proposed migration (5.24).

at $z = 15$ mm, $z = 25$ mm, and $z = 35$ mm. A 0.5 mm^3 probe of permittivity $\epsilon_r = 1.5$ was used for this calibration object (CO) measurement. After the range migration of the PSF, an 8th-order Butterworth low-pass filter is applied in the Fourier domain to restrict the spectrum to the region accessible within the viewing angle of the aperture (5.26). The data is then supplied to the combined Born/Rytov QMH algorithm [9]. After inversion, a low-pass 16th order Butterworth filter is applied in the Fourier domain at each range slice, and has a 20 dB cutoff set to the diffraction limit as defined by (5.26).

The resultant reconstructions can be seen in Fig. 5.5. The quantitative estimates of both the large central object and the small cubicles are reasonably accurate when using four measured PSFs (see Figs. 5.5a and 5.5b) as well as the SPA-based range migration (see Figs. 5.5e and 5.5f). As a clarifying note, the quantitative estimates with QMH (a direct reconstruction method which employs a linearized scattering model) are better with low-contrast objects but may deteriorate if high-contrast electrically large objects are present. Fig. 5.5 confirms that the quantitative accuracy is better with the SPA migration approach (5.24) as compared to the conventional angular spectrum representation (5.25) (see Figs. 5.5c and 5.5d).

The two closely spaced probes ($\epsilon_r = 1.5$) in the $z = 5$ mm plane are barely distinguishable from each other. Using the far-field monostatic radar resolution with $\alpha_{\max} = 80.54°$ [13]

$$\Delta\xi = \frac{\lambda_{\min}}{4\sin\alpha_{\max}} \approx 2 \text{ mm}, \; \xi \equiv x, y \tag{5.27}$$

which is exactly the size of these probes, and the sampling step in the acquisition. Their estimated real permittivity is 1.345 in the range migration approach and 1.33 in the measured PSF approach (see Fig. 5.6). The larger object at $z = 15$ mm is

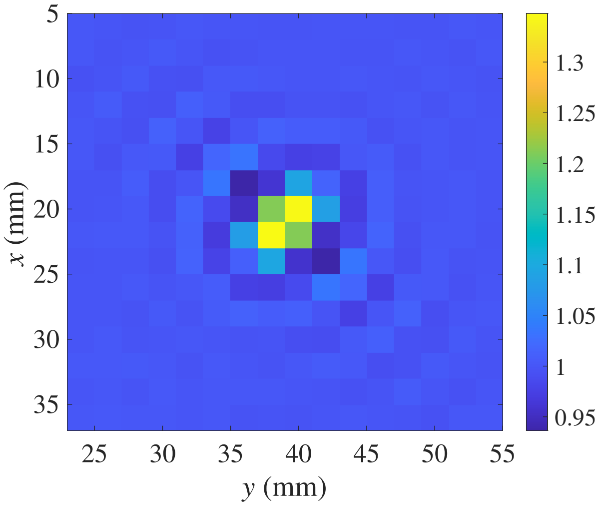

Figure 5.6: Enlarged image of the $z = 5$ mm layer from Fig. 5.5e, focusing on the two small probes. The probes, although placed directly side-by-side, can be individually identified.

structurally identified in both approaches, and has an average real permittivity of 1.361 in the range migration approach and 1.327 in the measured PSF approach. The furthest components at $z = 35$ mm highlight the impact of the diffraction limit, which shows the two cubes in contact as one larger cube of higher permittivity, and the isolated cube as a lower permittivity, larger cube structure.

5.3.2 Experiment

To further validate the approach, a planar raster scanning chamber is configured with a WR-28 horn antenna [34]. The antenna is connected to an Agilent E8363B vector network analyzer capturing S_{11} data from 26 GHz to 40 GHz in 100 MHz increments. While the antenna remains fixed, the platform carrying the imaging target shifts in 2 mm increments across a 30 cm by 30 cm aperture. The antenna is positioned approximately 5 mm above measured objects. The platform is still when measurements are acquired. Overall, there are 151 (x) by 151 (y) by 141 (ω) data points per measurement.

The measured object is a stack of four 0.5 inch (12.7 mm) thick *Styrofoam* sheets with an average estimated permittivity of $\epsilon_r \approx 1.175 - \mathrm{i}0$ across the frequency of interest. Several items are placed at different locations in the image volume. Two crosses, one made of carbon rubber and the other ceramic, are positioned in layers 1 and 3 of the stack-up (see Fig. 5.7). Their permittivity values can be found in Table 5.1. These values are determined either via measurement with a dielectric probe or taken from reference [35]. Note that the actual permittivity of the components that have been starred (*) are expected to be larger than the measured value due to the inability to carry out accurate measurements with a slim-form probe [36]. This probe requires 5 mm of penetration to provide an accurate measurement result. In layers 2 and 4, a series of small targets (2.4 mm diameter *Nylon* balls and $3 \times 2.6 \times 2$ mm^3 carbon rubber prisms) are positioned laterally in pairs, each separated (edge-to-edge) by either 8 mm, 4 mm, or 2 mm. By doing so, we can evaluate the image resolution of the system relative to the shortest wavelength (7.5 mm at 40 GHz).

A series of PSF measurements are also performed on calibration objects (COs), which consist of a small scattering probe (SP) embedded in a *Styrofoam* sheet. One of the carbon rubber prisms serves as a scattering probe ($3 \times 2.6 \times 2$ mm^3, $\epsilon_r \approx 7.85 - \mathrm{i}3.01$). The probe is centered laterally and is positioned at the top-most portion of each layer formed by a *Styrofoam* sheet. Note that this probe position is offset along range with respect to the cross-shaped components, which are vertically centered within the *Styrofoam* sheet.

To validate the proposed PSF range migration approach, the PSF measured at

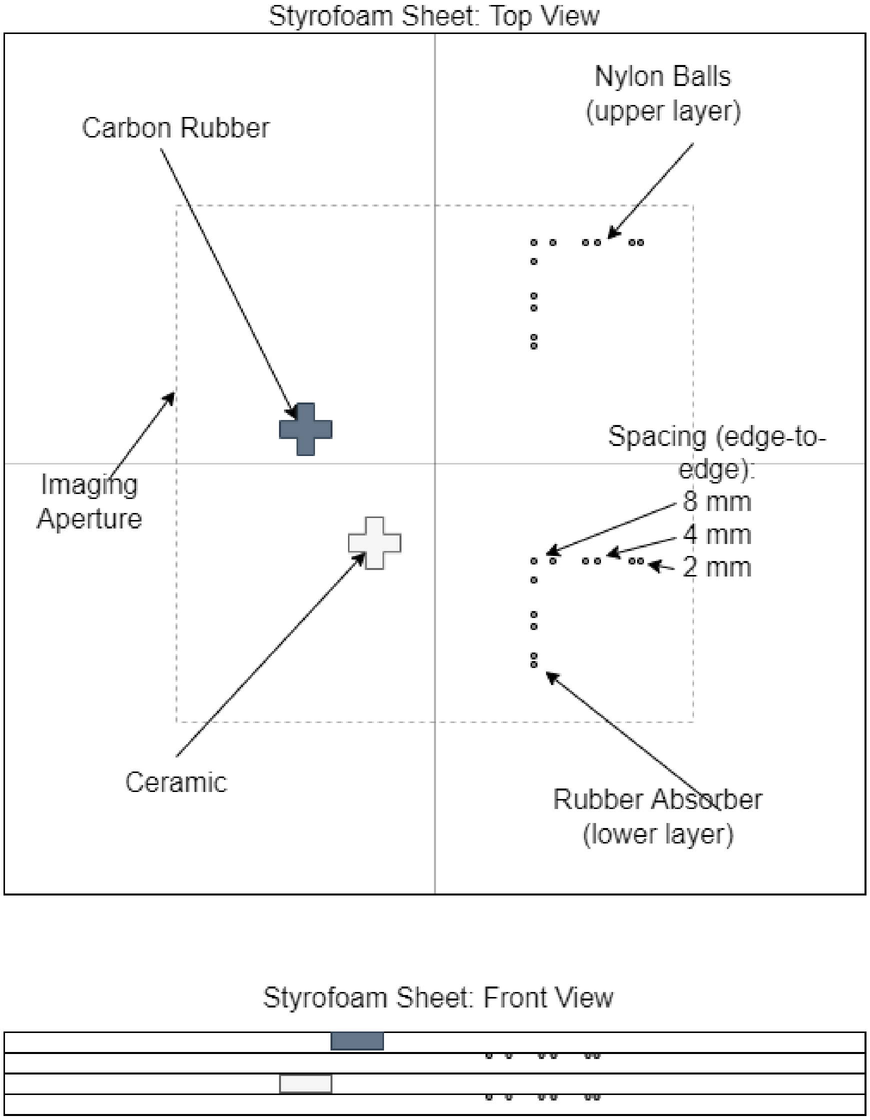

Figure 5.7: Image of the OUT, containing the two crosses made of carbon rubber (Layer 1) and microwave ceramics (Layer 3), and the two arrays of scattering probes, made of 2.4 mm diameter *Nylon* balls (in Layer 2), and $3 \times 2.6 \times 2\ \text{mm}^3$ carbon-rubber material (Layer 4)

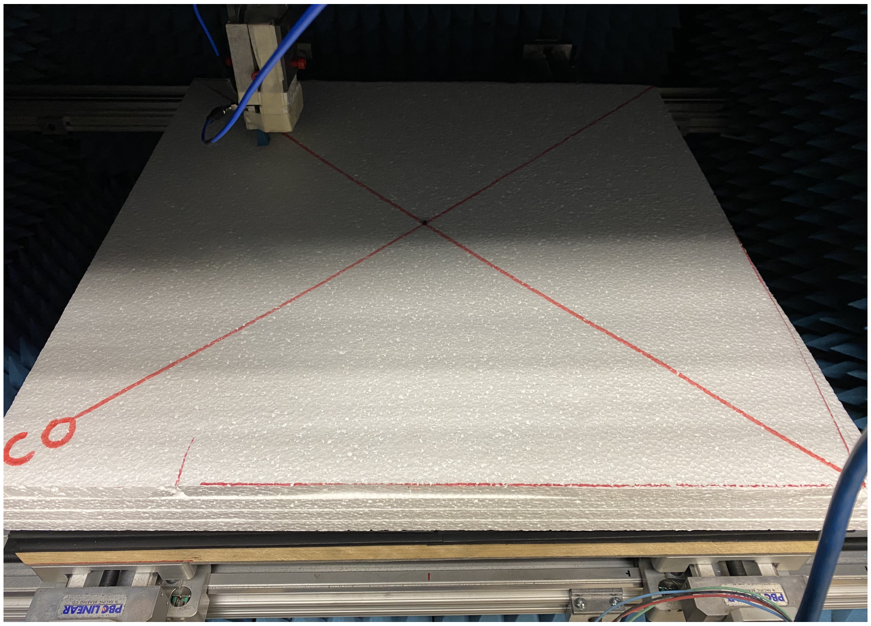

Figure 5.8: Photo of the acquisition chamber and the CO object. The WR-28 horn is visible in the top left corner of the image. The platform shifts in a raster-scanning fashion while the antenna remains fixed.

the plane closest to the antenna is refocused to all other desired range slices for image reconstruction. For comparison, this is repeated for the standard plane-wave range translation. The results are summarized in Fig. 5.9 and Fig. 5.10.

In the results using only measured PSFs (Fig. 5.9), the images have good structural accuracy, i.e., the item's position and shape are reconstructed well. "Bleeding" artifacts occur throughout the image, due to both the large size and permittivity contrast of the cross-shaped components, as well as the misalignment with the PSF probe positioning in the CO measurements. The quantitative accuracy is low, especially in the regions occupied by the two cross-shaped components, which are not only high-contrast but also they are not electrically small. The top-most carbon-rubber cross is reconstructed with some nonphysical (positive) imaginary permittivity values

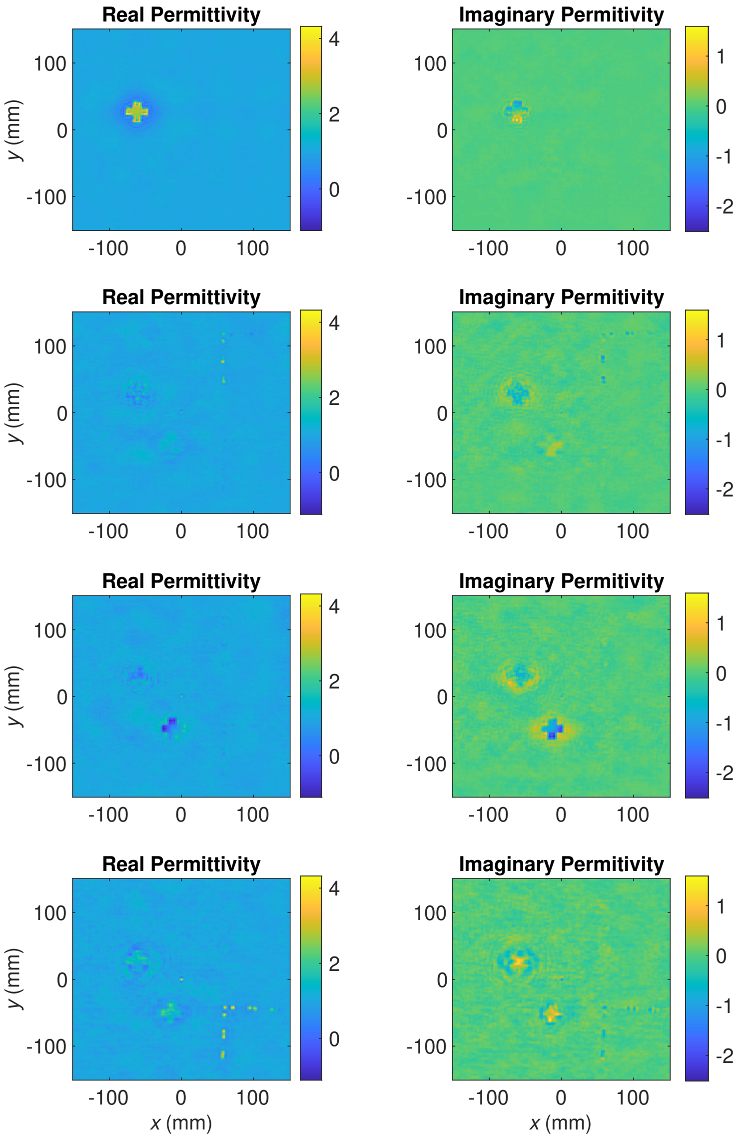

Figure 5.9: QMH reconstructions of the simulated OUT shown in Fig. 5.4 using the combined Born/Rytov approach [9]. To reconstruct the images, four PSF measurements are performed with the scattering probe at the four desired range slices ($z = 5, 17.7, 30.4, 43.1$ mm). Each row shows plots of the real and imaginary parts of the OUT relative permittivity at a range slice: from $z = 5$ mm (top) to $z = 43.1$ mm (bottom).

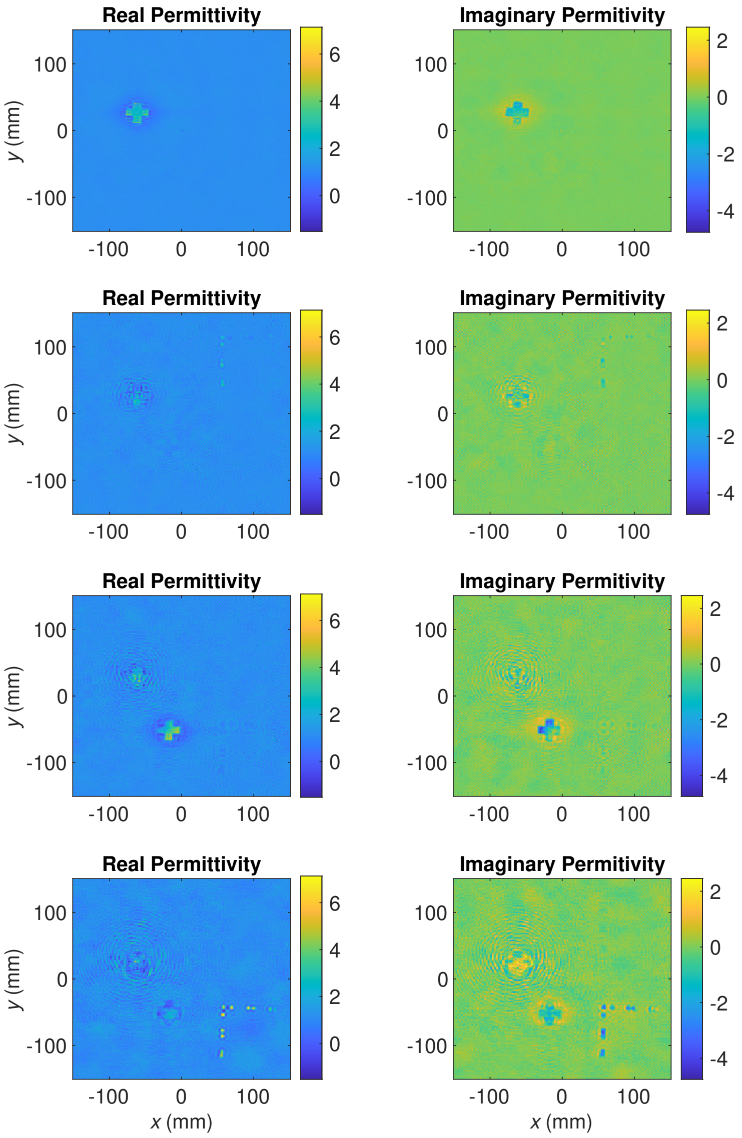

Figure 5.10: QMH reconstructions of the simulated OUT shown in Fig. 5.4 using the combined Born/Rytov approach [9]. To reconstruct the images, a single PSF measurement is performed with the scattering probe at $z = 5$ mm. The measured PSF is then migrated to $z = 4.5, 16.0, 32.0, 42.6$ mm. Each row shows plots of the real and imaginary parts of the OUT relative permittivity at a range slice: from $z = 4.5$ mm (top) to $z = 42.6$ mm (bottom).

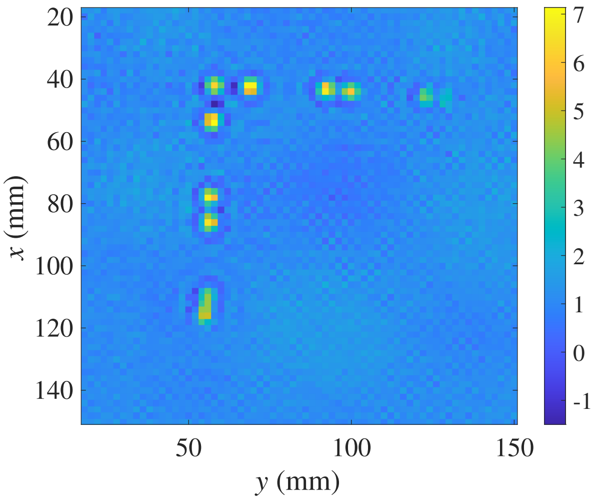

Figure 5.11: Enlarged real-part of the permittivity of the $z = 42.6$ mm layer from Fig. 5.10, focusing on the array of carbon rubber probes. The probes hardest to individually identify are the probes separated by $\approx \lambda_{\text{min}}/4$. The probes separated by $\approx \lambda_{\text{min}}$ and $\approx \lambda_{\text{min}}/2$ are distinguishable.

whereas the reconstructed ceramic cross in layer 3 has a negative real-part of the permittivity. Such errors are expected because of the linearizing approximation of the forward model [13]. The smaller probes (*Nylon* balls in layer 2 and thin rubber prisms in layer 4) are reconstructed at accurate range locations with reasonable permittivity estimates.

Now consider the results generated using the range migration algorithm with a single measured PSF ($z = 4.5$ mm), shown in Fig. 5.10. Since the range migration allows for the PSF to be migrated to any position, slight adjustments are made to the PSF for layer 3 to align it with the cross item. While the bleeding artifacts of the crosses are still present, the cross property estimation has improved and the nonphysical permittivity values have decreased. Interestingly, this result appears to suggest that the ceramic cross has significant loss, which has not been found in the material permittivity estimated through the dielectric probe measurement. Note also

Table 5.1: Averaged Dielectric Properties of Phantom Materials from 26 GHz to 40 GHz

Material (Structure)	ϵ'	ϵ''
Styrofoam	1.18	0.00
Nylon Ball [37]	3.05	0.03
Carbon Rubber Cross[1]	8.49	0.93
Ceramic Cross[1]	4.48	0.44
Carbon Rubber Scattering Probe[1]	7.85	3.01

that the permittivity of both cross-shaped components appears to change across the surface of the object, which may be due to the different leveling with respect to the aperture plane.

The comparison of the images in Fig. 5.9 and Fig. 5.10 suggests that the spatial resolution is not impacted by the replacement of the measured PSFs with migrated ones. The smallest probe spacing is 2 mm in layers 2 and 4, which was chosen to be close to $\lambda_{\min}/4 \approx 1.874$ mm, where $\lambda_{\min}$ is the shortest wavelength (at 40 GHz). Using (5.27), the viewing-angle limited resolution can also be determined. Here, α is limited by the beamwidth of the horn antenna which is $\approx 54^\circ$ [34], which would imply a resolution of 2.47 mm. Thus, the difficulty in distinguishing the close proximity probes in layers 2 and 4 is expected. The real-permittivity slice image in Fig. 5.11 shows an enlarged section where the small probes reside in the layer $z = 42.6$ mm. It is observed that the image resolution is worse than $\lambda_{\min}/4$. However, the probes separated by distances of $\lambda_{\min}/2$ and $\lambda_{\min}$ are distinguished very well.

---

[1] These properties are underestimated due to the inability to properly measure them with the available dielectric measurement probe [36]. Documentation on the dielectric properties of these materials is not available above 20 GHz.

5.4 Conclusions

In this work, a new formulation of range migration is derived with the stationary phase approximation for the case of monostatic measurements. The range migration is performed directly in Fourier domain. Compared to previous range-migration strategies, which adjust only the phase of the scattering kernel, this formulation has better accuracy, especially in near-field and close-range imaging scenarios, where the aperture size is much larger than the range distance to the target and the 3D range resolution is in the same order of magnitude as the range distance to the target. The result is analytical and it does not increase the computational requirements of the Fourier-based image reconstruction algorithms.

The impact of the aperture size is also investigated with account for the maximum viewing angle of the imaging setup. The results indicate that the best strategy for range migration of a measured PSF is to first acquire the PSF with a scattering probe at the closest range position relative to the antenna(s) and then migrate away to all other desired range position.

Both simulation and experimental examples using the QMH image-reconstruction algorithm demonstrate the image quality improvement when compared to the plane-wave migration approach. Most importantly, the accurate range-migration strategy allows for taking full advantage of measured PSFs with significantly reduced calibration effort. This is due to the reduction of the number of PSF measurement from N_z (the number of imaged slices in a 3D image) to just one.

Future work will expand this study to bistatic radar. Also, the efficacy of the proposed technique will be validated with other quantitative Fourier-based imaging algorithms, e.g., [29].

REFERENCES

[1] D. J. Daniels, *Ground Penetrating Radar.* IET, 2004, vol. 1.

[2] M. Grasmueck, R. Weger, and H. Horstmeyer, "Full-resolution 3D GPR imaging," *Geophysics*, vol. 70, pp. K12–K19, Jan. 2005.

[3] C. Gilmore, I. Jeffrey, and J. LoVetri, "Derivation and comparison of SAR and frequency-wavenumber migration within a common inverse scalar wave problem formulation," *IEEE Trans. Geosci. Remote Sens.*, vol. 44, no. 6, pp. 1454–1461, Jun. 2006.

[4] Z. Li, J. Wang, and Q. H. Liu, "Interpolation-free Stolt mapping for SAR imaging," *IEEE Geosci. Remote Sens. Lett.*, vol. 11, no. 5, pp. 926–929, Oct. 2014.

[5] L. Merabet, S. Robert, and C. Prada, "2-D and 3-D reconstruction algorithms in the Fourier domain for plane-wave imaging in nondestructive testing," *IEEE Trans. Ultrason., Ferroelectr., Freq. Control*, vol. 66, no. 4, pp. 772–788, Jan. 2019.

[6] J. W. Goodman, *Introduction to Fourier Optics.* New York, USA: McGraw-Hill, 1996.

[7] M. Soumekh, *Fourier Array Imaging.* NJ, United States: Prentice-Hall, 1994.

[8] Y. Meng, C. Lin, J. Zang, A. Qing, and N. K. Nikolova, "General theory of holographic inversion with linear frequency modulation radar and its application to whole-body security scanning," *IEEE Trans. Microw. Theory Techn.*, vol. 68, no. 11, pp. 4694–4705, Aug. 2020.

[9] D. Tajik, R. Kazemivala, and N. K. Nikolova, "Real-time imaging with simultaneous use of Born and Rytov approximations in quantitative microwave holography," *IEEE Trans. Microw. Theory Techn.*, pp. 1–14, Dec. 2021.

[10] R. K. Amineh, J. J. McCombe, A. Khalatpour, and N. K. Nikolova, "Microwave holography using measured point-spread functions," *IEEE Trans. Instrum. Meas.*, vol. 64, no. 2, pp. 403–417, Feb. 2015.

[11] A. Eid, J. Zhu, L. Xu, J. G. D. Hester, and M. M. Tentzeris, "Holography-based target localization and health monitoring technique using UHF tags array," *IEEE Internet Things J.*, vol. 8, no. 19, pp. 14 719–14 730, Apr. 2021.

[12] D. Gabor, "A new microscopic principle," *Nature*, no. 666, pp. 777–778, May 1948.

[13] N. K. Nikolova, *Introduction to Microwave Imaging.* Cambridge, United Kingdom: Springer Science & Business Media, 2017.

[14] C. Özdemir, Şevket Demirci, E. Yiğit, and B. Yilmaz1, "A review on migration methods in B-scan ground penetrating radar imaging," *Math. Probl. Eng.*, vol. 2014, pp. 772–788, Jun. 2014.

[15] J. M. Lopez-Sanchez and J. Fortuny-Guasch, "3-d radar imaging using range migration techniques," *IEEE Trans. Antennas Propag.*, vol. 48, no. 5, pp. 728–737, 2000.

[16] X. Zhuge and A. G. Yarovoy, "Three-dimensional near-field mimo array imaging using range migration techniques," *IEEE Trans. Image Processing*, vol. 21, no. 6, pp. 3026–3033, 2012.

[17] L. Pulido-Mancera, T. Fromenteze, T. Sleasman, M. Boyarsky, M. F. Imani, M. Reynolds, and D. Smith, "Application of range migration algorithms to imaging with a dynamic metasurface antenna," *J. Opt. Soc. Am. B*, vol. 33, no. 10, pp. 2082–2092, Oct. 2016. [Online]. Available: http://www.osapublishing.org/josab/abstract.cfm?URI=josab-33-10-2082

[18] F. Uysal, "Comparison of range migration correction algorithms for range-Doppler processing," *J. Appl. Remote Sens.*, vol. 11, no. 3, pp. 1 – 10, Sep. 2017. [Online]. Available: https://doi.org/10.1117/1.JRS.11.036023

[19] R. H. Stolt, "Migration by Fourier transform," *Geophysics*, vol. 1, no. 63, p. 23–48, Feb. 1978.

[20] C. Cafforio, C. Prati, and F. Rocca, "SAR data focusing using seismic migration techniques," *IEEE Trans. Aerosp. Electron. Syst.*, vol. 27, no. 2, pp. 194–207, Mar. 1991.

[21] R. Bamler, "A comparison of range-Doppler and wavenumber domain SAR focusing algorithms," *IEEE Trans. Geosci. Remote Sens.*, vol. 30, no. 4, pp. 706–713, Jul. 1992.

[22] M. Soumekh, "Range stacking: an interpolation-free sar reconstruction algorithm," in *Algorithms for Synthetic Aperture Radar Imagery V*, vol. 3370. SPIE, 1998, pp. 13–24.

[23] W. Tan, P. Huang, Z. Huang, Y. Qi, and W. Wang, "Three-dimensional microwave imaging for concealed weapon detection using range stacking technique," *Int. J. Antennas Propag.*, vol. 2017, 2017.

[24] S. Li, G. Zhao, H. Sun, and M. Amin, "Compressive sensing imaging of 3-d object by a holographic algorithm," *IEEE Trans. Antennas Propag.*, vol. 66, no. 12, pp. 7295–7304, 2018.

[25] Y. Meng, C. Lin, A. Qing, and N. K. Nikolova, "Accelerated holographic imaging with range stacking for linear frequency modulation radar," *IEEE Trans. Microw. Theory Tech.*, vol. early access, 2021.

[26] A. S. Beaverstone, D. S. Shumakov, and N. K. Nikolova, "Integral equations of scattering for scalar frequency-domain responses," *IEEE Trans. Microw. Theory Techn.*, vol. 64, no. 4, pp. 1120–1132, Apr. 2015.

[27] D. Sheen, D. McMakin, and T. Hall, "Near-field three-dimensional radar imaging techniques and applications," *Appl. Opt.*, vol. 49, no. 19, pp. E83–E93, Jun. 2010.

[28] D. Tajik, F. Foroutan, D. S. Shumakov, A. D. Pitcher, and N. K. Nikolova, "Real-time microwave imaging of a compressed breast phantom with planar scanning," *IEEE J. Electromagn., RF, Microw. Med. Biol.*, vol. 2, no. 3, pp. 154–162, Sep. 2018.

[29] D. S. Shumakov and N. K. Nikolova, "Fast quantitative microwave imaging with scattered-power maps," *IEEE Trans. Microw. Theory Techn.*, vol. 66, no. 1, pp. 439–449, Jan. 2018.

[30] D. Tajik, R. Kazemivala, and N. K. Nikolova, "Point-spread functions in inverse scattering and image reconstruction with microwaves and millimeter waves," in *Electromagnetic Waves and Antennas for Biomedical Applications*, L. Wang, Ed.

London, England: Institute of Engineering and Technology, 2022, ch. 1, pp. 1 – 46.

[31] D. Tajik, A. D. Pitcher, and N. K. Nikolova, “Comparative study of the Rytov and Born approximations in quantitative microwave holography,” *Prog. Electromagn. Res. B*, vol. 79, pp. 1–19, Jan. 2017.

[32] S. J. Orfanidis, *Electromagnetic Waves and Antennas.* Rutgers University, 2015, vol. 1.

[33] Altiar FEKO, Electromagnetic Simulation Software. [Online]. Available: https://altairhyperworks.com/product/FEKO

[34] “WR-28 waveguide standard gain horn antenna operating from 26.5 GHz to 40 GHz with a nominal 10 dBi gain with UG-599/U square cover flange,” https://www.pasternack.com/standard-gain-horn-waveguide-size-wr28-pe9850-10-p.aspx, Accessed: 2022-02-24.

[35] M. N. Afsar, “Precision millimeter-wave measurements of complex refractive index, complex dielectric permittivity, and loss tangent of common polymers,” *IEEE Trans. Instrum. Meas.*, vol. IM-36, no. 2, pp. 530–536, 1987.

[36] “N1501A Dielectric Probe Kit,” https://www.keysight.com/ca/en/assets/7018-04631/technical-overviews/5992-0264.pdf, Accessed: 2022-02-24.

[37] N. Reyes, F. Casado, and V. T. *et al*, “Complex dielectric permittivity of engineering and 3D-printing polymers at Q-band,” *J. Infrared Milli. Terahz. Waves*, vol. 39, 2018.

CHAPTER 6

CONCLUSIONS

6.1 Summary

In this work, microwave imaging algorithms are developed and enhanced via: (a) experimental evaluations using compressed breast phantoms, (b) quality control techniques guaranteeing sufficient contrast-to-noise ratios for image processing, (c) improved use of the Born and Rytov linear approximations to enhance detection of embedded targets, and (d) range focusing techniques to reduce calibration time and provide range sampling flexibility [1–3]. All developments are supported by both simulated and experimental studies, which is critical for any technology attempting to reach clinical trials. While this work focuses primarily on planar scanning, it can be easily modified to accommodate cylindrical and hemispherical scanning apertures that are seeing more widespread use in microwave breast imaging [4]. The following discussion highlights future work for each chapter.

6.2 Future Work

6.2.1 Improved Design of Acquisition System

In several of the published works, high output power was required to achieve sufficient contrast-to-noise ratio (CNR) in the point-spread functions (PSF). However, the selection of output power does not reflect what is required for clinical circumstances which must adhere to the Canada Safety Code 6 (or equivalent) requirements [5]. This is particularly true in the case of the work in Chapter 4, which utilizes 8 W of transmit power in order to generate sufficient signal quality, with scan time that is in excess of 5 hours [3]. Future work should improve the acquisition setup so that it does not require such substantial output power. It was shown in Chapter 2 that with a realistic scan time of several minutes, 3 W of power would not exceed the 8 W/kg requirement for controlled environments. Indeed, achieving a power output of 1 W (a 9 dB decrease from Chapter 4), should be manageable and be set as a requirement for future experimental evaluations. Improvements to the acquisition system, including the further addition of shielding absorbers and non-reflective platform designs could substantially reduce the background clutter and help achieve this goal.

6.2.2 Improving Phantom Design for Compressed Breast Imaging

The work in [1] relied on layered phantom material to construct a compressed breast phantom, which does not correlate well with substantially heterogeneous breast tissue. Future developments of compressed breast phantoms should utilize more heterogeneous tissue structures. Several Canadian teams have found success in their own custom phantom design [6–8], utilizing oil and gelatin combinations to match the dielectric properties of tissues, with some using 3D printed materials to match closely the physical structure of specific tumors. These phantoms typically have limited shelf-lives as their moisture content changes over time, requiring new phantoms to be regularly built. Other teams utilize carbon rubber phantom structures that have longer shelf-lives, but are more challenging to manufacture and cannot be further customized post-construction [9,10]. It would be worthwhile to pursue both phantom styles for compressed breast structures, which would in-turn push the imaging algorithms discussed in this work toward clinical trials.

6.2.3 Additional Quality Control Techniques for Microwave Acquisition Systems

Quality control remains a challenging and unresolved aspect of microwave imaging [2,10,11]. Due to the variety of configurations of microwave hardware relating to antenna aperture shape, antenna type, and the baseline image processing algorithm, a variety of performance metrics can be generated which may only satisfy the evaluation of specific hardware configurations. These unique characteristics make comparisons between different prototypes challenging, and cause divergence in hardware research development. A push should be made to create common image quality metrics that can be used to evaluate the performance of microwave imaging hardware. This would enable the identification of optimal hardware implementation and thus focusing research effort on optimal configurations, as well as provide a beneficial tool to engineers who are debugging/optimizing their hardware. Metrics from MRI and other imaging modalities can be immediately borrowed to perform this [12–14]. In particular, lateral resolution evaluation can yield important information on weaknesses of the acquisition system in a given direction. A good example of this quality control evaluation can be found in [15], which utilizes a series of horizontal and diagonal metal stripes as a ‘benchmark target’ to evaluate their imaging system and associated holography algorithm. Other QA approaches used in MRI such as image uniformity should also be explored, especially for maintenance purposes. Image uniformity studies the acquisition setup itself, which in the case of this thesis would involve analysis of the variance on the RO measurement.

6.2.4 Enhanced Image Reconstruction by Use of Iterative Imaging Techniques

Though results in Chapter 4, as well as in [3, 16], show that combining the Born and Rytov approximations can yield increased image quality, further work is needed. Algorithms that can rely on this combination still struggle with nonphysical permittivities that are generated due to use of a linearized model being applied to a nonlinear scattering problem. The main resolution to this problem is the implementation of iterative algorithms, which utilize nonlinear models of scattering via repeated updating of internal parameters. However, conventional iterative algorithms rely on full-wave EM simulators which add substantial computational load and can introduce modelling errors that lead to image degradation [17–19]. Modelling errors are not related to numerical accuracy but instead involve the inability to account for all acquisition-specific factors that can influence a measurement. Examples include cables, vibrations during measurement, and positioning inaccuracy. Thus, conventional iterative algorithms such as the Born iterative and distorted Born iterative methods may not provide the most practical solution [17, 18].

However, the algorithms discussed in this thesis (quantitative microwave holography and scattered-power mapping) can be further explored and transformed into iterative algorithms by using them as a module within an iterative procedure. One can either use QMH and SPM as: (a) an initial guess that can be used to accelerate a conventional iterative algorithm that typically start with an assumed uniform background or (b) perform repeated computations of QMH or SPM, updating the resolvent kernel (i.e. the total internal electric field) before each iteration based on the new permittivity estimate [20]. This approach would take advantage of the speed of the QMH and SPM methods, avoid the modelling errors associated with EM solvers, and account for the complex scattering effects that contribute to significant errors and artifacts generated using the linear models of scattering alone.

6.2.5 Prototypes for Planar Scanning

This thesis focuses primarily on the development of imaging algorithms for use in biomedical imaging, yet highlighted in Chapter 1 is the need for pairing algorithms with specific hardware implementation to avoid modelling errors. Although experimental examples were provided throughout this thesis, these experiments relied on a slow raster scanning acquisition system, which utilizes a limited number of antennas (2-8) and takes hours to complete a single measurement. In order to achieve any success in biomedical imaging for breast cancer applications, imaging hardware must be able to perform all necessary measurements within several minutes, limiting the RF exposure to the patient as well as reducing their overall discomfort. It is clear that this is achievable given the success of other microwave imaging prototypes currently undergoing clinical trials around the world [21–23]. Work at McMaster University has begun in this area, and the development of a planar active receive antenna array has been demonstrated with a dynamic range of 118 dB [24–26]. Future developments will involve a custom-designed transmit array with switching capabilities for each element, and an integrated radio that will allow for synchronization between the transmit and receive stages. This development is critical as it transforms the imaging system into a vector-network analyzer, and thus directly integrates with the QMH and SPM algorithms that rely on S-parameter measurements.

6.2.6 Final Remarks

Microwave imaging for biomedical applications is an exciting area of research that continues to develop as new low-cost high-frequency components become available. Though some may doubt the effectiveness of microwave imaging for breast cancer applications considering its prolonged exploration with limited success, the work of this thesis as well as recent prototypes demonstrates the value of pursuing this research area [21–23]. I envision a measurement system which could be placed inside a general practitioners office, with a simple bed-like profile, automatically perform its calibration and detection without the need of a radiologist. This lack of radiologist can be achieved with advances in machine learning techniques, benefiting from the quantitative diagnostic values generated by my proposed methods. Patient data would also be stored, allowing for health monitoring and longitudinal studies which may further improve the mortality rates with respect to breast cancer.

However, the hope for this research is to go beyond breast cancer detection into other areas of biomedical imaging. If microwave imaging technology can be proven to operate at low-cost and with minimal inconvenience to the patient, other diagnostic areas such as brain-stroke detection and skin-cancer detection may be able to leverage this success. Also, pairing microwave technology with other imaging modalities creates the possibility of image fusion. Image fusion is a technique already showing great success in PET/CT imaging by combining complementary traits of each technology to create higher fidelity images. With these benefits in mind, microwave imaging technology has come a long way since its original inception in the 1960s, and will continue to enhance the lives and well-being of humanity for years to come.

REFERENCES

[1] D. Tajik, F. Foroutan, D. S. Shumakov, A. D. Pitcher, and N. K. Nikolova, “Real-time microwave imaging of a compressed breast phantom with planar scanning,” *IEEE J. Electromagn., RF, Microw. Med. Biol.*, vol. 2, pp. 154–162, Sep. 2018.

[2] D. Tajik, J. Trac, and N. K. Nikolova, “Quality control of microwave equipment for tissue imaging,” *IEEE J. Electromagn., RF, Microw. Med. Biol.*, vol. 4, pp. 52–60, Mar. 2019.

[3] D. Tajik, R. Kazemivala, and N. K. Nikolova, “Real-time imaging with simultaneous use of Born and Rytov approximations in quantitative microwave holography,” *IEEE Trans. Microw. Theory Techn.*, pp. 1–14, Dec. 2021.

[4] D. O’Loughlin, M. O’Halloran, B. M. Moloney, M. Glavin, E. Jones, and M. A. Elahi, “Microwave breast imaging: Clinical advances and remaining challenges,” *IEEE Trans. Biomed. Eng.*, vol. 65, pp. 2580–2590, Nov. 2018.

[5] *Limits of human exposure to radiofrequency electromagnetic energy in the frequency range from 3 KHz to 300 GHz.* Health Canada, 2015.

[6] E. Porter, J. Fakhoury, R. Oprisor, M. Coates, and M. Popović, “Improved tissue phantoms for experimental validation of microwave breast cancer detection,” in *4th Eur. Conf. Antennas Propag. EuCAP*, pp. 1–5, IEEE, Apr. 2010.

[7] T. Reimer, J. Krenkevich, and S. Pistorius, “An open-access experimental dataset for breast microwave imaging,” in *14th Euro. Conf. Antennas Propag.*, pp. 1–5, Mar. 2020.

[8] T. Reimer and S. Pistorius, “A quantitative analysis of the impact of glass as a phantom shell material in breast microwave sensing,” in *19th Int. Symp. Antenna Techn. Appl. Electromagn. (ANTEM)*, pp. 1–2, Aug. 2021.

[9] J. Garrett and E. Fear, “Stable and flexible materials to mimic the dielectric properties of human soft tissues,” *IEEE Antennas Wireless Propag. Lett.*, vol. 13, pp. 599–602, Mar. 2014.

[10] J. Moll, D. Wõrtge, V. Krozer, A. Santorelli, M. Popović, B. Bazrafshan, F. Hübner, T. J. Vogl, and N. Nikolova, “Quality control of carbon-rubber tissue phantoms: Comparative MRI, CT, X-ray and UWB microwave measurements,” in *11th European Conf. Antennas Propag. EuCAP*, pp. 2723–2727, Mar. 2017.

[11] D. Tajik, J. Trac, and N. K. Nikolova, “Spatial resolution evaluation of a microwave system for breast cancer screening,” in *13th Euro. Conf. Antennas Propag. EuCAP*, pp. 1–5, Jun. 2019.

[12] M. J. Firbank, R. M. Harrison, E. D. Williams, and A. Coulthard, “Quality assurance for MRI: practical experience.,” *British J. Radiol.*, vol. 73, no. 868, pp. 376–383, 2000. PMID: 10844863.

[13] R. R. Price, L. Axel, T. Morgan, R. Newman, W. Perman, N. Schneiders, M. Selikson, M. Wood, and S. R. Thomas, “Quality assurance methods and phantoms for magnetic resonance imaging: Report of AAPM nuclear magnetic resonance Task Group No. 1,” *Med. Phys*, vol. 17, pp. 287–295, Apr. 1990.

[14] R. T. Droege, “A quality assurance protocol for CT scanners,” *Radiol.*, pp. 244–246, Jan. 1983.

[15] Y. Meng, C. Lin, J. Zang, A. Qing, and N. K. Nikolova, "General theory of holographic inversion with linear frequency modulation radar and its application to whole-body security scanning," *IEEE Trans. Microw. Theory Techn.*, vol. 68, pp. 4694–4705, Aug. 2020.

[16] D. Tajik, N. K. Nikolova, and M. D. Noseworthy, "Improving quantitative microwave holography through simultaneous use of the Born and Rytov approximations," in *16th Euro. Radar Conf. EuRAD*, Nov. 2019.

[17] Y. M. Wang and W. C. Chew, "An iterative solution of the two-dimensional electromagnetic inverse scattering problem," *Int. J. Imag. Sys. Tech.*, vol. 1, no. 1, pp. 100–108, 1989.

[18] W. C. Chew and Y. M. Wang, "Reconstruction of two-dimensional permittivity distribution using the distorted Born iterative method," *IEEE Trans. Med. Imag.*, vol. 9, pp. 218–225, Jun. 1990.

[19] M. Ostadrahimi, P. Mojabi, C. Gilmore, A. Zakaria, S. Noghanian, S. Pistorius, and J. LoVetri, "Analysis of incident field modeling and incident/scattered field calibration techniques in microwave tomography," *IEEE Antennas Wireless Propag. Lett.*, vol. 10, pp. 900–903, Sep. 2011.

[20] N. K. Nikolova, *Introduction to Microwave Imaging.* Cambridge, United Kingdom: Springer Science & Business Media, 2017.

[21] P. Meaney, M. Fanning, D. Li, S. Poplack, and K. Paulsen, "A clinical prototype for active microwave imaging of the breast," *IEEE Trans. Microw. Theory Techn.*, vol. 48, pp. 1841–1853, Nov. 2000.

[22] B. M. Moloney, P. F. McAnena, S. M. Elwahab, A. Fasoula, L. Duchesne, J. D. Gil Cano, C. Glynn, A. O'Connell, R. Ennis, A. J. Lowery, *et al.*, "The Wavelia microwave breast imaging system–tumour discriminating features and their clinical usefulness," *Br. J. Radiol.*, vol. 94, p. 20210907, Oct. 2021.

[23] M. Adachi, T. Nakagawa, T. Fujioka, M. Mori, K. Kubota, G. Oda, and T. Kikkawa, "Feasibility of portable microwave imaging device for breast cancer detection," *Diagnostics*, vol. 12, Dec. 2022.

[24] F. Foroutan and N. K. Nikolova, "Active sensor for microwave tissue imaging with bias-switched arrays," *Sensors*, vol. 18, p. 1447, May 2018.

[25] F. Foroutan and N. K. Nikolova, "Dynamic range of an active radio sensor for bias-switched arrays for microwave tissue imaging," in *IEEE Intern. Symp. Antennas Propag. APS/URSI*, pp. 11–12, May 2018.

[26] V. Tyagi, *Active Sensor Array for UWB Breast-Cancer Screening.* PhD thesis, McMaster University, 2021.